

University of Nottingham
UK | CHINA | MALAYSIA

Wearable Magnetoencephalography

by

Elena Boto, *Licenciada*

Thesis submitted to the University of Nottingham

for the degree of Doctor of Philosophy

December 2018

Contents

Abstract **iv**

Acknowledgements **v**

Introduction **1**

1 Magnetoencephalography **7**
1.1 The MEG signal . . . 7
1.1.1 Neurons and signal origins . . . 8
1.1.2 Measurable neuroelectrical effects . . . 12
1.2 Data analysis . . . 15
1.2.1 Forward problem . . . 15
1.2.2 Inverse problem . . . 20
1.3 Data collection: the MEG system . . . 24
1.3.1 Conventional superconducting MEG systems . . . 24
1.3.2 Emerging technologies . . . 30

2 Optically-pumped magnetometers **33**
2.1 Introduction . . . 33
2.1.1 Principle of operation . . . 35
2.1.2 The QuSpin sensor . . . 36
2.2 Atomic energy levels . . . 37
2.2.1 Fine structure . . . 39
2.2.2 Hyperfine structure . . . 40
2.2.3 Zeeman splitting . . . 40
2.3 Optical pumping . . . 40
2.4 Zero field and spin-exchange suppression . . . 42
2.5 Signal equations . . . 44
2.6 Summary . . . 47

3 Potential advantages of OPMs for MEG **48**
3.1 Introduction . . . 48
3.2 Methods . . . 50
3.2.1 Simulated systems . . . 50
3.2.2 Comparison of SNR . . . 52
3.2.3 Beamformer reconstruction accuracy . . . 53
3.2.4 Spatial resolution and channel count . . . 59
3.3 Results . . . 61
3.4 Discussion . . . 69

3.4.1 SNR . . . 70
3.4.2 Reconstruction accuracy . . . 72
3.4.3 Spatial resolution . . . 73
3.4.4 Limitations . . . 74
3.5 Conclusions . . . 76

4 Experimental MEG measurements using a single OPM 77
4.1 Introduction . . . 77
4.2 Methods . . . 79
4.2.1 Data acquisition . . . 79
4.2.2 Data analysis . . . 83
4.3 Results . . . 86
4.4 Discussion . . . 93
4.4.1 Gradiometry . . . 93
4.4.2 Scanner-casts . . . 95
4.4.3 Signal magnitude and SNR . . . 96
4.5 Conclusions . . . 98
4.A Appendix . . . 99

5 Towards wearable OPM-MEG 103
5.1 Introduction . . . 103
5.2 OPM-MEG instrument description . . . 105
5.2.1 System overview . . . 106
5.2.2 Nulling coils . . . 108
5.2.3 Sensor gain . . . 109
5.2.4 Crosstalk . . . 113
5.2.5 Motion tracking . . . 115
5.3 Methods . . . 116
5.3.1 Data acquisition . . . 116
5.3.2 Data collection . . . 118
5.3.3 Data analysis . . . 119
5.3.4 Quantifying spatial resolution . . . 122
5.4 Results . . . 123
5.4.1 Finger abduction paradigm . . . 123
5.4.2 Ball game paradigm . . . 127
5.4.3 Spatial resolution . . . 128
5.5 Discussion . . . 130
5.5.1 Signal-to-interference . . . 130
5.5.2 Spatial resolution . . . 131
5.5.3 Wearable technology . . . 132
5.6 Conclusions . . . 132

6 Comparison with EEG 133
6.1 Introduction . . . 133
6.2 Methods . . . 134
6.2.1 System . . . 134
6.2.2 Data acquisition . . . 136
6.2.3 Data analysis . . . 137
6.3 Results . . . 138

6.3.1 Finger abduction 138
6.3.2 Muscle tensing 140
6.4 Discussion 142
6.4.1 Muscle artefacts 143
6.4.2 Spatial resolution 144
6.4.3 Practicalities 144
6.5 Conclusions 145

7 Concluding remarks **146**
7.1 Signal-to-noise ratio 146
7.2 Improved practicality 147
7.3 3D printing and future helmet design 148
7.4 New OPM designs 148
7.5 Epilogue 149

Bibliography **151**

Abstract

Functional neuroimaging offers a means to understand brain function and dysfunction. Over decades, different technologies have been developed to provide a non-invasive measure of brain activity that could help us to better understand the mechanisms underlying human cognition. Magnetoencephalography (MEG) is one of these techniques which, over the past 30 years, has been increasingly contributing to neuroscientific studies giving insights into human brain electrophysiology, with excellent temporal resolution and surprisingly high spatial resolution. However, MEG hardware has limitations and it has only been in the past few years that alternative technologies have seen a rapid progress with an intent to overcome the drawbacks of conventional MEG devices. The main limitation of MEG systems is that they rely on superconducting quantum interference devices (SQUIDs) to measure magnetic fields outside the head. This means that they require cryogenic cooling and as a consequence, sensors are fixed in position in a one-size-fits-all helmet. A vacuum is maintained between the subject's head and the detectors which limits the sensitivity of the measurement, and subjects must remain still in large cumbersome scanners.

Advances in the field of quantum technologies mean that magnetic field sensors, such as optically-pumped magnetometers (OPMs), operating at room temperature, are now able to achieve sensitivities similar to that of SQUIDs. This means that room temperature magnetoencephalography (MEG), with a greatly increased flexibility of sensor placement, can now be considered. Furthermore, these new sensors can be placed directly on the scalp surface giving, theoretically, a large increase in the magnitude of the measured signal.

In this thesis, we explore the advantages of multi-channel OPM systems using both simulations, and experimental measurements made using commercially available OPMs in combination with a 3D-printed helmet. With the incorporation of field-nulling technologies, we demonstrate a non-restrictive MEG system that could benefit many different participant cohorts, for example children. The results presented highlight the opportunity afforded by OPMs to generate uncooled, potentially low-cost, high sensitivity MEG systems which offer a step change compared to the current generation of cryogenic instrumentation.

Acknowledgements

First of all, I would like to thank my supervisors Dr Matthew Brookes and Prof Richard Bowtell. It has been a joy working with you but more importantly, learning from you. This thesis hopefully reflects those lessons. Matt, thanks for replying to that email from 2013, even if it was three years later, and for giving me the opportunity to start this project which I have enjoyed doing since the beginning. I should say that the highlight of these years has been the day I beat you at badminton. Many thanks also to Prof Mark Fromhold for giving me the opportunity to participate in the Quantum Technologies programme and supporting me throughout my time as a Ph.D. student.

None of this work would have happened without the collaboration with Prof Gareth Barnes, whose expertise and constant enthusiasm have led to things we could not have imagined happening in such a short time.

An obvious thank-you goes to Dr Vishal Shah and his team in QuSpin, without whose efforts and collaboration some of the experimental work would not have happened.

Special mention goes to the members of the OPM team (a.k.a. the ones who ended The Shed's life): Dr JL, Gill, Niall: thank you for joining the OPM club with your wonderful brains, without you, we would not have been in the game at all, and Chapter 5 would not have existed. Ryan, I could have done with not having you, since you and Niall have the same name after all and I just get confused. I am kidding, you can stay, and carry on with the wonderful baby OPM project that you started. But, don't forget to bring pork scratchings.

Dom, thanks to you I think I now understand that accent that is spoken remotely on the other side of the planet. But I am even more grateful for all your more-than-needed expertise, which made possible the Royal Society exhibit. I would also like to thank everyone who participated and made 'Quantum Sensing the Brain' happen. It was an incredible experience thanks to you all.

Thanks to the MEG team in its entirety, for the fun activities we have done together, always starting and finishing at the pub, and usually involving curry for dinner. I would like to give George a special mention, who has always been extremely helpful since the very beginning. Lauren, you are a constant inspiration on how to walk through this world with a smile on your face. You have made my Ph.D. life very enjoyable.

I should also thank Lesley, Henry and Alan for their invaluable help.

A special thanks goes to Jorge for showing me Nottingham and its lovely

University.

I am thankful for the friendships formed during the past three years. Ben, Nick, I still miss having you here. Simon, I do not miss you that much just yet, even though the lack of gossip is noticeable. Adam, if you come back I promise I will let you beat me at badminton. Gita, wherever we are next, we should definitely keep in touch!

Andy, the ~~little~~ nightmare. You made the time during my last year very enjoyable, but rather distracting, maybe you did us all a favour by leaving Nottingham after all. You are allowed to come back now. *Gracias*.

And now into the Spanish section:

Gracias a la existencia de Whatsapp, Telegram, Skype, Facebook, Instagram, etc... la comunicación con la familia y amigos ha sido relativamente fácil. Mención especial a Grupitis, que da gusto que después de 25 años nos sigamos viendo. Pau, Clau y Mari, gracias por estar cerca a pesar de la distancia, os perdono por haber vivido juntas sin mí. Pilar y Balbi, mis *uapas*, gracias por siempre estar al otro lado del teléfono.

Y finalmente, a mi familia. Luis. Lis. Te admiro mucho, no podría haber tenido un hermano mayor mejor. Gracias Titi por llenarme la maleta de embutido cada vez que vuelvo a casa. Eli, no me dio tiempo a acabar esto para que lo vieras. Papá y Mamá. Gracias por darme absolutamente todo, por apoyarme en cada momento. Una de las mayores satisfacciones es ver que os sentís orgullosos de mí. Espero que este librillo os haga sentir así.

Esta tesis se la dedico a mi familia. Os echo de menos.

Introduction

Our ability to non-invasively measure human brain function has revolutionised neuroscience. Unlike structural imaging techniques such as X-ray Computed Tomography (Hounsfield, 1973) or Magnetic Resonance Imaging (MRI, Lauterbur (1973); Mansfield and Grannell (1973)) which generate images (with millimetre or better spatial resolution) of brain structure, functional imaging techniques provide a measure of the evolution of human brain activity over time. In this way, researchers and clinicians are offered a non-invasive window on the working human brain. This is important to understand how the healthy brain operates, but also critical in disorders where brain structure looks normal, but brain function is perturbed (this can be the case in disorders such as epilepsy, or in some mental health conditions such as schizophrenia).

Functional brain imaging techniques

The late 20th century saw the development of a number of ways to measure brain function non-invasively, and of these techniques, five (see Table 1 for a summary) have become prominent and are now used in imaging laboratories worldwide:

- **Functional Magnetic Resonance Imaging** (**fMRI**; Ogawa et al. (1990)) exploits the fact that when an area of brain becomes 'active' (i.e. when neurons begin to fire) it requires more energy. This means that an in-

crease in the supply of oxygenated blood is required local to that region. There is a difference between the magnetic properties of oxy- and deoxy-haemoglobin, the former being diamagnetic and the latter paramagnetic. This offers an endogenous contrast agent which allows us to measure changes in the intensity of rapidly acquired MR images (Mansfield, 1977). In this way, fMRI offers a useful means to measure brain activity, with high spatial resolution. However, because it represents an indirect measurement of neural activity (i.e. via blood flow rather than activity in neurons) its temporal resolution is limited.

- **Positron Emission Tomography** (**PET**; Fox et al. (1984)) involves the administration of a radioactively labelled isotope to a subject, such as ^{15}O or ^{18}F. These nuclei are unstable, and will emit a positron which, on collision with an electron, will result in mutual annihilation and consequently, two gamma rays are emitted at 180° of each other. These are detected by an array of detectors around the patient and back-projection-reconstruction enables reconstruction of images showing distribution of the positron emitting isotope in the body. Administration of ^{15}O to a subject enables us to map, in time and space, oxygen use in the brain and so, in a manner similar to fMRI, this technique offers an indirect measure of brain activity. However, the use of PET, particularly in healthy volunteers is limited because of the risk of ionising radiation.

- **Functional Near-InfraRed Spectroscopy** (**fNIRS**; Ferrari and Quaresima (2012)) also provides an indirect measurement of brain function by detecting changes in haemoglobin concentrations. These can be measured by means of the characteristic absorption spectra of infrared light by haemoglobin in the brain. fNIRS is a practical technique since, unlike PET or fMRI which require subjects to remain still in large and expensive scanners, fNIRS only requires the use of a set of optodes, which are mounted on the head in a helmet arrangement. So, this means that whilst the indi-

rect nature of the measurement, and the mechanism of fNIRS limits both temporal and spatial resolution (respectively) it can be deployed in vulnerable patient cohorts (in particular fNIRS has found extensive use in children).

- **Electroencephalography** (**EEG**; Berger (1929)) relies on the measurement of electrical potential on the scalp surface, generated by synchronised current flow through neuronal assemblies in the brain. Invented in the 1920's, EEG offers extremely high temporal resolution by virtue of the fact that electrical activity is measured directly. EEG is also extremely practical, with activity being measured by head-mounted electrodes. However, EEG also suffers from poor spatial resolution because electrical potentials need to pass through the skull and be measured at the surface of the scalp. Because the skull has high electrical resistance, the spatial signature of those electrical potentials gets distorted, and this limits its utility as an "imaging" modality.

- **Magnetoencephalography** (**MEG**; Cohen (1968)) assesses the changes in magnetic field outside the head that are generated by the same neuronal currents which produce the electrical potential measured with EEG. MEG offers the same exquisite temporal resolution as EEG; however unlike electrical potentials, magnetic fields pass through the skull relatively unaffected, and this means that MEG offers significantly better spatial resolution than EEG. However, at present MEG requires the use of superconducting sensors which are cryogenically cooled, making systems expensive. Also, similar to fMRI and PET, systems require subjects to remain still with their head in a fixed position inside a helmet; this means utility is often limited by a lack of practicality, particularly in young subject cohorts.

Table 1: **Functional neuroimaging techniques.**

	fMRI	**PET**	**fNIRS**	**EEG**	**MEG**
Temporal resolution	∼5 s	∼5 s	∼5 s	1 ms	1 ms
Spatial resolution	1 mm (7T)	4–5 mm	<1.5 cm	a few cm	3–10 mm
Cost	£1M (3T)	∼ £300k (> £10M[1]) [1] with cyclotron	∼ £200k	£20k	∼ £2M
Invasiveness	No	Yes	No	No	No
Wearable	No	No	Yes	Yes	No
Motion robustness	No	No	Yes	Yes	No
Mechanism	Indirect	Indirect	Indirect	Direct	Direct

Thesis aim

Of all of the methods discussed above, MEG offers the best combination of direct and non-invasive access to electrophysiological activity with sub-millisecond temporal resolution and high spatial resolution. It is almost uniquely equipped to bridge the gap between human data (acquired non-invasively), animal data (acquired using invasive electrodes which measure electrical activity directly) and computational models of electrophysiology, in both health and disease. However, severe limitations lie in current MEG sensor technology. Most MEG systems consist of an array of superconducting detectors placed inside a fixed dewar. The system tends to be one-size-fits-all, and subject movement relative to the fixed sensors degrades data quality. The requirement for cryogenic cooling means that a vacuum must be maintained between the head and the detectors, which are consequently sited 3–6 cm from the adult brain surface and this distance is even greater in subjects with smaller heads (e.g. infants). MEG is therefore limited by a low signal-to-noise ratio (SNR), and this is particularly important given that the magnetic fields generated by the brain are much smaller than environmental and biomagnetic interference. In addition, the high purchase cost and significant running cost (due to cryogenics) have limited clinical take-up of MEG systems, and the worldwide shortage of helium is a constant

threat to the smooth operation of a MEG laboratory. However, recycling systems are able to reduce this problem.

In principle, many of these limitations could be lifted if body temperature detectors could be used to detect the tiny magnetic fields generated by the brain. If sensors could be made small and lightweight they could be moved closer to the head, potentially even on to the scalp surface, and this would generate an increase in the measurable signal and potentially SNR. Moving sensors towards the head would also allow for better measurement of the spatial distribution of extracranial magnetic fields and so consequently potentially better spatial resolution. Flexible sensor placement would allow a system to adapt to any head size, and in principle subjects might even be able to move during scanning. These latter two points would have the extremely attractive property of combining the advantages of the high spatial resolution of MEG with the practicality of EEG. The aim of this thesis is to explore the potential of scalp-mounted sensor arrays, for detection of the MEG signal.

Thesis overview

The thesis is divided into six chapters:

Chapter 1 describes the theory behind MEG, from the origin of the signal to the mathematical methods used to exploit the rich information content carried by neuromagnetic field data. The instrumentation of current systems is also reviewed and emerging technologies presented.

In **Chapter 2** we review the potential of one specific sensor type, the optically-pumped magnetometer (OPM), for MEG signal detection. The mechanisms behind OPM operation are described, with particular focus in the QuSpin device which has recently been commercialised and will be used throughout this thesis.

In **Chapter 3** a set of simulations is described, with the aim of comparing,

quantitatively, the advantages of a hypothetical whole-head scalp-mounted MEG device, over current state-of-the-art systems based on cryogenic sensors.

Chapter 4 presents the first experimental measurements made with a single, lightweight, commercialised, QuSpin OPM. We describe the critical requirement for interference reduction via a technique known as gradiometry, and we also exploit the accuracy of 3D printing for sensor mounting. A comparison with superconducting sensors is also carried out.

Chapter 5 describes the fabrication and implementation of a multi-channel 'wearable' MEG device based on 13 OPMs in a scanner-cast. We bring together this novel device with a field-nulling technique which allows, for the first time, unrestricted movement during MEG acquisition. We also describe development and application of a naturalistic paradigm, exploiting the fact that participants can move.

Chapter 6 provides a comparison between EEG and our newly developed OPM-MEG device. Specifically in terms of movement and muscle artefacts.

At the end of the thesis, concluding remarks are given, and a perspective on the future of OPM technology is put forward.

Chapter 1

Magnetoencephalography

This chapter will cover the basic theory underlying magnetoencephalograhy (MEG), from the origins of the signal to the instrumentation used for its detection. The chapter will also cover the mathematical methods used to infer 3D images of brain activity via reconstruction of magnetic field data.

1.1 The MEG signal

Sitting on our shoulders is perhaps the most complex organised structure in the universe[1]: the human brain, which remains poorly understood. The principal building block of the brain is the neuron: a type of electrical cell which constitutes the most fundamental information processing unit. When information is being processed, small electrical currents flow within and between neurons which, like any other electrical currents, produce a magnetic field. Provided that thousands of neurons act in concert (Murakami and Okada, 2006), then these tiny fields interfere constructively and a small but measurable magnetic field signal can be captured non-invasively outside the head, using very sensitive magnetic field detectors. The ability to measure these magnetic fields and

[1]Adapted from Michio Kaku's quote: "The human brain has 100 billion neurons, each neuron connected to 10 thousand other neurons. Sitting on your shoulders is the most complicated object in the known universe."

extract the relevant underlying information on neural current flow constitutes the basis of magnetoencephalography (MEG) (Baillet, 2017).

1.1.1 Neurons and signal origins

Around 100 billion neurons exist in the cortex, the brain's outermost structure. A single neuron consists of four parts (see Figure 1.1):

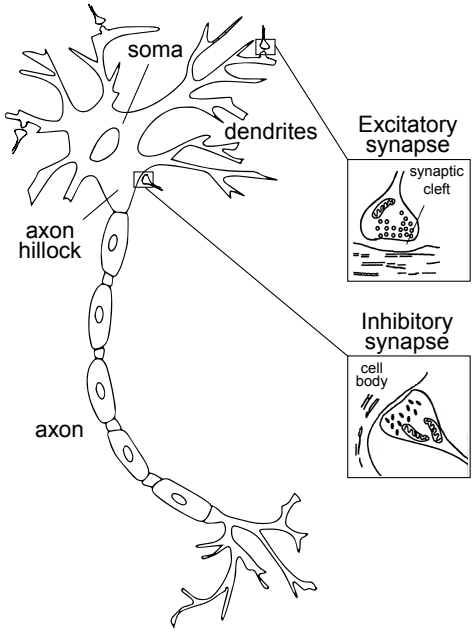


Figure 1.1: **Schematic of a neuron.** Partly adapted from Hämäläinen et al. (1993).

- **Soma**. Also referred to as the cell body, contains the nucleus and much of the metabolic machinery.
- **Dendrites**. Thread-like extensions of the soma which receive electrochemical impulses from other cells.
- **Axon**. A single long fibre that carries the nerve impulse (called the action potential) away from the soma to other cells.
- **Axon hillock**. Part of the cell where the action potential is initiated.

The soma and dendrites form the gray matter (see Figure 1.2a/b), while axons mainly form the white matter, connecting different (functionally-specialised)

cortical regions as well as deeper structures such as the thalamus and brain stem. Depending on the distribution of dendrites around the soma, neurons can fall into two groups: stellate and pyramidal cells. The former have mostly symmetric dendritic configuration while, in contrast, pyramidal neurons have a highly asymmetric dendritic tree, with dendrites mostly oriented perpendicular to the cortical surface (Orrison et al., 1995). Since dendrites guide the current flow, the elongated morphology of pyramidal neurons constrains the current along the cell, creating a greater magnetic field compared to that from stellate cells, whose symmetric dendritic configuration tends to cause magnetic fields to cancel. In Figure 1.2c these two types of neurons can be observed in one of Ramón y Cajal's drawings.

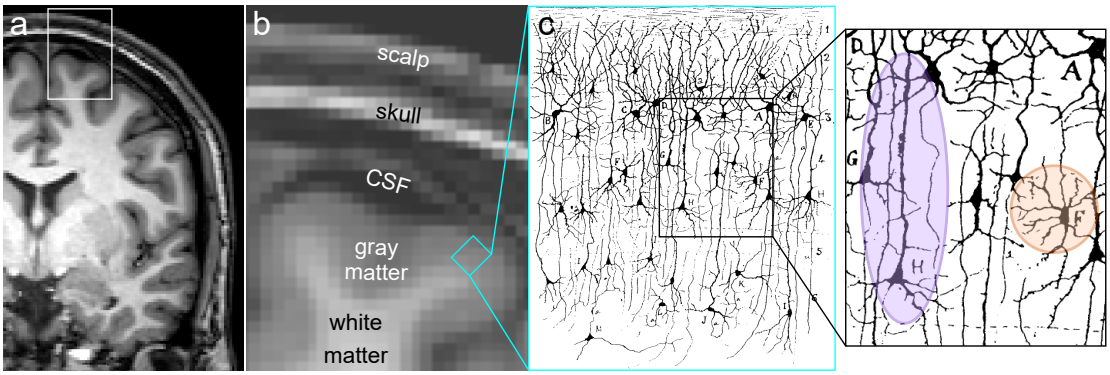


Figure 1.2: **Cortical surface.** a) Coronal slice of a magnetic resonance image. b) Inset of (a) showing the different tissue types. c) Inset of (b), drawings made by Ramón y Cajal in 1888 where different types of neurons are represented. Zoomed-in image shows examples of pyramidal and stellate neurons in purple and orange, respectively. Adapted from Hämäläinen et al. (1993).

Neurotransmission

The neuron, like any other cell, is surrounded by an insulating membrane which divides the tissue into intracellular and extracellular compartments, each having different ion concentrations (mainly K^+ (potassium), Na^+ (sodium) and Cl^-(chlorine) ions). In the resting state, there is an imbalance in ion concentrations across the membrane, which results in a potential difference of –70 mV in the intracellular, relative to the extracellular space. However, interaction be-

tween cells can change this potential and if the potential at the axon hillock reaches a threshold level, the neuron "fires" an **action potential** (see below); this is effectively a small current "pulse" that propagates along the axon. As mentioned above, interactions between neurons are mediated via electrochemical processes. These processes initiate in the synapses (or connections) between neurons and can be excitatory (increase of the intracellular potential, making the cell more likely to fire) or inhibitory (decrease of the intracellular potential, making the cell less likely to fire). Most excitatory synapses are on the dendrites while inhibitory synapses often attach to the soma (see Figure 1.1). For synaptic transmission to occur, an action potential arrives at the end of the axon of the pre-synaptic neuron and this stimulates the release of neurotransmitter molecules into the synaptic cleft (the space between the axon and the dendrite), which causes the opening of ion channels on the walls of the post-synaptic cell. These channels allow flow of ions into the cell, therefore changing the potential difference across the membrane. Consequently, current will flow into the post-synaptic neuron and along its dendrites. This **post-synaptic potential** (see below) makes the post-synaptic cell more or less likely to fire.

Therefore, two major classes of neuronal current can create an extracanial magnetic signal: currents associated with action potentials and those associated with post-synaptic potentials:

Action potentials

The action potential is characterised by a leading edge of depolarisation and a trailing edge of repolarisation as it moves down the axon. It is initiated at the axon hillock when the intracellular potential reaches the firing threshold of about –55 mV, allowing voltage-gated Na^+ and K^+ ion channels to open. The concentration of ions on both sides of the membrane changes, with Na^+ ions flowing in and K^+ ions flowing out of the cell. The conductivity of sodium

suddenly increases, causing a rapid influx of Na^+ ions into the neuron. This depolarises the membrane, raising the potential to 40 mV in ∼1–2 ms. This rapid change of potential then triggers the adjacent region, causing action potentials down the axon with unattenuated amplitude. The conductivity of the cell membrane to sodium finally increases enough to cause an efflux of K^+ ions, repolarising the membrane and lowering the potential back to the resting state. The action potential can be approximated by two oppositely-oriented current dipoles (Figure 1.3a): the leading edge can be modelled by a current dipole oriented away from the soma, while the repolarisation edge is modelled as a current dipole oriented toward the soma. Therefore, the action potential is approximated by a quadrupolar current.

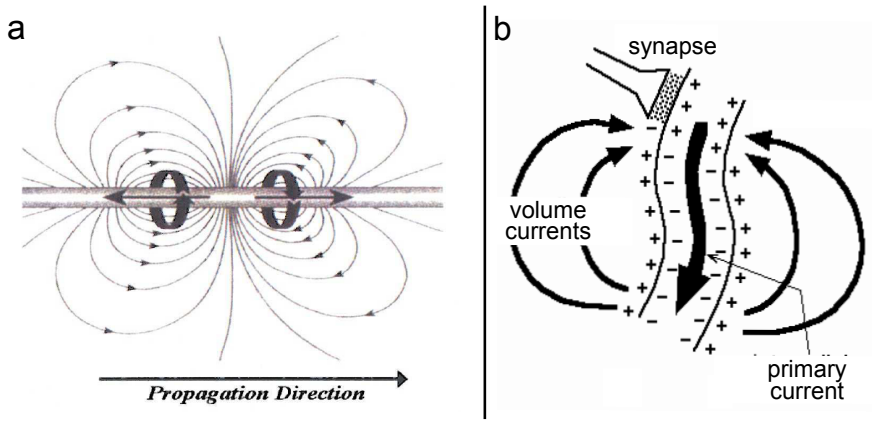


Figure 1.3: **Current patterns.** a) Action potential. b) Post-synaptic potential. Adapted from Orrison et al. (1995) and Vrba (2000).

Post-synaptic potentials

As noted above, termination of an action potential at the end of the axon of a pre-synaptic cell causes neurotransmitter release. Neurotransmitters cause the opening of ion channels on the walls of the post-synaptic cell. If these channels open allowing Na^+ ions into the cell, the cell is depolarised and there is an excitatory post-synaptic potential. If on the other hand, ion channels open allowing K^+ out of the cell or Cl^- into the cell, the cell is hyperpolarised and there is an inhibitory post-synaptic potential. This means that the likelihood of

the cell firing an action potential will be dependent on the sum of these two events (i.e. neurons act as simple integrators). Post-synaptic events cause current to flow along the dendrites and into the soma. This is referred to as the intracellular or primary current (Figure 1.3b), which can be approximated as a dipole and has a lifetime of around 10 ms. Following the passage of a primary current, the resting potential of the neuron must be restored: ions are pumped back into the extracellular region, resulting in an electric field between the ion expulsion point and the synaptic junction, originating an extracellular current in the opposite direction to the primary current. This is called extracellular or volume current (Figure 1.3b). The signals originated from volume currents are therefore dependent on the conductivity of the surrounding tissue. Later we will show that they have little effect on the measurable magnetic field.

A dipolar field, produced by post-synaptic currents, decreases with distance as $1/r^2$, more slowly than the $1/r^3$-dependent quadrupolar field, produced by action potentials. In addition, the overall duration of post-synaptic currents (lasting tens of milliseconds) is longer than that of action potentials (which have a duration of 1 ms only), allowing a greater likelihood of synchronisation and therefore constructive summation of fields. The greater probability of synchronisation, the dipole nature ($1/r^2$) and the asymmetry of dendrites mean that the neural origin of the MEG signal is likely to be the synchronisation of tens of thousand post-synaptic currents in pyramidal neurons.

1.1.2 Measurable neuroelectrical effects

Neuromagnetic fields detected with MEG are very rich in temporal and spectral information, and depending on the type of recordings made and the way signals are analysed, different information will be generated. Below three different categories of MEG-detectable effects are introduced:

Spontaneous activity

Spontaneous rhythms occur naturally in the brain without requiring any external stimulation. They were first discovered in humans by Hans Berger in 1929 (Berger, 1929) using his newly developed electroencephalogram (EEG). He measured amplitude changes in a rhythm of 8 to 13 Hz at the back of the subject's head associated with the opening and closing of the eyes. Since then, efforts have been made to characterise these oscillations in the brain and depending on their frequency, different types of oscillation have been categorised: raging from slow rhythms (Delta, $<$4 Hz and Theta, 4-8 Hz) to faster oscillations (Alpha, 8-13 Hz; Beta, 13-30 Hz and Gamma $>$30 Hz). The frequency band of interest in MEG is thus between 0.5-1,000 Hz, although the vast majority of studies tend to look in the 1-100 Hz band (Lopes da Silva, 2013).

Evoked responses

An evoked response is a signal that is time- and phase-locked to an external event. Experiments looking at evoked responses often involve the repetition of a stimulus over multiple trials. Because an evoked response is phase-locked, averaging it over multiple trials will not change its magnitude or morphology. However, the magnitude of non phase-locked (e.g. random) signals will decrease with the square root of the number of averages (trials). Consequently, after averaging, the random fluctuations are attenuated and the evoked response is revealed prominently. Studies into evoked responses typically involve the presentation of a sensory stimulus, e.g. in the visual (Ahlfors et al., 1992), somatosensory (Hari et al., 1993) or auditory cortices (Hari et al., 1987).

Induced effects

The term 'induced' is given to a stimulus-related change in spontaneous activity. It has been shown that amplitude of oscillations can be modulated in the presence of a stimulus (Pfurtscheller and Lopes Da Silva, 1999). Unlike evoked responses, whilst time-locked, induced effects are non phase-locked, and therefore trial averaging would result in the loss of induced effects from the signal. To avoid this, neuromagnetic signals are first frequency filtered to the band of interest and then squared (or the amplitude envelope calculated) in order to measure stimulus-induced oscillatory power change in that band. Averaging envelopes across trials will then result in observable induced effects.

This thesis is predominantly concerned with the development of MEG hardware. Consequently, we restrict ourselves to detection of repeatable and reliable MEG effects. Specifically, we look to measure the somatosensory evoked response and the movement/sensory induced beta response. The somatosensory evoked response typically comprises an early (20 ms) deflection (the N20) followed by a later ($\sim$40 ms) response (P35/P40) and then a (100 ms) response (the P100). This response, which is commonly evoked via electrical stimulation of the median nerve, is one of the most reliable MEG signals. The induced beta response is usually generated by movement, and comprises a reduction of oscillatory power in the 13–30 Hz band during movement followed by an increase above baseline on movement cessation. Again this is one of the most reliable and robust effects in MEG/EEG signals, nevertheless there is significant interest in its temporal morphology with e.g. the post-movement "rebound" being related to the formation of transient long range networks (Tewarie et al., 2018) and its amplitude being diminished in e.g. schizophrenia (Robson et al., 2016).

1.2 Data analysis

Having recorded MEG data, the major challenge is to extract the underlying neuronal currents based only on the extracranial magnetic fields that they generate. For this, we need to have a model of the magnetic field pattern outside the head generated by a known current. Generation of this model is referred to as the Forward Problem, which could be stated as: *given a known distribution of current within the brain, can we determine the resulting magnetic fields?* A few things need to be considered before solving this problem:

- The permeability, μ, of tissues in the head and its different compartments is approximately the same as that of free space, μ_0, so we can treat the entire medium as homogeneous.
- The extracranial magnetic fields are generated by the primary and volume currents originated at the dendrites of post-synaptic neurons. The primary current can be approximated by a dipole.

1.2.1 Forward problem

The magnetic fields generated by a current density **J** located inside a volume (e.g. the head) can be derived using Maxwell's equations:

$$\begin{aligned} \nabla \cdot \mathbf{E} &= \frac{\rho}{\epsilon}, \\ \nabla \cdot \mathbf{B} &= 0, \\ \nabla \times \mathbf{E} &= -\frac{\partial \mathbf{B}}{\partial t}, \\ \nabla \times \mathbf{B} &= \mu_0 \left(\mathbf{J} + \epsilon \frac{\partial \mathbf{E}}{\partial t} \right), \end{aligned} \tag{1.1}$$

where ϵ is the permittivity of a medium, μ_0 is the permeability of free space and ρ is the charge density. The electromagnetic fields from the brain vary at low frequencies (1–80 Hz) and therefore we can adopt the quasistatic approximation

(Hämäläinen et al., 1993), meaning that the last two equations in 1.1 can be modified as:

$$\begin{aligned} \nabla \times \mathbf{E} &= 0, \\ \nabla \times \mathbf{B} &= \mu_0 \mathbf{J}. \end{aligned} \tag{1.2}$$

The solution for the magnetic field is then given by the Ampère-Laplace law:

$$\mathbf{B}(\mathbf{r}) = \frac{\mu_0}{4\pi} \int_G \mathbf{J}(\mathbf{r}') \times \frac{\mathbf{r} - \mathbf{r}'}{|\mathbf{r} - \mathbf{r}'|^3} dv', \tag{1.3}$$

where $\mathbf{r}$ is the location where the field is to be measured and $\mathbf{r}'$ a location inside the volume conductor G.

The total current $\mathbf{J}$ can be written as the sum of the primary and volume currents,

$$\mathbf{J} = \mathbf{J}_p + \mathbf{J}_v. \tag{1.4}$$

The volume current is the result of the macroscopic electric field on charge carriers in the conducting medium, i.e. it is an ohmic current, therefore, assuming uniform conductivity σ, we can write $\mathbf{J}_v(\mathbf{r}) = \sigma \mathbf{E}(\mathbf{r})$. Given that the electric field is related to the electrical potential in the form of $\mathbf{E} = -\nabla V$, Equation 1.4 becomes:

$$\mathbf{J}(\mathbf{r}) = \mathbf{J}_p(\mathbf{r}) - \sigma \nabla V(\mathbf{r}). \tag{1.5}$$

Substituting Equation 1.5 into Equation 1.3 yields:

$$\begin{aligned} \mathbf{B}(\mathbf{r}) = \frac{\mu_0}{4\pi} \int_G \mathbf{J}_p(\mathbf{r}') \times \frac{\mathbf{r} - \mathbf{r}'}{|\mathbf{r} - \mathbf{r}'|^3} dv' \\ - \frac{\mu_0}{4\pi} \sum_{j=1}^{n} \sigma_j \int_{G_j} \nabla V(\mathbf{r}') \times \frac{\mathbf{r} - \mathbf{r}'}{|\mathbf{r} - \mathbf{r}'|^3} dv', \end{aligned} \tag{1.6}$$

where the sum is over different head compartments, G_j, as shown in Figure 1.4a, with conductivity σ_j. Focussing on the second integral, using the vector identity $\nabla \mathrm{a} \times \nabla \mathrm{b} = \nabla \times (\mathrm{a} \nabla \mathrm{b})$, where $\mathrm{a} = V(\mathbf{r}')$ and $\nabla \mathrm{b} = (\mathbf{r} - \mathbf{r}')/|\mathbf{r} - \mathbf{r}'|^3$ we

get:

$$\nabla V(\mathbf{r}') \times \frac{\mathbf{r}-\mathbf{r}'}{|\mathbf{r}-\mathbf{r}'|^3} = \nabla \times V(\mathbf{r}') \frac{\mathbf{r}-\mathbf{r}'}{|\mathbf{r}-\mathbf{r}'|^3}. \tag{1.7}$$

Now applying the generalised Stokes' theorem: $\int_G \nabla \times \mathbf{X}\, dv' = \int_S \hat{\mathbf{n}} \times \mathbf{X}\, ds$, Equation 1.6 becomes:

$$\begin{aligned}\mathbf{B}(\mathbf{r}) = \frac{\mu_0}{4\pi} \int_G \mathbf{J}_p(\mathbf{r}') \times \frac{\mathbf{r}-\mathbf{r}'}{|\mathbf{r}-\mathbf{r}'|^3} dv' \\ - \frac{\mu_0}{4\pi} \sum_{j=1}^{n} (\sigma_j' - \sigma_j'') \int_{S_j} V(\mathbf{r}') \cdot \hat{\mathbf{n}}(\mathbf{r}') \times \frac{\mathbf{r}-\mathbf{r}'}{|\mathbf{r}-\mathbf{r}'|^3} dS_j.\end{aligned} \tag{1.8}$$

This is called the Geselowitz formula (Geselowitz, 1967): σ' and σ'' are the conductivities in adjacent compartments and $\hat{\mathbf{n}}(\mathbf{r}')$ is a unit vector perpendicular to surface S_j at $\mathbf{r}'$. Note that the first term corresponds to the magnetic fields due to the primary current, $\mathbf{B}_p(\mathbf{r})$, and is invariant to the conductivity profile of the medium. The second term contains the contribution from the volume currents to the magnetic field, $\mathbf{B}_v(\mathbf{r})$. Note that the volume currents have been approximated as a set of fictitious currents flowing on a conductive surface S_j.

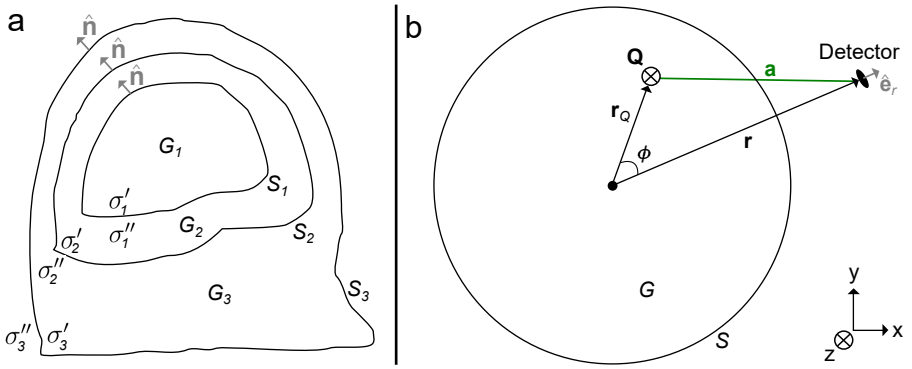


Figure 1.4: **Forward model set-up.** a) Schematic diagram showing three head compartments with their respective volumes G_j, surfaces S_j, normal vectors $\hat{\mathbf{n}}$ and conductivities σ_j. b) Single sphere model.

Single sphere model

It is common in MEG to approximate the head (brain, skull and scalp) to a single spherically symmetric conductor (see Figure 1.4b): we assume that the

volume G is bound to a spherical surface S and has a uniform conductivity σ. The radial component of the magnetic field, $B_r(\mathbf{r})$ outside a sphere (i.e. along the $\mathbf{r}$ direction) can be easily computed: given that $\mathbf{B}(\mathbf{r}) \cdot \hat{\mathbf{e}}_r(\mathbf{r}) = B_r(\mathbf{r})$. The detectable field then becomes:

$$\begin{aligned} B_r(\mathbf{r}) = \frac{\mu_0}{4\pi} \int_G \mathbf{J}_p(\mathbf{r}') \times \frac{\mathbf{r} - \mathbf{r}'}{|\mathbf{r} - \mathbf{r}'|^3} \cdot \hat{\mathbf{e}}_r \, dv' \\ - \frac{\mu_0 \sigma}{4\pi} \int_S V(\mathbf{r}') \cdot \hat{\mathbf{n}}(\mathbf{r}') \times \frac{\mathbf{r} - \mathbf{r}'}{|\mathbf{r} - \mathbf{r}'|^3} \cdot \hat{\mathbf{e}}_r \, dS. \end{aligned} \tag{1.9}$$

Focussing on the second integral, specifically on the term: $\hat{\mathbf{n}}(\mathbf{r}') \times (\mathbf{r} - \mathbf{r}') \cdot \hat{\mathbf{e}}_r$:

$$\hat{\mathbf{n}}(\mathbf{r}') \times (\mathbf{r} - \mathbf{r}') \cdot \hat{\mathbf{e}}_r = (\hat{\mathbf{n}}(\mathbf{r}') \times \mathbf{r} - \hat{\mathbf{n}}(\mathbf{r}') \times \mathbf{r}') \cdot \hat{\mathbf{e}}_r. \tag{1.10}$$

This term equals to zero because:

$$\begin{aligned} \hat{\mathbf{n}}(\mathbf{r}') \times \mathbf{r}' = 0 \text{ since} \qquad & \hat{\mathbf{n}}(\mathbf{r}') \parallel \mathbf{r}' \\ \hat{\mathbf{n}}(\mathbf{r}') \times \mathbf{r} \cdot \hat{\mathbf{e}}_r = 0 \text{ since} \quad & (\hat{\mathbf{n}}(\mathbf{r}') \times \mathbf{r}) \perp \hat{\mathbf{e}}_r. \end{aligned} \tag{1.11}$$

Consequently, the second term in Equation 1.9 vanishes leaving an expression for $B_r(\mathbf{r})$ independent of the contribution of volume currents and invariant to conductivity:

$$B_r(\mathbf{r}) = \frac{\mu_0}{4\pi} \int_G \mathbf{J}_p(\mathbf{r}') \times \frac{\mathbf{r} - \mathbf{r}'}{|\mathbf{r} - \mathbf{r}'|^3} \cdot \hat{\mathbf{e}}_r \, dv'. \tag{1.12}$$

An important point here is that if the dipole source is radial, then the magnetic field outside G vanishes. However, this means that MEG remains sensitive to the vast majority of the cortex (Hillebrand and Barnes, 2002).

Current dipole

As mentioned above, we can approximate the primary current as a current dipole, $\mathbf{Q}$ at location $\mathbf{r}_Q$, therefore $\mathbf{J}_p$ can be thought of a concentration of current

to a single point,

$$\mathbf{J}_p(\mathbf{r}') = \mathbf{Q}\delta(\mathbf{r}' - \mathbf{r}_Q), \tag{1.13}$$

where $\delta(\mathbf{r})$ is the Dirac delta function. Using this, the expression for $\mathrm{B}_r(\mathbf{r})$ can be simplified further:

$$\begin{aligned} B_r(\mathbf{r}) &= \frac{\mu_0}{4\pi}\int_G \mathbf{Q}\delta(\mathbf{r}' - \mathbf{r}_Q) \times \frac{\mathbf{r} - \mathbf{r}'}{|\mathbf{r} - \mathbf{r}'|^3} \cdot \hat{\mathbf{e}}_r \, dv' \\ &= \frac{\mu_0}{4\pi}\frac{\mathbf{Q} \times (\mathbf{r} - \mathbf{r}_Q)}{|\mathbf{r} - \mathbf{r}_Q|^3} \cdot \hat{\mathbf{e}}_r. \end{aligned} \tag{1.14}$$

To obtain the other (non-radial) components of the magnetic field outside G, we make use of the Maxwell's equation $\nabla \times \mathbf{B} = \mu_0\mathbf{J}$ which becomes $\nabla \times \mathbf{B} = 0$ because $\mathbf{J} = 0$ outside G. This allows us to express the total magnetic field in terms of the magnetic scalar potential $U(\mathbf{r})$,

$$\mathbf{B}(\mathbf{r}) = -\mu_0 \nabla U(\mathbf{r}). \tag{1.15}$$

To find U, we fix $\mathbf{r}$ outside G and consider a line integral of ∇U along the radius $(\mathbf{r} + t\hat{\mathbf{e}}_r)$, where $0 < t < \infty$. U vanishes at ∞. We write:

$$\begin{aligned} U(\mathbf{r}) &= -\int_0^\infty \nabla U(\mathbf{r} + t\hat{\mathbf{e}}_r) \cdot \hat{\mathbf{e}}_r dt \\ &= \frac{1}{\mu_0}\int_0^\infty \mathbf{B}(\mathbf{r} + t\hat{\mathbf{e}}_r) \cdot \hat{\mathbf{e}}_r dt \\ &= \frac{1}{\mu_0}\int_0^\infty B_r(\mathbf{r} + t\hat{\mathbf{e}}_r) dt \\ &= \frac{1}{\mu_0}\int_0^\infty \mathbf{B}_p(\mathbf{r} + t\hat{\mathbf{e}}_r) \cdot \hat{\mathbf{e}}_r dt \\ &= \frac{1}{4\pi}\mathbf{Q} \times (\mathbf{r} - \mathbf{r}_Q) \cdot \hat{\mathbf{e}}_r \int_0^\infty \frac{dt}{|\mathbf{r} + t\hat{\mathbf{e}}_r - \mathbf{r}_Q|^3}. \end{aligned} \tag{1.16}$$

Solving the integral, which according to Sarvas (1987) is easy to compute, results in:

$$U(\mathbf{r}) = -\frac{1}{4\pi}\frac{\mathbf{Q} \times \mathbf{r}_Q \cdot \mathbf{r}}{F}, \tag{1.17}$$

where $F = a(ar + \mathbf{r}^2 - \mathbf{r}_Q \cdot \mathbf{r})$, $\mathbf{a} = \mathbf{r} - \mathbf{r}_Q$, $a = |\mathbf{a}|$ and $r = |\mathbf{r}|$.

Finally, the expression for the magnetic field outside a spherically symmetric conductor, G, created by a dipole $\mathbf{Q}$ becomes:

$$\mathbf{B}(\mathbf{r}) = \frac{\mu_0}{4\pi F^2} \left(F\mathbf{Q} \times \mathbf{r}_Q - \mathbf{Q} \times \mathbf{r}_Q \cdot \mathbf{r} \nabla F \right), \tag{1.18}$$

where $\nabla F = (r^{-1}a^2 + a^{-1}\mathbf{a} \cdot \mathbf{r} + 2a + 2r)\,\mathbf{r} - (a + 2r + a^{-1}\mathbf{a} \cdot \mathbf{r})\,\mathbf{r}_Q$.

Other head models

The single sphere head model simplifies calculations of the magnetic fields outside the head, but represents an oversimplification of the head geometry. Huang et al. (1999) developed the **multiple** or **local sphere model** where an optimal sphere is selected independently for each detector. This results in a series of overlapping spheres with a geometry that better approximates the brain and therefore offers a more accurate, but simple solution. More realistic head models require the use of boundary element methods (BEM): these are the most accurate forward solutions used to date (Stenroos et al., 2014), however, they are computationally expensive. Both the single sphere and local sphere models will be used throughout this thesis.

1.2.2 Inverse problem

We now have a model of the magnetic fields outside the head given a known current dipole distribution in the brain. However in MEG, the fundamental problem is to compute the current distribution given the (measured) field. This is called the Inverse Problem and can be formulated as: *given a set of magnetic field measurements outside the head, can we reconstruct the underlying current dipole distribution in the brain?* This is mathematically ill-posed (Hadamard, 1902) since field cancellation means that an infinite number of current distributions can

generate the same field pattern. Nevertheless, optimisation approaches exist, allowing us to solve the problem in light of specific assumptions.

Lead fields

If $m_i(t)$ is the output of a magnetic field detector i ($i = 1, 2, \ldots, N$; where N is the total number of detectors) at a time t, there is a vector field $\mathbf{l}(\mathbf{r}')$ satisfying:

$$m_i(t) = \int_V l_i(\mathbf{r}') \cdot q(\mathbf{r}', t)\, dv', \tag{1.19}$$

and is called the lead field and represents the model of the magnetic fields for a dipole of unit strength at a given position $\mathbf{r}'$. The brain is usually discretised into a number of voxels, j ($j = 1, 2, \ldots, M$; with M being the total number of voxels). Therefore, assuming that only one dipole exists per voxel, we can write:

$$m_i(t) = \sum_{j=1}^{M} l_{i,j} \cdot q_j(t) \tag{1.20}$$

and in matrix form we obtain:

$$\mathbf{m}(t) = \mathbf{L} \cdot \mathbf{q}(t), \tag{1.21}$$

where $\mathbf{q}(t)$ has dimensions $M \times 1$ and $\mathbf{L}$ is the lead-field matrix, of dimensions $N \times M$ containing all the information on how the dipoles map to the detectors.

Equation 1.21 represents the generative model describing the MEG data, $\mathbf{m}$, in terms of the underlying current dipole distribution, $\mathbf{q}$. Mathematically, the process of solving the inverse problem is inverting this equation (finding $\mathbf{q}$ given $\mathbf{m}$ and $\mathbf{L}$). There are a number of ways to solve this, each involving different assumptions. In this thesis we concentrate on a method known as beamforming.

Beamforming

Beamforming is a popular solution to the inverse problem that has been used extensively for EEG and MEG (Van Veen et al., 1997; Vrba and Robinson, 2001). It was originally developed for signal processing in fields like radar, geophysical exploration and communications, amongst others (Van Veen and Buckley, 1988). Using a beamformer, an estimate of electrical source strength, $\hat{\mathbf{q}}_{\boldsymbol{\theta}}$, at a given location and orientation $\boldsymbol{\theta}$ is given by a weighted sum of sensor measurements (see Figure 1.5) so that:

$$\hat{q}_{\boldsymbol{\theta}}(t) = \mathbf{w}_{\boldsymbol{\theta}}^T \mathbf{m}(t). \tag{1.22}$$

Note that the 'hat' notation is used to represent a beamformer estimate; i.e. $\hat{\mathbf{q}}_{\boldsymbol{\theta}}$ is the beamformer estimate of $\mathbf{q}_{\boldsymbol{\theta}}$ made using only the MEG data, $\mathbf{m}$. $\mathbf{w}_{\boldsymbol{\theta}}$ is a vector of weighting parameters (dimension $N \times 1$) tuned to the location and orientation $\boldsymbol{\theta}$. The coefficients, $\mathbf{w}_{\boldsymbol{\theta}}$, have to be selected so that they emphasise activity at $\boldsymbol{\theta}$ while attenuating signals from all other locations, including environmental magnetic interference. Therefore, the weights are derived based on variance minimisation: the overall variance in $\hat{\mathbf{q}}_{\boldsymbol{\theta}}$ is minimised with the linear constraint that signals originating from $\boldsymbol{\theta}$ remain. Mathematically this can be expressed as,

$$\min_{\mathbf{w}_{\boldsymbol{\theta}}} |\langle \hat{q}_{\boldsymbol{\theta}}^2(t) \rangle| \text{ subject to } \mathbf{w}_{\boldsymbol{\theta}}^T \mathbf{l}_{\boldsymbol{\theta}} = 1, \tag{1.23}$$

where $\mathbf{l}_{\boldsymbol{\theta}}$ is the forward field for location and orientation $\boldsymbol{\theta}$, i.e. $\mathbf{l}_{\boldsymbol{\theta}}$ is a model of the magnetic field measured at the N sensors if a dipole of unit amplitude existed at $\boldsymbol{\theta}$ ($\mathbf{l}_{\boldsymbol{\theta}}$ is a column of $\mathbf{L}$).

The most commonly employed solution to this equation is

$$\mathbf{w}_{\boldsymbol{\theta}}^T = \frac{\mathbf{l}_{\boldsymbol{\theta}}^T \mathbf{C}^{-1}}{\mathbf{l}_{\boldsymbol{\theta}}^T \mathbf{C}^{-1} \mathbf{l}_{\boldsymbol{\theta}}}, \tag{1.24}$$

where $\mathbf{C} = \langle \mathbf{m}(t)\ \mathbf{m}(t)^T \rangle$ and is approximated by the data covariance of dimensions $N \times N$ ($\langle \cdot \rangle$ represents the temporal expectation value). The ij^{th} element of $\mathbf{C}$ is the covariance of the data recorded at channels i and j, respectively, and is calculated as

$$C_{ij} = \frac{1}{P} \sum_{p=1}^{P} m_i(t_p) m_j(t_p), \tag{1.25}$$

where P is the total number of time points. In cases where $\mathbf{C}$ is close to singular, this matrix can be regularised, e.g. using: $\mathbf{C}_r = \mathbf{C} + \mu\mathbf{\Sigma}$, where μ is the regularisation parameter and $\mathbf{\Sigma}$ is the noise covariance matrix (usually approximated as a scaled identity matrix, $\mathbf{I}$).

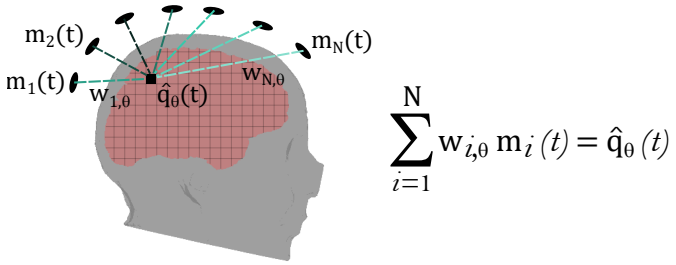


Figure 1.5: **Schematic of the beamforming method.**

It is important to note that an inherent assumption of the beamformer is that spatially separate sources are not temporally correlated.

An important parameter of source reconstruction is the source orientation: so far we have assumed that this is known and represented within $\boldsymbol{\theta}$, but in practice this is not the case. For this reason, the orientation of the reconstructed source is derived as that which gives the maximal signal-to-noise ratio (SNR) for a given location. Given that, in the spherical model, radial sources do not contribute to the signal, the orientation of a dipole is constrained to remain azimuthal to the brain surface. Consequently, the weights for a dipole at location $\mathbf{r}$ are derived at different azimuthal angles ϕ, ranging from 0 to π. The maximal SNR is estimated using the pseudo-Z-statistic, Z, at each angle ϕ, where

$$\mathsf{Z}_{\mathbf{r},\phi} = \frac{\mathbf{w}_{\mathbf{r},\phi}^T \mathbf{C} \mathbf{w}_{\mathbf{r},\phi}}{\mathbf{w}_{\mathbf{r},\phi}^T \mathbf{\Sigma} \mathbf{w}_{\mathbf{r},\phi}^T}, \tag{1.26}$$

Finally, ϕ is selected from the maximum value of $\mathbf{Z}_{\mathbf{r},\phi}$.

In Chapter 3 we use the beamformer in simulations of a whole-head scalp-mounted MEG system. In Chapters 5 and 6 we use the beamformer to process real data from an OPM-MEG instrument.

1.3 Data collection: the MEG system

Neuromagnetic signals are on the order of a few tens to hundreds of femtotesla (fT), around a billion times smaller than the earth's magnetic field. A suitable MEG detector system which is able to detect such fields will also be sensitive to other magnetic fields present (see Figure 1.6), such as unwanted contributions from various environmental interfering sources (cars, elevators, power-line signals, laboratory equipment), from other biomagnetic fields (heart, muscles, eye movement) or even parts of the brain which are not under investigation. Indeed, MEG has been referred to as *"the art of finding a needle in a haystack"* (Vrba, 2002). For this reason, there are two basic technical requirements for measuring the tiny magnetic fields from the brain:

- An array of sensitive magnetic field detectors
- Reduction of environmental and biomagnetic interference

1.3.1 Conventional superconducting MEG systems

The first recording of neuromagnetic signals was made in 1968 with a 2-million turn resistive copper coil (Cohen, 1968). This, for obvious reasons, was impractical, and there was a need for more sensitive instruments to detect small magnetic fields. Highly sensitive detectors of magnetic field based on superconducting and quantum phenomena were being developed, called superconducting quantum interference devices (SQUIDs; Jaklevic et al. (1964); Zimmerman

et al. (1970)) and it was in 1972 when SQUIDs were first used for detection of MEG signals (Cohen, 1972). Following this pioneering work, MEG systems have seen a gradual increase in the number of sensors spaced around the head in order to give whole-head coverage, resulting in the introduction of commercially available devices in the 90's (Knuutila et al., 1993; Vrba et al., 1999) with hundreds of channels.

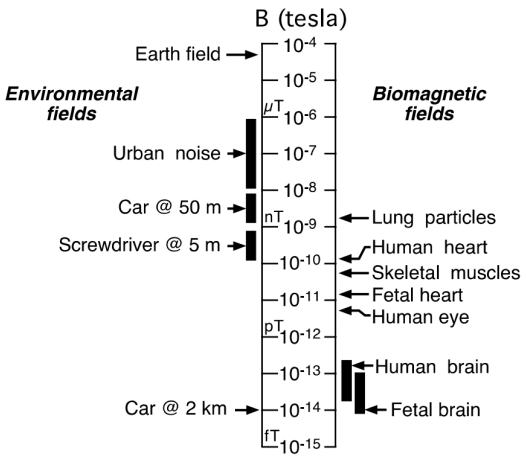


Figure 1.6: **Scale of magnetic fields from environmental and biomagnetic sources.** Adapted from Vrba (2000).

SQUIDs

The SQUID consists of a ring of superconducting material interrupted by two insulating oxide layers called Josephson junctions (JJ). Superconductivity was discovered in 1911 by H. K. Onnes, following speculation that the resistance of metals falls to zero at low temperatures, allowing them to form a perfect conductor (Onnes, 1911). Onnes showed that for some materials, an abrupt transition occurred at a critical transition temperature, T_c.

A theory of superconductivity was proposed by Bardeen, Cooper and Schrieffer in 1957, today known as the BCS theory (Bardeen et al., 1957). They postulated that the superconducting electrons are bound together forming pairs (referred to as Cooper pairs) and act like a boson (rather than two fermions), which means that many are allowed to exist in the same quantum state. In 1962,

B. D. Josephson postulated that, at temperatures $T < T_c$, Cooper pairs should be able to tunnel through the insulating gap (JJ) between two superconductors (Josephson, 1962). This tunnelling process allows the passage of small currents through the SQUID and, if the current becomes greater than a critical value, a drop in potential difference occurs. This voltage modulation is a sinusoidal function of magnetic flux, Φ, through the SQUID loop, and it is this that is used for the detection of the neuromagnetic fields.

Figure 1.7a shows a diagram of a SQUID circuit. A superconducting pick-up coil is connected to a SQUID via mutual inductance. When the bias current through the SQUID exceeds the critical value, the potential difference across the SQUID follows the behaviour shown in Figure 1.7b, when modulated by changing flux through the ring. The SQUID is always made to operate at the steepest part of the curve, represented as the lock point, where dV/dΦ is at its steepest. Feedback circuitry and a second coil ensures the SQUID remains at this lock point. In short, a dc SQUID operates as follows:

1. Neuromagnetic fields induce current in the pick-up coil, which in turn, causes current flow in the signal coil.

2. This current generates a magnetic field that influences the SQUID by induction, causing a change in flux through the ring.

3. Assuming that the critical current is exceeded, a detectable voltage change occurs.

4. SQUID electronics in turn apply a feedback current to counterbalance the induced current, thus balancing the flux through the ring.

5. Magnitude of the required feedback current, measured as a voltage produced across a resistor, is the output of the system and reflects a quantitative measure of magnetic field.

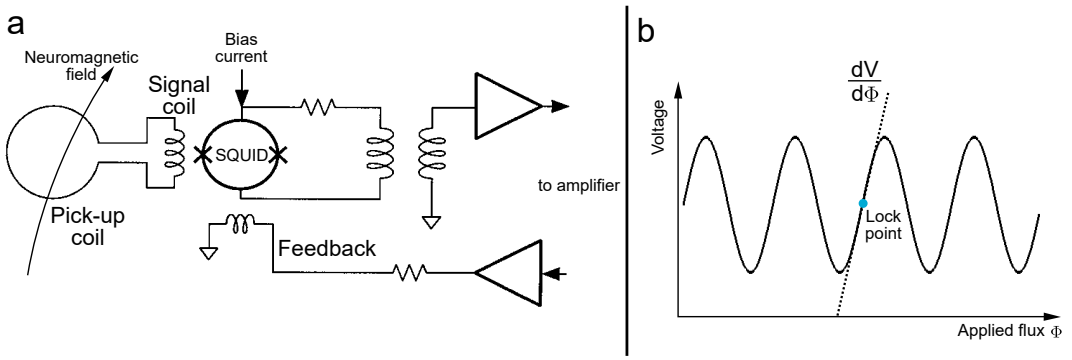


Figure 1.7: **SQUID.** a) Schematic diagram. b) The flux-to-voltage transfer function.

SQUIDs operated in this way offer a sensitive measure of magnetic fields with a typical noise floor of $<$10 fT/$\sqrt{\text{Hz}}$, a bandwidth of several kHz and a dynamic range in the nanotesla (nT) range.

Interference reduction

- **Magnetically-shielded room**

  The most straightforward and reliable way of reducing environmental magnetic disturbances is to house the MEG device inside a magnetically-shielded room (MSR). Different methods exist to make such an enclosure, but the most common is to build the room out of materials with very high permeability (μ-metal). Magnetic fields take the path of highest permeability, meaning that they travel around the walls of the MSR and away from the MEG detectors. Aluminium layers are usually sandwiched between μ-metal walls to shield the MEG by eddy currents from AC sources. MSRs are most effective at shielding high-frequency fields. The MSR installed at the Sir Peter Mansfield Imaging Centre consists of two layers of μ-metal and one layer of aluminium (Vacuumschmelze®), and the remnant static field inside is around 25 nT.

- **Hardwired gradiometers**

  Another effective way of reducing the effect of external magnetic fields is via the use of gradiometric coil configurations. The pick-up coil in Figure

1.7a can have a geometry designed to reduce unwanted signals. Two examples of these pick-up coils are shown in Figure 1.8a. Magnetometers (i) consist of a single loop of wire. A first-order axial gradiometer (ii) has a second loop wound in opposition, which results in the cancellation of a component of the field that passes through both coils (i.e. in a uniform field it reads zero). Figure 1.7b shows how this type of gradiometer reduces external interference from distal sources: the inhomogeneous field produced by nearby sources are effectively measured, whereas the more homogeneous fields of distant sources are cancelled.

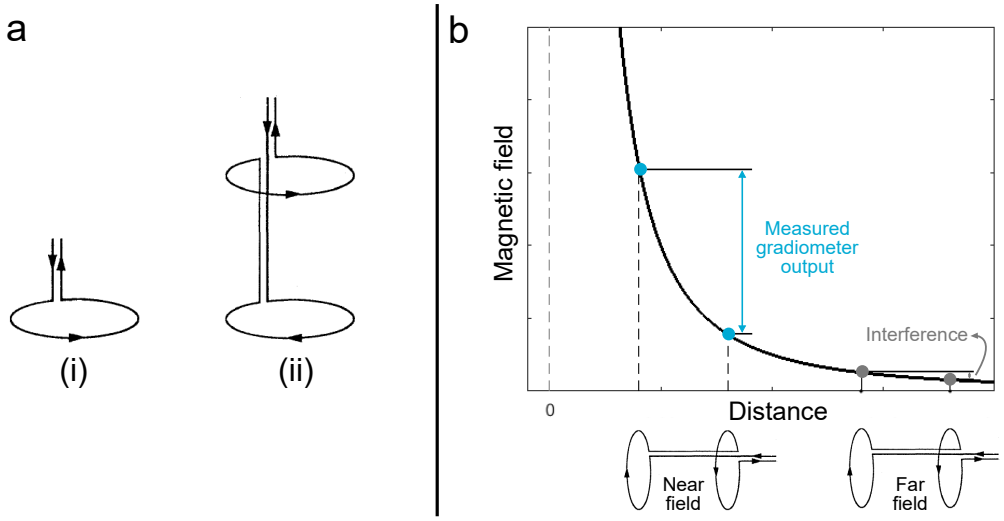


Figure 1.8: **Hardwired gradiometers.** a) Example of two pick-up coils: (i) magnetometer and (ii) axial gradiometer. b) Graph showing the effect of axial gradiometers at cancelling the magnetic field from far sources. Adapted from Hämäläinen et al. (1993) and Vrba (2000).

- **Synthetic gradiometers**

  Hardwired gradiometers are mostly first-order gradiometers, and these, in combination with the shielding afforded by the MSR are sufficient but could benefit from the incorporation of higher-order gradiometric configurations. In principle, it is possible to build hardwired second- and third-order gradiometers, but they are bulky and impractical. An alternative is to "synthesise" a gradiometer (Vrba et al., 1991) by using a combination of reference gradiometers located distal to the head. The CTF™ MEG system

in Nottingham can synthesise third-order gradiometers using an array of 29 reference sensors located distal to the head but within the cryogenic dewar (see Figure 1.9b).

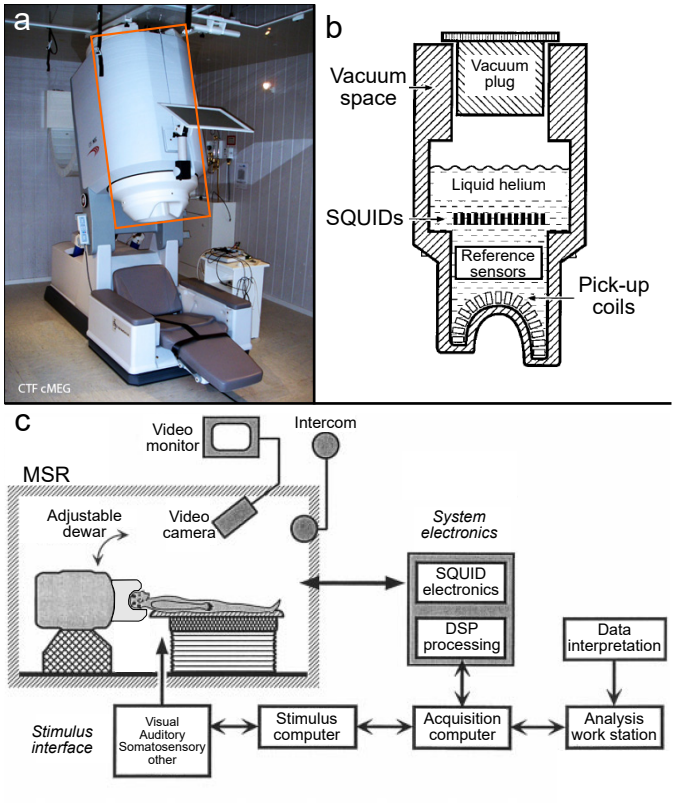


Figure 1.9: **SQUID-based MEG system.** a) CTF^{TM} MEG system at the Sir Peter Mansfield Imaging Centre. b) Inset of (a) showing the inside of the dewar. c) Overview of the experimental set-up. Adapted from (Vrba and Robinson, 2001).

Experimental procedure

Figure 1.9 shows the MEG system at the Sir Peter Mansfield Imaging Centre in Nottingham (a,b), along with a schematic diagram of the experimental instrumentation (c). A subject would be either seated or supine with their head resting inside the dome of the dewar. To minimise head movement, extra padding is usually provided to fit between the head and the surface of the dewar. Three head position coils (at the nasion, left and right pre-auricular points) are attached to the subject to allow for co-registration of the head with the sensor locations and also for tracking movement. It is common to have a 5-mm head

movement tolerance to ensure good co-registration (Gross et al., 2013). Measurements from the SQUIDs are digitised by an electronics rack located outside the MSR, and sent to an acquisition computer that saves the data. A stimulus computer is usually used to provide sensory stimulation, along with other equipment such as projectors, button boxes, earphones, etc. The acquisition and stimulus computers are linked so that markers can indicate the timing of the specific stimuli with respect to the MEG data. Given that the MEG dewar contains liquid helium, safety precautions must be taken: an oxygen monitor is placed inside the MSR, an intercom allows communication between the subject and MEG operator and a video camera gives visual assessment inside the MSR.

1.3.2 Emerging technologies

At the time of writing, all the delivered commercially available MEG devices are based on SQUIDs. They have been the only practical solution to detect the very low amplitude magnetic fields generated by the brain, and indeed they have a number of desirable properties including high sensitivity ($<$10 fT/$\sqrt{\text{Hz}}$), high bandwidth (0-12,000 Hz in a CTF system) and (assuming that the feedback electronics can cope adequately with the sinusoidal flux-to-voltage transfer function) a reasonable dynamic range. However, SQUIDs also have significant limitations, principally brought about by the requirement for cryogenic cooling. This means that SQUIDs must be kept at a reasonable distance from the head, and in fixed locations, limiting both sensitivity and practicality. Further, the purchase and running costs of a SQUID system are high. This means the introduction of new sensor types could have the potential to revolutionise MEG scanning.

The development of alternative magnetic field detectors which overcome some of the disadvantages of SQUIDs has been rapid in recent years. Here, some of these technologies are briefly summarised.

High-temperature SQUIDs (High-T_c SQUIDs)

High-T_c SQUIDs use a superconducting material with a higher transition temperature, allowing the SQUID to operate at liquid nitrogen (77 K), rather than liquid helium temperatures (4 K). Insulation requirements are thus less severe which means that sensor-to-scalp distance could be reduced from a few centimetres to less than 1 millimetre (Andersen et al., 2017), although for multi-channel arrays this may not be feasible. High-T_c SQUIDs have the potential to be more flexible (Riaz et al., 2017), but the improvements on their manufacture are part of an ongoing process. Typically, materials for high-T_c superconductors are difficult to work with, meaning this technology is still not ready for direct translation to MEG technology.

Hybrid SQUIDs (HyQUIDs)

A new variant of a SQUID, the HyQUID™ was developed by Royal Holloway University in 2016 (Shelly et al., 2016) which provides better overall performance and simpler fabrication compared to a SQUID. The HyQUID consists of a superconducting loop, like in a SQUID, with the difference that the weak link is made of a normal conductor (Petrashov et al., 1995). Field detection is based upon a process known as Andreev reflections at a superconductor/metal boundary. A MEG scanner based on HyQUIDs (MEGSCAN®) has been developed by York Instruments Ltd. which has an exclusive license to use the technology. The system is cryogen-free, even though the HyQUIDs are operated in a superconducting environment. This is achieved using recent advances in cryogenics provided by Oxford Instruments, which maintain the superconducting state by pulse tube refrigeration technology. The MEGSCAN dewar is similar in shape to conventional SQUID-based MEG devices, meaning that the sensors are in a fixed array and a gap is maintained between the sensors and the subject's head.

Nitrogen-vacancy (NV) centres

NV centres exploit the isolated electronic spin system of the NV centre in diamond to offer a sensitive measure of very weak magnetic fields (Rondin et al., 2014). They operate at room temperature and have recently been miniaturised, potentially offering a route to scalp-based MEG (Dale and Morley, 2017). However, at the time of writing their sensitivity is significantly lower than that of a SQUID (few hundred picotesla) which means the technology is not ready for application in MEG.

Optically-pumped magnetometers (OPMs)

OPMs exploit the spin properties of alkali atoms, and a technique known as optical pumping, to prepare a gas of atoms such that its opacity to laser light is a sensitive marker of local magnetic field. Their theoretical sensitivity surpasses even that of the SQUID (Dang et al., 2010), and OPMs operate without cryogenic cooling. They have recently been miniaturised (Sander et al., 2012) and commercialised (Shah and Wakai, 2013) and their main advantage is that they can be placed directly on the scalp. Their bandwidth is suited to MEG acquisition (0-150 Hz) and their dynamic range ($\pm$5 nT), though limited, is acceptable.

Of all of the emerging technologies listed above, the one that is closest to application for MEG is the OPM. Indeed, there have been a number of examples of OPMs being used to capture biomagnetic signals from the brain (Xia et al., 2006; Johnson et al., 2010, 2013; Kamada et al., 2015; Colombo et al., 2016; Kim et al., 2014). For these reasons, the next chapter, and the rest of this thesis, will now concentrate on the theory and application of OPMs for MEG measurement.

Chapter 2

Optically-pumped magnetometers

This chapter describes the operation of the optically-pumped magnetometers (OPMs) used throughout this thesis. Following a brief literature review on the use of OPMs for biomagnetic measurement, we move on to the mode of operation of commercially available OPMs made by QuSpin Inc.[1](CO, USA). The fundamental underlying quantum mechanical principles are described and following this, a semi-classical framework is introduced which allows a platform for quantitative assessment of the sensors, which is followed up in Chapter 5.

2.1 Introduction

As introduced in the previous chapter, optical interrogation of alkali atoms contained in a vapour cell constitutes one of the most sensitive ways to measure magnetic fields. Alkali OPMs implement this technique, and have been proved to reach sensitivities comparable (Allred et al., 2002) or in some cases even better than SQUIDs (Kominis et al., 2003; Dang et al., 2010). The set-up required for achieving such sensitivity, however, is often bulky and laboratory-based. Nevertheless the first ever MEG recording using a laboratory OPM set-up was reported in 2006 (Xia et al., 2006) inside a human-sized shield during auditory stimulation. Results showed clearly that the auditory evoked response was measurable with a high SNR.

[1] http://quspin.com/

The last two decades have seen rapid advances in the miniaturisation of OPMs. Methods originally developed for chip-scale atomic clocks were used to build the first microfabricated OPMs (Schwindt et al., 2017, 2007). This initial work, whilst still far from reaching the sensitivity similar to that of a SQUID (sensitivities were of the order of a few picoteslas), showed the potential of the technology to be scaled down in size and weight and leave the laboratory bench. A few years later, table-top set-ups showed sensitivities of a few tens of femtoteslas (Shah et al., 2007) and even reached below 10 fT (Griffith et al., 2010; Shah and Romalis, 2009), which had been the target sensitivity for SQUIDs used in MEG. The introduction of techniques used in manufacturing microelectromechanical systems (MEMS) added to the excitement of having compact magnetometers for biomedical applications, and led to the first "packaged" microfabricated OPMs. Some examples of compactly packaged OPMs are shown in Figure 2.1: sensors in panels (a), (b) and (f) were developed at the National Institute of Standards and Technology (NIST); the sensor in (c) at Sandia National Laboratories; the sensor in (d) was developed at Kyoto University and the sensor in (e) at QuSpin Inc.

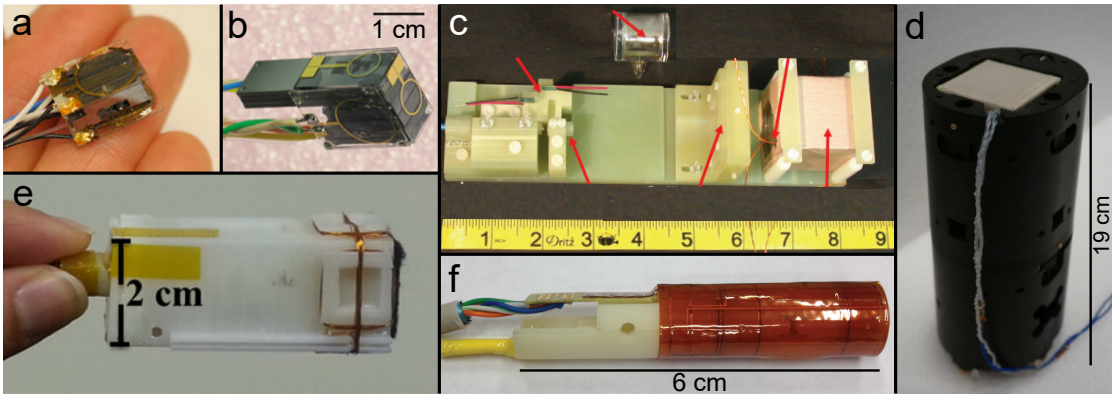


Figure 2.1: **The first compact OPMs.** a) Sander et al. (2012). b) Mhaskar et al. (2012). c) Johnson et al. (2013). d) Kamada et al. (2015). e) Shah and Wakai (2013). f) Sheng et al. (2017).

Some of these sensors have been used to measure MEG signals: for example, recent papers have described the successful detection of phase-locked evoked responses generated by auditory (Johnson et al., 2010, 2013) or somatosensory

(Sander et al., 2012) stimulation. Other groups have shown how sensors positioned over the occipital lobe enable detection of the induced changes in the alpha (8–13 Hz) rhythm generated by opening and closing the eyes (Sander et al., 2012; Kamada et al., 2015). In addition, multi-channel measurements have been demonstrated (Kim et al., 2014; Colombo et al., 2016), showing the potential of OPMs to become the fundamental building block for a new generation of whole-head MEG systems.

2.1.1 Principle of operation

The OPMs used in the studies outlined above differ on many aspects, such as the materials used to build them, optical configuration, sensitivities and even the strategy used to read out the field. However, their working principle can be outlined with a single description. Most optical magnetometers rely on a measurement of the evolution of an atomic spin ensemble in a magnetic field. The working principle can therefore be described in three steps (see Figure 2.2):

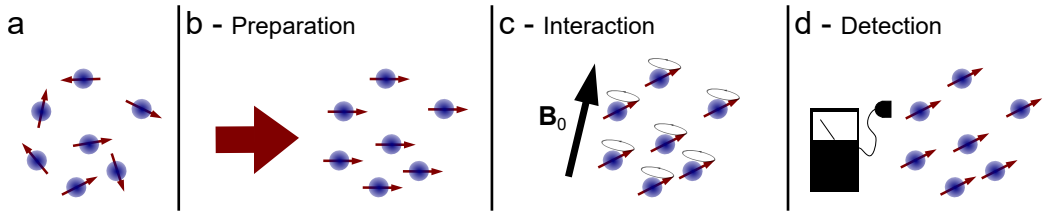


Figure 2.2: **Principle of operation.** a) An ensemble of atomic spins are initially randomly oriented. b) Atomic spins are spin polarised. c) Interaction with the magnetic field $\mathbf{B}_0$ causes precession of spins about the field at a rate proportional to its magnitude. d) Detection of the evolution of spins provides an indirect measurement of the magnetic field.

1. Atoms are prepared in a well-defined spin state e.g. a specific hyperfine state (or specific orientation with respect to an external magnetic field). The atomic ensemble therefore becomes spin polarised.

2. Atomic spins interact with the magnetic field in their environment, causing

precession at the Larmor frequency:

$$\omega_L = \gamma \left| \mathbf{B}_0 \right| \tag{2.1}$$

where γ is the gyromagnetic ratio of the atoms. I.e. precession rate is proportional to the magnitude of the field $\mathbf{B}_0$.

3. The altered state of the atoms is measured via assessment of the change in magnetisation and the effects of the magnetic field are deduced.

The most common technique used to spin polarise the atomic ensemble is optical pumping (Happer, 1972) (hence the name *optically-pumped* magnetometers). Through this mechanism, the angular momentum of atoms can be reoriented by illuminating them with circularly polarised light, which is resonant with an optical transition of the atoms. This produces a coherent alignment of the spins in the atomic spin ensemble. The light used to polarise the atoms can also be used to read out the spin state of the atoms, and along with it, the effect of the external magnetic field on the spins (thus forming a magnetometer).

Having now introduced the basic scheme by which OPMs function, we now focus down on the principles underlying the QuSpin OPM.

2.1.2 The QuSpin sensor

Commercialisation of OPMs (QuSpin, Osborne et al. (2018)) and scalability of their manufacturing process have made it possible to envisage MEG systems based on these devices. Figure 2.3a shows a photograph of a Gen-1 QuSpin Zero-Field Magnetometer (QZFM), which has dimensions of 13 mm$\times$19 mm$\times$110 mm. Panel (b) shows a schematic representation of the sensor head, along with its internal optical components. These are labelled in panel (c). A 3$\times$3$\times$3-mm^3 vapour cell filled with a gas of rubidium-87 (^{87}Rb) sits at the centre of the sensor head, and its centre point is 6.5 mm from the external surface of

the unit. A laser diode emitting 795-nm light is used for optical pumping. The laser light is collimated by a plano-convex lens and reflected through 90 degrees using a prism before passing through the cell. The light transmitted is reflected again and directed towards a photo-detector, which monitors its intensity. Also, electric heaters and on-board electromagnetic coils are placed around the cell. All the components inside the sensor are non-magnetic (to the greatest extent possible).

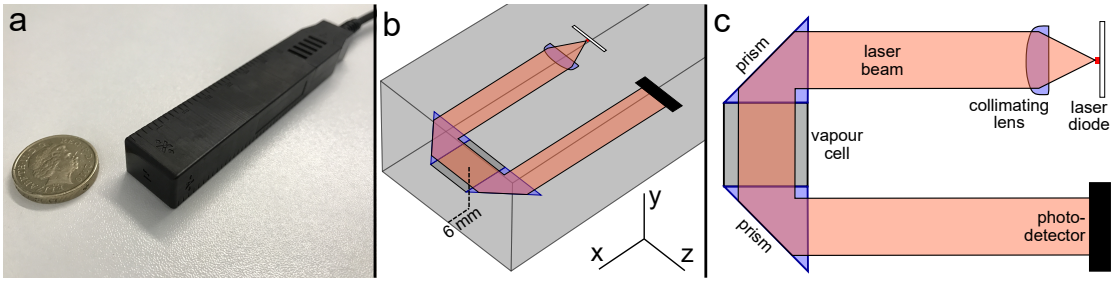


Figure 2.3: **The QuSpin OPM device.** a) Photograph of a QZFM QuSpin sensor. b) Schematics of the inside of the sensor. c) Basic operation and optics.

2.2 Atomic energy levels

In order to understand precisely how the QuSpin sensor works, first, the basic principles underlying the atomic energy levels in ^{87}Rb are reviewed. Alkali metals, like ^{87}Rb, are useful in many different applications because their outer shell contains a single unpaired electron, which can be easily manipulated. In addition, rubidium atoms have a low melting temperature and their optical energy levels are easily accessible using commercial infrared laser diodes. OPMs exploit the energy structure of the ground and excited states to polarise ^{87}Rb atoms, so it is useful to review the energy levels of the atom.

The *wavefunction* of an atomic electron can be described by four quantum numbers:

- The principal quantum number, n

- The azimuthal quantum number, l, which describes the orbital angular momentum of the electron. l can take integer values between 0 and n–1, and different states are denoted by letters: e.g. $l = 0$ corresponds to the s state, $l = 1$ to p, $l = 2$ to d, $l = 3$ to f, ...
- The magnetic quantum number, m_l, which takes integer values between $-l$ and $+l$ and (loosely) represents the z-projection of the orbital angular momentum
- The spin quantum number, s, describes the electronic spin

In ^{87}Rb, the ground state is an s shell with orbital angular momentum $L = 0$ and the first excited state is a p shell with $L = 1$. The valence electron has spin $S = 1/2$ and a total angular momentum J which is the sum of its orbital angular momentum and spin:

$$J = L + S. \tag{2.2}$$

Energy level transitions between ground and excited states (or vice versa) can occur via absorption (or emission) of light, causing changes in the total angular momentum of the valence electron.

Furthermore, the total angular momentum of the atom, F, is given by the sum of the total electron angular momentum, J, and nuclear spin, I:

$$F = J + I. \tag{2.3}$$

The nuclear spin of an atom is an intrinsic property and in ^{87}Rb is $I = 3/2$. The total angular momentum of the atom dictates its magnetic moment, μ_F, so that

$$\mu_F = \gamma F, \tag{2.4}$$

where γ is again the gyromagnetic ratio, which for ^{87}Rb is approximately 7 Hz/nT (4.6 Hz/nT in *SERF* regime, to be discussed later).

2.2.1 Fine structure

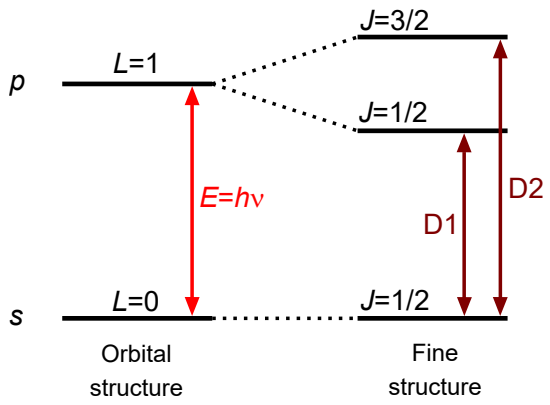


Figure 2.4: **Fine structure.** Energy splitting due to fine structure of the ground and excited states for an alkali atom. Light with photon energy $E = h\nu$ causes transitions between states.

Interaction between the electron's spin S and orbital angular momentum L causes a splitting of energy levels (see Figure 2.4), and this is referred to as the *fine structure* of the atom. These energy levels are found by taking integer steps in the form:

$$|L - S| \leqslant J \leqslant L + S. \tag{2.5}$$

Therefore, in the ground state there is only one possible value $J = 1/2$, while in the first excited state, the fine structure splits this state into two levels: $J = 1/2$ and $J = 3/2$. The energy transitions between the ground state $(L = 0, J = 1/2)$ and the excited states $(L = 1, J = 1/2)$ and $(L = 1, J = 3/2)$ levels are referred to as the D1 and D2 transitions, respectively. These transitions can be selectively chosen by specifying the appropriate frequency, ν, of the incident light, given that the photon energy

$$E = h\nu, \tag{2.6}$$

where h is Planck's constant. For ^{87}Rb, the D1 transition corresponds to the energy of a 795-nm wavelength photon.

2.2.2 Hyperfine structure

The *hyperfine structure* is the result of the interaction between the electron and nuclear spins, resulting in a further splitting of the atomic levels into states of total atomic spin $F = I + J$ (see Figure 2.5). The ground $(L = 0, J = 1/2)$ and excited $(L = 1, J = 1/2)$ states are split into levels with $F = I \pm 1/2$, i.e. $F = 1$, 2, separated by the hyperfine energy splitting.

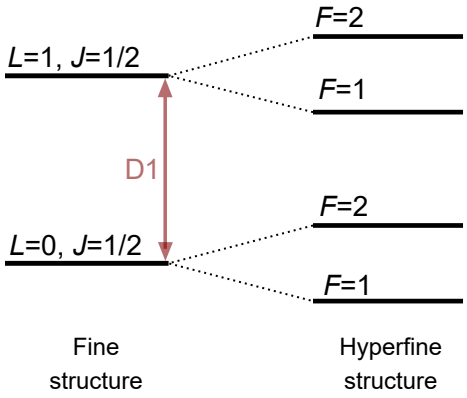


Figure 2.5: **Hyperfine structure.** Energy splitting due to hyperfine structure of the ground and excited states involved in the D1 transition.

2.2.3 Zeeman splitting

Finally, interaction with an external magnetic field further splits the hyperfine structure into different Zeeman sublevels with projection $m_F = \{-F, -F + 1, \ldots, F - 1, F\}$ of the atomic angular momentum F along some quantization axis (in absence of magnetic field, defined by the direction of the laser propagation through the atoms). The ground-state Zeeman sublevels are shown in Figure 2.6. The energy splitting depends on the magnetic field strength.

2.3 Optical pumping

As mentioned above, optical pumping involves using laser light to drive a large population of atoms into a specific energy level. The valence electron of ^{87}Rb

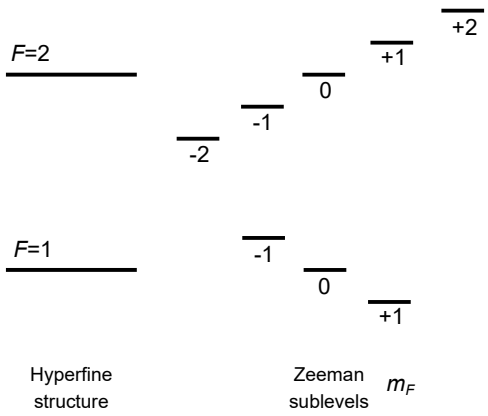


Figure 2.6: **Zeeman sublevels.** Energy splitting of the hyperfine levels of the ground state due to an external magnetic field, resulting in different m_F sublevels.

atoms will change sublevels (i.e. orbital angular momentum – D1 transition) when the atomic sample is irradiated with 795-nm laser light, as shown in Figure 2.5. Usually circularly polarised light is used, which means that all photons have the same spin projection along the beam's propagation (e.g. $\hat{\mathbf{z}}$). For left circularly polarised light, all photons have angular momentum of $+1$ along this axis which will add angular momentum to the atom. Therefore, only transitions causing a change of $\Delta m_F = |m_F(\text{final}) - m_F(\text{initial})| = +1$ will occur. At the same time, atoms may spontaneously emit light, decaying back to the ground state. They do so by emitting a randomly polarised resonant photon that can depolarise another atom if reabsorbed. These two effects (D1 transition pumping and spontaneous emission) will eventually force the atom into the level with the lowest orbital angular momentum $(L = 0)$, i.e. the ground state, and highest atomic angular momentum $(F = 2, m_F = +2)$ as shown in Figure 2.7. Once the atom is in this state, called the *dark state*, it becomes unaffected by the laser light, because of the unavailability of a level with $m_F > +2$: the atomic ensemble becomes transparent to the laser light, which passes through the vapour cell unaffected.

As the laser optically pumps the atoms into this transparent steady state, a strong net magnetisation aligned along the laser axis, is produced in the gas. The gas is said to be spin polarised and becomes magnetically sensitive. Unfortunately, this polarisation is eliminated by collisions between polarised and

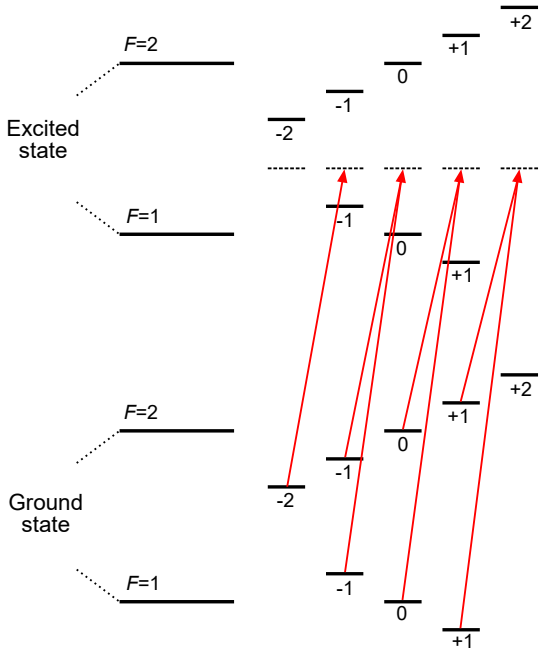


Figure 2.7: **Schematics of the optical pumping mechanism.** Circularly polarised light causes atomic transitions with $\Delta m_F = +1$.

unpolarised atomic species, since the atoms can exchange their spin via collisions. This process is known as spin-exchange (SE) relaxation, and counters the effect of optical pumping, returning the gas to its initial state of poor magnetic sensitivity. However, it is possible to minimise the SE effect by working in a very low magnetic field environment and at high atomic density.

2.4 Zero field and spin-exchange suppression

At high atomic densities, spin-exchange collisions will occur frequently. In such a collision between two atoms, the electron spin orientation in both atoms can be reversed, causing a redistribution among the Zeeman sublevels, leading to relaxation because atoms in the two hyperfine levels precess in opposite directions:

$$\omega_+ = \gamma \left|\mathbf{B}_0\right| = -\omega_- \tag{2.7}$$

where the subscripts denote the hyperfine levels $F = I \pm 1/2$. The sensitivity of a magnetometer generally improves as the number of atoms increases, but this

improvement is negated by the spin-exchange collisions that limit the polarisation lifetime. However, Happer and Tang (1973) discovered that at extremely high atomic densities, and near zero fields, the spin-exchange rate (R_{SE}) will be larger than the precession frequency, and an individual atom will precess by only a small angle between SE collisions. Each atom samples the different sublevels in a short period of time, and the entire atomic ensemble precesses coherently. This is referred to as the Spin-Exchange Relaxation-Free (SERF) regime (Allred et al., 2002), and OPMs are often described as zero-field or SERF magnetometers. This is shown in Figure 2.8, with the R_{SE} increasing by a factor of 10 between each plot (top to bottom, left to right). If R_{SE} is small compared to the Larmor frequency, then an individual atom spends a longer period of time in one hyperfine level. The coherence time of the entire ensemble is limited. As R_{SE} increases, atoms spend shorter times in a particular state between collisions, and a single precession frequency is observed.

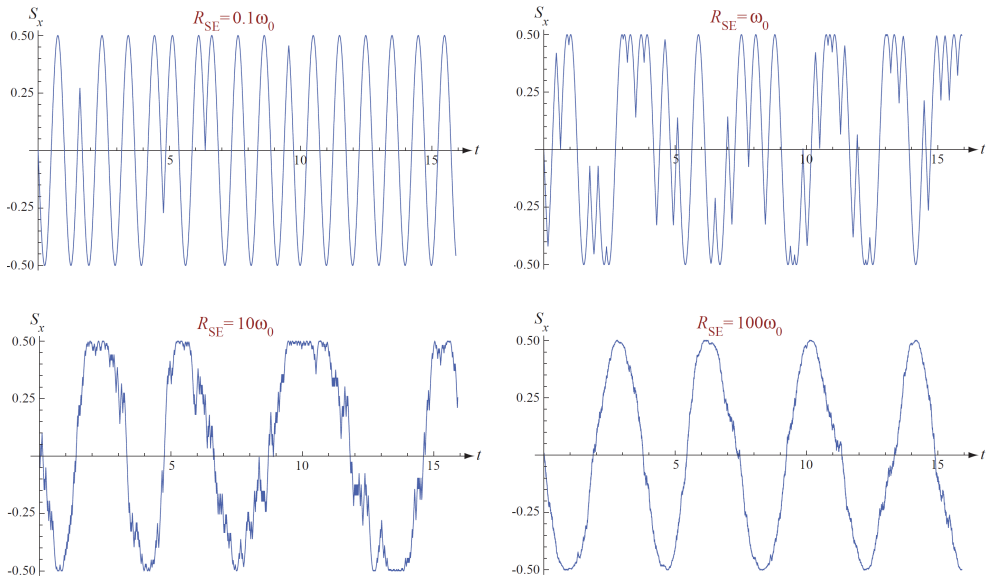


Figure 2.8: **SERF.** Spin-exchange rate (R_{SE}) increasing by a factor of 10 between plots. ω_0 represents the Larmor frequency. When R_{SE} is sufficiently fast, the atomic ensemble precess coherently at a net frequency slower than ω_0. Adapted from Seltzer (2008).

To optimise rubidium density in the vapour cell of the QZFM sensor, the resistive heaters around the cell are used to electrically heat the gas to around 150 °C to increase the density such that R_{SE} exceeds the Larmor precession

frequency, and the spins are in the SERF regime. The cell is inside an oven to minimise heat loss and provide a reasonable surface temperature of the sensor housing.

2.5 Signal equations

After optical pumping and spin-exchange suppression, a large steady-state polarisation, **P**, exists within the vapour cell, along the direction of the laser ($\hat{\mathbf{z}}$). This polarisation can be described using Bloch equations (Bloch, 1946):

$$\frac{d\mathbf{P}}{dt} = \mathbf{P} \times \gamma\mathbf{B} - \frac{1}{\tau}\left(\mathbf{P} - P_0'\hat{\mathbf{z}}\right), \tag{2.8}$$

where **B** is the field within the cell, $\tau = (R+1/T_2)^{-1}$ is the atomic spin coherence time, which is a function of both the optical pumping rate, R, and the relaxation time T_2 and P_0' is related to the equilibrium polarisation ($P_0' = P_0 R\tau$ with P_0 being the equilibrium polarisation).

In the steady state, $d\mathbf{P}/dt = 0$, and the solution to Equation 2.8 becomes:

$$\begin{aligned} P_x &= \frac{B_y/(\gamma\tau) + B_x B_z}{(1/\gamma\tau)^2 + B_x^2 + B_y^2 + B_z^2} P_0' \\ P_y &= \frac{-B_x/(\gamma\tau) + B_y B_z}{(1/\gamma\tau)^2 + B_x^2 + B_y^2 + B_z^2} P_0' \\ P_z &= \frac{(1/\gamma\tau)^2 + B_z^2}{(1/\gamma\tau)^2 + B_x^2 + B_y^2 + B_z^2} P_0' \end{aligned} \tag{2.9}$$

The photo-detector detects changes in P_z, and we are assuming the field we measure is B_x, along the $\hat{\mathbf{x}}$ axis, perpendicular to the laser. In zero-field conditions, the sensor on-board coils minimise the field inside the cell to provide

$B_y = 0$ and $B_z = 0$; therefore, the previous equations can be simplified further:

$$\begin{aligned} P_x &= 0 \\ P_y &= \frac{-\gamma\tau B_x}{1+(\gamma\tau B_x)^2} P_0' \\ P_z &= \frac{1}{1+(\gamma\tau B_x)^2} P_0' \end{aligned} \tag{2.10}$$

These curves are plotted as a function of B_x in Figure 2.9, showing the sensitivity to changes in the magnetic field along $\hat{\mathbf{x}}$. The change in polarisation along the direction of the laser (P_z) has a Lorentzian line shape, and this is referred to as the zero-field or Hanle resonance (Hanle, 1925). The full width at half maximum (FWHM) of this zero-field resonance equals to $1/\gamma\tau$ and is around 30 nT in a QZFM sensor.

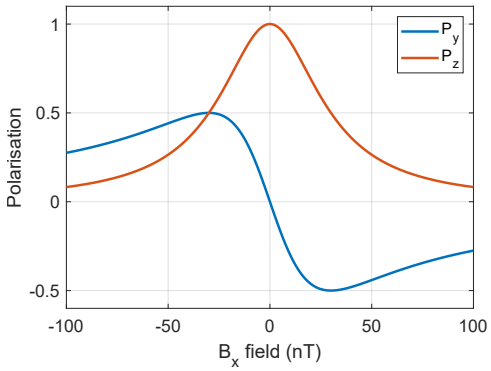


Figure 2.9: **Solutions to Bloch equations in zero field.** Polarisation P_z along the axis of the laser $\hat{\mathbf{z}}$, in orange, showing an absorption profile. Polarisation P_y along the other axis $\hat{\mathbf{y}}$, in blue, shows a dispersion profile. Value of $1/\gamma\tau$ in Equation 2.10 was set to 30 nT.

There are two difficulties associated with measuring the fields in this way. The first one is that this set-up is sensitive to noise (Kastler, 1973) and the second is that, given the symmetric nature of the Lorentzian shape, it will give the same output for positive and negative changes in field of the same amplitude. This can be overcome by performing an amplitude modulation of the polarisation: the on-board coil generates an oscillating magnetic field of magnitude b_x in the form $\delta B_x = b_x \cos \omega t$ where ω is the modulation frequency, much higher than the

Larmor frequency (the QZFM uses $\omega = 923$ rad·Hz). Equation 2.8 then becomes:

$$\frac{d\mathbf{P}}{dt} = \mathbf{P} \times \gamma \left[\mathbf{B} + (b_x \cos \omega t)\hat{\mathbf{x}}\right] - \frac{1}{\tau}\left(\mathbf{P} - P_0'\hat{\mathbf{z}}\right). \tag{2.11}$$

The simple steady-state solution is no longer valid, however, a solution was obtained by Cohen-Tannoudji et al. (1970); when $B_y = B_z = 0$, the component P_z oscillating at the modulation frequency ω is given by:

$$P_z = \frac{\gamma\tau B_x}{1 + (\gamma\tau B_x)^2} J_0\left(\frac{\gamma b_x}{\omega}\right) J_1\left(\frac{\gamma b_x}{\omega}\right) P_0' \sin \omega t, \tag{2.12}$$

where J_n are Bessel functions of the first kind. While the inclusion of these functions complicates the signal equation, they evaluate to a constant term and thus we can write:

$$P_z \propto \frac{\gamma\tau B_x}{1 + (\gamma\tau B_x)^2} P_0' \sin \omega t. \tag{2.13}$$

Now, after demodulation via lock-in detection, the output signal is a dispersion curve (see Figure 2.10) which means that positive and negative amplitude changes can be discriminated.

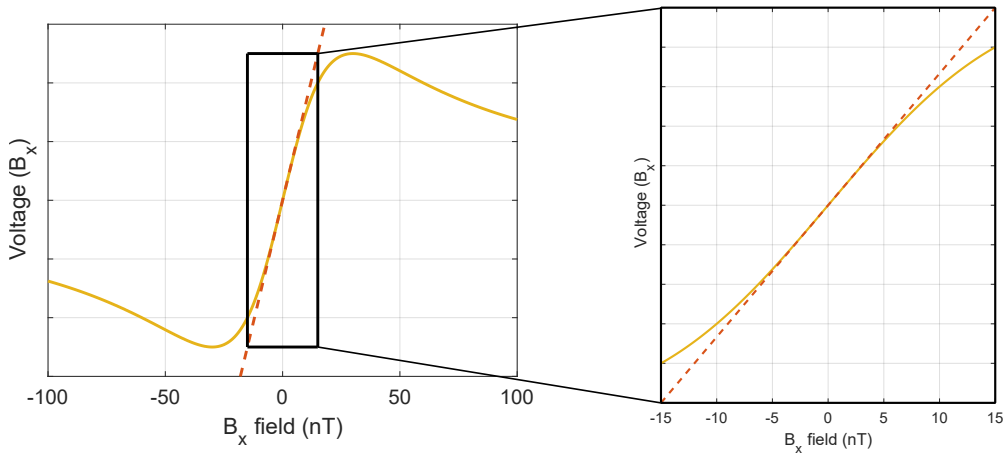


Figure 2.10: **Magnetometer response.** The voltage output is a function of the magnetic field along the sensor's sensitive axis ($\hat{\mathbf{x}}$) and has a dispersion shape, with maximum slope at zero field. The response is linear near zero field, as shown in the inset.

It should be noted that the response of the sensor is approximately linear around zero field, as shown in the inset of Figure 2.10.

2.6 Summary

In summary this chapter has provided a theoretical overview of the physics behind OPMs, focussing on the QuSpin device in particular. A quantitative assessment of its operation has been described, and it will be followed up in Chapter 5.

Chapter 3

Potential advantages of OPMs for MEG

In this chapter a set of simulations is described. A hypothetical MEG system based on OPMs is compared to the current state-of-the-art SQUID-based system. Forward modelling was used to assess potential advantages in SNR (afforded by OPMs being closer to the head) and inverse modelling (beamforming) was used to assess improvements in source reconstruction accuracy and spatial resolution. Results show that OPM-based MEG could potentially offer a step change in the utility of MEG. However that potential is critically dependent on accurate modelling as well as practical OPM array construction.
The work presented here was published in PLoS One in 2016 (Boto et al., 2016).

3.1 Introduction

Despite its excellent potential, MEG is limited by a low SNR and restricted spatial resolution. This is mainly due to the low amplitude of the biomagnetic fields being measured. Extremely sensitive magnetic field detectors are used, and until recently, superconducting quantum interference devices (SQUIDs) have been the only sensors with sufficient sensitivity to record neuromagnetic signals. However, SQUIDs themselves impose a number of limitations: they require the use of cryogenics, making MEG systems bulky and expensive to maintain. This also

means that a vacuum must be maintained between the pick-up coils and the head, thus limiting the minimum separation between the brain and detectors to 3–6 cm for an adult's head. Sensors are held in a fixed position within a one-size-fits-all helmet, meaning that the brain-to-sensor distance will be greater for subjects with smaller heads, e.g. children. In addition, the inflexibility of the sensor placement means that some brain regions have poorer coverage than others (e.g. temporal lobe).

Recently, alternative magnetic field detectors like the OPMs (Kominis et al., 2003) described in Chapter 2 and high-T_c SQUIDs (Öisjöen et al., 2012) have reached the sensitivities required for MEG recordings. In particular OPMs, which do not require cryogenics, have been developed such that they have a small footprint (Sander et al., 2012) meaning that a large number of sensors can be placed flexibly and directly on someone's head, and whole-head coverage is feasible. In principle, the advantages afforded by an OPM-based MEG system are obvious: bringing sensors closer to the head will increase the measured signal (assuming noise floors of OPMs and SQUIDs are comparable) and consequently SNR. Although this result is expected, many critical questions remain unanswered: *What quantitative improvement in SNR might be expected and how does it change with cortical location? How would this SNR gain affect source reconstruction accuracy (following inverse modelling)? How would an OPM system be impacted by the accuracy of modelling algorithms? What would the gain in spatial resolution be compared to current systems?* In addition, the number of sensors required remains an open question.

In this chapter, forward field simulations are used in order to quantify the improvement in sensitivity of an OPM system compared to a current state-of-the-art SQUID-based MEG system. Following this, a beamformer spatial filtering approach is used to quantify the advantages of an OPM system for source reconstruction. We examined reconstruction accuracy of beamforming for single dipoles. In addition, by combining dipolar sources of interest with interfer-

ence generators, we examined the efficacy of interference rejection in OPM and SQUID systems. We investigated how the accuracy of magnetic field modelling (i.e. accuracy of the forward model) impacts the OPM and SQUID system results. Finally, we examined the spatial resolution of OPM and SQUID systems, its reliance on the number of MEG channels, and how this might impact connectivity metrics.

3.2 Methods

3.2.1 Simulated systems

Simulated SQUID (sSQUID) system

For all simulated SQUID-based measures, we employed the third-order, synthetic gradiometer configuration of a 275-channel CTF whole-head MEG system (MISL, Canada). This system contains 275 radially-oriented, axial gradiometers with a 5-cm baseline, along with a 29-channel reference array that is used to construct third-order synthetic gradiometers (Vrba and Robinson, 2002). The position of the head within the MEG helmet was based on an experimental recording, and was determined by using three head position indicator coils attached to the subject's head (nasion, left pre-auricular and right pre-auricular fiducial markers). In this system, the minimum distance from the scalp surface to the closest detector coil is 1.7 cm; this would assume that the scalp is touching the surface of the MEG helmet (which of course is not simultaneously achievable for all scalp locations). In the simulations used here, the subject was positioned with the back of their head touching the back of the helmet, meaning that the largest scalp-to-sensor distance was at the front of the head for the sSQUID system. A high resolution anatomical MRI (1-mm^3 resolution), including fiducial markers, was available for this subject allowing complete registration of the MEG sensor

geometry to the brain anatomy.

Simulated OPM (sOPM) system

In the simulated OPM system, measurement locations were 4 mm from the scalp surface, a distance which is realistic for available SERF OPMs (Sander et al., 2012). The arrangement of sensors was determined by the projection of the 275 sensor locations from the sSQUID system onto the scalp of the same individual used for the sSQUID simulations. Given the size of current micro-fabricated OPM devices ($\sim$1 cm^2 footprint) such a 275-channel system is conceivable. The scalp surface was extracted from the anatomical MRI using Iso2Mesh[1] (Fang and Boas, 2009). To ensure equivalence of the sSQUID and sOPM systems for sensitivity comparison, the sOPM system was also configured with its sensors forming radially-oriented axial gradiometers (5-cm baseline). Note however that for beamformer measurements (see later) we consider OPM magnetometers.

Both simulated set-ups are plotted in Figure 3.1.

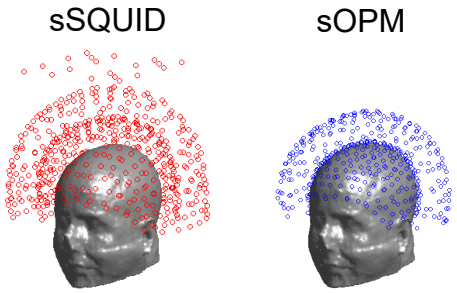


Figure 3.1: **Simulated systems**. The left panel shows the coil arrangement for the sSQUID system, based on the axial gradiometer configuration of the 275-channel CTF MEG instrument. The right panel shows the sOPM system.

In both the sOPM and sSQUID simulations, simulated dipoles were located on the cortical surface, which was extracted as a mesh from the anatomical MRI using Freesurfer[2] (Fischl et al., 2001). This meant that 21,401 individual dipoles could be located at the vertices of the triangular cortical mesh, with each dipole oriented perpendicular to the cortical surface. In order to simulate magnetic fields at the individual sensor locations, a multiple local sphere head model was used (Huang et al., 1999) in conjunction with the forward model derived

[1] `http://iso2mesh.sourceforge.net/`
[2] `http://surfer.nmr.mgh.harvard.edu/`

by Sarvas (1987). Gradiometers were formed via a subtraction of the radial field components through each gradiometer loop (in the case of the sSQUID) or through two OPMs in the case of the sOPM. Third-order gradiometers for the sSQUID were constructed using weighting coefficients from the real MEG recording.

3.2.2 Comparison of SNR

Assuming an equivalent noise floor ($\lesssim$10 fT rms/$\sqrt{\text{Hz}}$) for the sSQUID (Vrba, 2002) and the sOPM systems (both in magnetometer (Allred et al., 2002) and gradiometer configurations), the difference in field magnitudes at the sensors can be used to calculate the gain in SNR afforded by the sOPM system (thus, in the remainder of this chapter, all SNR calculations assume equivalent noise floors for the sSQUID and sOPM). Measured fields at each sensor were simulated for each possible dipole location in the cortex, assuming a dipole moment, $|\mathbf{q}| = 1$ nAm. For every cortical location, j, we calculated the expected output (i.e. the forward field) $\mathbf{l}_j$ for all 275 MEG channels for both systems (therefore $\mathbf{l}_j$ has dimensions of $N_{ch} \times 1$, being N_{ch} the number of channels). The Frobenius norm, f_j, of the forward field vector $\mathbf{l}_j$ was then computed as,

$$f_j = |\mathbf{l}_j|_F = \sqrt{\sum_{j=1}^{N_{ch}} |\mathbf{l}_j|^2}, \tag{3.1}$$

and the comparison of the sSQUID and sOPM systems was derived as,

$$\text{ratio}_j = \frac{f_{j,\text{OPM}}}{f_{j,\text{SQ}}}. \tag{3.2}$$

This ratio, which effectively represents the change in measured signal (and SNR) afforded by moving from the sSQUID to the sOPM system, was calculated at each source location on the cortical surface.

3.2.3 Beamformer reconstruction accuracy

Single dipoles

To examine the accuracy of source reconstruction for our two systems, we first simulated a number of sets of MEG data. A source time course $\mathbf{q}_j$, at cortical location j, containing a total of N time points was simulated as Gaussian-distributed random data with a standard deviation of 5 nAm. Note here that $N = f \cdot \Delta$, where f is sampling frequency and Δ represents the duration of the simulated recording. This dipole signal was projected through the forward field vector for location j, $\mathbf{l}_j$, and simulated MEG data were generated as

$$\mathbf{m} = \mathbf{l}_j \mathbf{q}_j + \mathbf{e}, \tag{3.3}$$

with dimensions of $N_{ch} \times N$. Here, $\mathbf{e}$ represents noise which was generated as normally-distributed random data with a standard deviation of 50 fT. A single set of MEG data, $\Delta = 600$ s ($N = 360,000$) in duration, was simulated for each of the 21,401 possible dipole locations on the cortical mesh. This was done twice using forward fields computed for the sSQUID and sOPM systems. The SNR of these data was dependent on the cortical location, and varied from 0 to 3 for the sSQUID system and 0 to 24 for the sOPM system (note here SNR is computed as the standard deviation of the signal at the maximally affected channel divided by the mean noise). The difference in SNR between systems was purely a result of the proximity of the sensors to the scalp.

To compare the accuracy of source reconstruction in the two systems, a beamformer spatial filter was implemented. As introduced in Chapter 2, the beamformer reconstruction is given by

$$\hat{\mathbf{q}}_j = \mathbf{w}_j^T \mathbf{m}. \tag{3.4}$$

Note this is equivalent to Equation 1.22, but rather than the source being indexed by $\boldsymbol{\theta}$, which represents location and orientation, the orientation was assumed to be known (and perpendicular to the extracted cortical surface). Consequently, j only indexes dipole position.

The beamformer equation thus becomes

$$\min_{\mathbf{w}_j} |\langle \mathbf{q}_j^2 \rangle| \text{ subject to } \mathbf{w}_j^T \mathbf{l}_j = 1, \tag{3.5}$$

and the regularised solution

$$\mathbf{w}_j^T = \frac{\mathbf{l}_j^T \{\mathbf{C} + \mu\boldsymbol{\Sigma}\}^{-1}}{\mathbf{l}_j^T \{\mathbf{C} + \mu\boldsymbol{\Sigma}\}^{-1} \mathbf{l}_j}. \tag{3.6}$$

Recall that $\mathbf{C}$ is the data covariance matrix, $\boldsymbol{\Sigma}$ represents the noise at each of the MEG channels and μ (the regularisation parameter) was set to 0.001 in order to maximise spatial resolution. Beamforming was applied in this way for all of the 21,401 simulated MEG datasets. In order to determine temporal reconstruction accuracy, the Pearson correlation coefficient was measured between the original simulated dipole time course data, $\mathbf{q}_j$, and the beamformer-reconstructed time course data, $\hat{\mathbf{q}}_j$. These correlation coefficients were computed for the sSQUID and sOPM systems and are denoted as $r_{\text{SQ}}(\mathbf{q}_j, \hat{\mathbf{q}}_j)$ and $r_{\text{OPM}}(\mathbf{q}_j, \hat{\mathbf{q}}_j)$, respectively.

To examine the spatial performance of the beamformer, four dipoles were chosen at random in the frontal, parietal and occipital regions. MEG data were generated separately for each dipole and beamformer-reconstructed time courses were generated at the source location and its 44 nearest neighbours, corresponding to distances of between 0–3 cm from the simulated source. The magnitude of temporal correlation between the simulated source time course and the beamformer reconstructions was then plotted as a function of distance from the source.

"Brain noise"

Although highly illustrative, beamformer reconstruction of single dipoles, as described in Section 3.2.3 - **Single dipoles**, is not necessarily representative of real life situations in which the beamformer must reconstruct the source of interest whilst simultaneously removing sources of interference. In order to investigate this, multiple dipole simulations were employed. Here, a single source of interest, $\mathbf{q}_j$, was simulated on the cortical surface as previously. However, in addition, five further sources, denoted by $\mathbf{q}_{\text{Int}_k}$, where $k = 1, 2, \ldots, 5$, were also simulated as interference generators (brain noise). For both $\mathbf{q}_j$ and $\mathbf{q}_{\text{Int}_k}$, source time courses were simulated as Gaussian-distributed random data with a standard deviation of 5 nAm. The MEG data were then simulated as

$$\mathbf{m} = \mathbf{l}_j \mathbf{q}_j + \sum_{k=1}^{5} \mathbf{l}_{\text{Int}_k} \mathbf{q}_{\text{Int}_k} + \mathbf{e}, \tag{3.7}$$

where $\mathbf{l}_{\text{Int}_k}$ represents the forward field vector for interference source k. Two separate cases of interference generators were simulated:

- **Case 1 – Interference in close proximity:** All 5 interference sources were dipolar, located on the cortical mesh, oriented perpendicular to the cortical surface and defined between 0–3 cm (Euclidean distance) from the source of interest. Actual interference locations were random, but in all cases were set such that $\mathbf{q}_{\text{Int}_1}$ was located at a distance of 0–6 mm from j; $\mathbf{q}_{\text{Int}_2}$ was between 6–12 mm from j; $\mathbf{q}_{\text{Int}_3}$ was between 12–18 mm from j; $\mathbf{q}_{\text{Int}_4}$ was between 18–24 mm from j and finally $\mathbf{q}_{\text{Int}_5}$ was between 24–30 mm from j. The location j, of the source of interest was allowed to vary across 10,400 possible dipole locations within a single hemisphere on the cortical mesh. See Figure 3.2a.

- **Case 2 – Deep sources:** Here, all 5 interference sources were again dipolar, oriented perpendicular to the cortical surface and located on the cor-

tical mesh at distances less than 4 cm from the closest sOPM sensor. The source of interest, however, was limited to cortical locations between 4 cm and 6 cm from the closest sOPM sensor. This therefore simulated the situation where the source of interest was located deeper than the sources of interference. The location, j, of the source of interest was allowed to vary across 4,901 possible dipole locations (see Figure 3.2b).

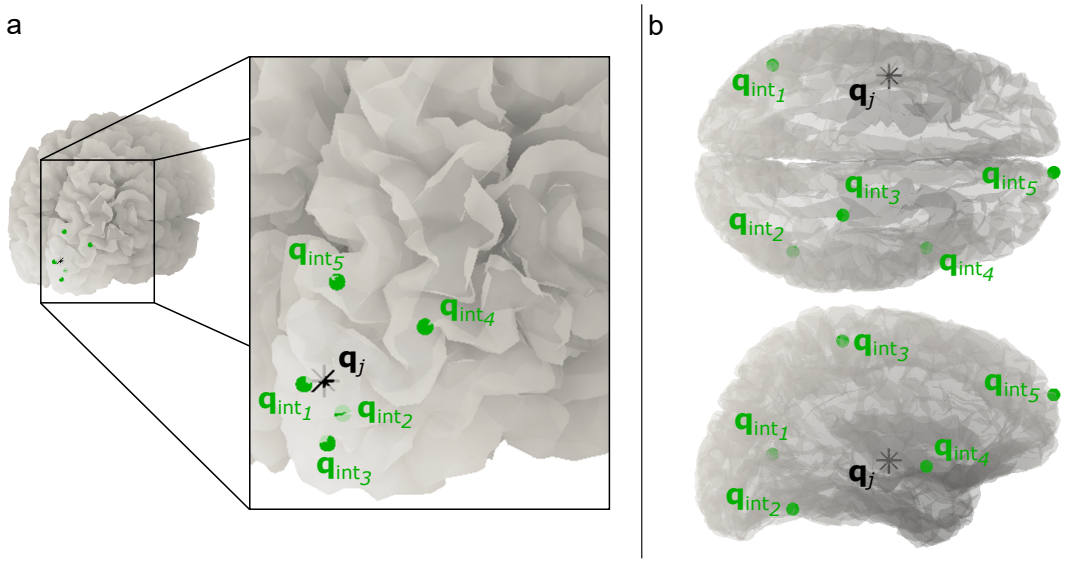


Figure 3.2: **Sources of interest and interference**. Schematic showing a single example of the relative locations of the source of interest (black) and the interference generators (green) for a) Case 1 (Interference in close proximity) and b) Case 2 (Deep sources).

In all cases, each MEG dataset was simulated as being 360,000 data samples (600 s) in length. In order to measure reconstruction accuracy we derived correlation coefficients $r_{\text{SQ}}(\mathbf{q}_j, \hat{\mathbf{q}}_j)$ and $r_{\text{OPM}}(\mathbf{q}_j, \hat{\mathbf{q}}_j)$ as previously. In order to quantify interference rejection, we also measured correlation between the beamformer-reconstructed estimate, $\hat{\mathbf{q}}_j$, and all five interference source time courses, $\mathbf{q}_{\text{Int}_k}$; i.e. we measured $r_{\text{SQ}}(\mathbf{q}_{\text{Int}_k}, \hat{\mathbf{q}}_j)$ and $r_{\text{OPM}}(\mathbf{q}_{\text{Int}_k}, \hat{\mathbf{q}}_j)$ for the sSQUID and sOPM systems, respectively. Obviously, for perfect beamformer performance we would expect $r(\mathbf{q}_j, \hat{\mathbf{q}}_j)$ to be close to one, whilst $r(\mathbf{q}_{\text{Int}_k}, \hat{\mathbf{q}}_j)$ should be close to zero.

Forward field error

The simulations described in Sections 3.2.3 - **Single dipoles** and **"Brain noise"** assume that the forward model used for beamforming is accurate (i.e. $\mathbf{l}_j$ in Equations 3.3 and 3.7 which defines the simulated data, and $\mathbf{l}_j$ in Equation 3.6 which describes beamforming, were the same). However, in reality, some error in deriving the forward model might be expected due to, for example, inaccurate knowledge of sensor locations or poor physical models of the fields generated. For this reason, it is important to define how forward field accuracy impacts upon beamformer source reconstruction for both sSQUID and sOPM instrumentation. In order to investigate this, we first altered the beamformer weights in Equation 3.6 such that:

$$\mathbf{w}_j^T = \frac{\hat{\mathbf{l}}_j^T \{\mathbf{C} + \mu\Sigma\}^{-1}}{\hat{\mathbf{l}}_j^T \{\mathbf{C} + \mu\Sigma\}^{-1} \hat{\mathbf{l}}_j}, \tag{3.8}$$

where

$$\hat{\mathbf{l}}_j = \mathbf{l}_j + \Delta\mathbf{l}_j \tag{3.9}$$

represents the forward field with added error $\Delta\mathbf{l}_j$. In order to simulate error on the forward model, we employed a geometrical approach depicted in Figure 3.3a. We first treated the genuine forward field, $\mathbf{l}_j$, as a $N_{ch} \times 1$ element vector, and defined a hyperplane in N_{ch}-dimensional space that is perpendicular to $\mathbf{l}_j$. In order to perturb $\mathbf{l}_j$, we defined the error $\Delta\mathbf{l}_j$ as a $N_{ch} \times 1$ element vector that is confined to the hyperplane. The vector sum of $\mathbf{l}_j$ and $\Delta\mathbf{l}_j$ then gave us the modified forward field as in Equation 3.9. The value $||\Delta\mathbf{l}_j||/||\mathbf{l}_j||$ represents a quantitative measure of the fractional error imposed upon the forward field model. (Note also that the angle α between $\hat{\mathbf{l}}_j$ and $\mathbf{l}_j$ (see Figure 3.3a) relates to the similarity between the accurate and perturbed forward field patterns).

$\Delta\mathbf{l}_j$ was constructed by first defining a $N_{ch} \times 1$ vector of random numbers, $\mathbf{r}$, as shown (for the simple 2D case) in Figure 3.3b. Projecting this random vector

onto the hyperplane gives:

$$\Delta \mathbf{l}_j = \xi \left\{ \mathbf{r} - \left(\frac{\mathbf{l}_j}{||\mathbf{l}_j||} ||\mathbf{r}|| \cos\beta \right) \right\}, \tag{3.10}$$

where

$$\cos\beta = \frac{\mathbf{l}_j^T \mathbf{r}}{||\mathbf{l}_j||\ ||\mathbf{r}||}. \tag{3.11}$$

And so

$$\Delta \mathbf{l}_j = \xi \left\{ \mathbf{r} - \left(\mathbf{l}_j \left(\mathbf{l}_j^T \mathbf{l}_j \right)^{-1} \mathbf{l}_j^T \mathbf{r} \right) \right\}. \tag{3.12}$$

The magnitude of $\Delta \mathbf{l}_j$ is controlled by the parameter ξ which can be used to manipulate the amount by which the forward field is modified.

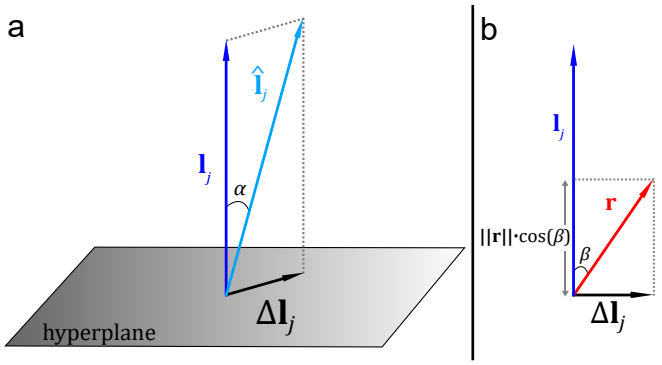


Figure 3.3: **Schematic diagram of forward field error simulation**. The perfect forward field, $\mathbf{l}_j$ is perturbed via addition of $\Delta \mathbf{l}_j$ to give $\hat{\mathbf{l}}_j$.

The single-source simulations, described in Section 3.2.3 - **Single dipoles**, were repeated, but this time, sources were reconstructed using beamforming (Equation 3.8) with added error on the forward field vector. The elements of $\mathbf{r}$ were defined as Gaussian-distributed random numbers and ξ was varied through 20 iterations such that $||\Delta \mathbf{l}_j||/||\mathbf{l}_j||$ spanned approximately the range from 0 to 0.5. For each value of ξ the simulation was repeated 5 times (with 5 realisations of $\mathbf{r}$) and results averaged. This whole process was repeated for 100 dipole locations randomly selected from one cortical hemisphere (performing this calculation for all dipole locations proved too computationally intensive). Results were averaged across shallow and deep dipoles.

3.2.4 Spatial resolution and channel count

To examine the spatial resolution of source-reconstructed MEG data from the sSQUID and sOPM systems, a final set of simulations was employed. Two sources were simulated at separate locations on the cortical surface, k and n. Two source time courses, $\mathbf{q}_k$ and $\mathbf{q}_n$ were simulated, both contained a total of N time points and comprised different Gaussian-distributed random data with a standard deviation of 5 nAm, meaning that the sources were temporally orthogonal. MEG data were then generated as

$$\mathbf{m} = \mathbf{l}_k\mathbf{q}_k + \mathbf{l}_n\mathbf{q}_n + \mathbf{e}, \tag{3.13}$$

where $\mathbf{l}_k$ and $\mathbf{l}_n$ are the forward field vectors for cortical locations k and n respectively, and $\mathbf{e}$ represents noise (normally-distributed random data with a standard deviation of 35 fT). This simulation was run multiple times with the source locations (k and n) selected randomly. The Euclidean distance between sources was measured for each source pair.

As previously, data were reconstructed using the beamformer spatial filter such that $\hat{\mathbf{q}}_k = \mathbf{w}_k^T\mathbf{m}$ and $\hat{\mathbf{q}}_n = \mathbf{w}_n^T\mathbf{m}$. In a connectivity measurement in real MEG data, we would look to quantify a relationship between the two reconstructed dipole time courses, $\hat{\mathbf{q}}_k$ and $\hat{\mathbf{q}}_n$; any statistical interdependency between these quantities would be used to indicate a functional connection between brain regions k and n (see O'Neill et al. (2015a) for a review). However, such a measurement necessarily requires that there is no spurious correlation between $\hat{\mathbf{q}}_k$ and $\hat{\mathbf{q}}_n$ caused by the limited spatial resolution. In the present simulation, the underlying time courses $\mathbf{q}_k$ and $\mathbf{q}_n$ used to generate the data are orthogonal, so that the correlation coefficient $r(\mathbf{q}_k, \mathbf{q}_n) = 0$. In order to test for the effects of spurious correlations in the beamformer reconstruction, we therefore measured correlation between source reconstructions, $r(\hat{\mathbf{q}}_k, \hat{\mathbf{q}}_n)$: if the dipoles simulated at k and n are resolvable, then this quantity should be close to zero. Note that in

much of the functional connectivity literature, $r(\hat{\mathbf{q}}_k, \hat{\mathbf{q}}_n)$ would be referred to as leakage between sources (Brookes et al., 2012). This simulation was run 3,000 times with $N = 360{,}000$. The measured Euclidean distances were categorised into 30 different bins of 2-mm width, the smallest being 0–2 mm, the largest being 58–60 mm. The simulation was designed such that 100 repeats were run for each bin. The spatial resolutions of the sSQUID and sOPM systems were then measured via assessment of the quantity $r(\hat{\mathbf{q}}_k, \hat{\mathbf{q}}_n)$ plotted against distance. Two sources were considered resolved if $r(\hat{\mathbf{q}}_k, \hat{\mathbf{q}}_n) < 1/\sqrt{2}$ (i.e. less than 50% shared variance between sources).

We also investigated the effect of different channel counts on the sOPM system's spatial resolution. In order to do this, three additional sensor configurations were simulated according to: 1) the international 10-10 EEG system; 2) the 10-5 EEG system (Oostenveld and Praamstra, 2001) and 3) a theoretical 10-2.5 system (see Figure 3.4). The application of these sensor configurations onto the scalp surface (Giacometti et al., 2014) resulted in systems with 81, 329 and 1,293 sensors respectively. A separate measurement of $r(\hat{\mathbf{q}}_k, \hat{\mathbf{q}}_n)$ versus source separation was made for each of these three systems.

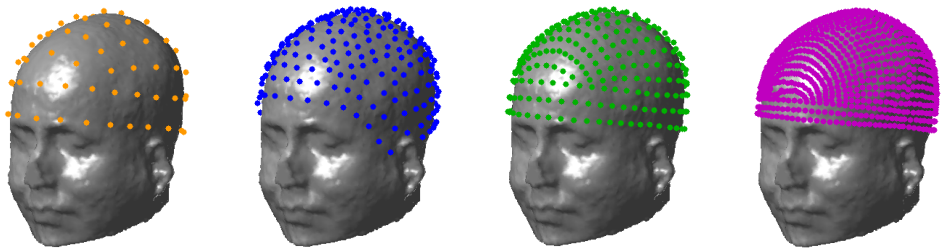


Figure 3.4: **Simulated systems for channel count comparison**. Simulation set-up comparing four different sOPM systems (from left to right): 81 sensors (10-10 EEG system), 275 sensors (equivalent to that shown in Figure 3.1a), 329 sensors (10-5 system) and 1293 sensors (hypothetical 10-2.5 system).

Finally, a simulation was employed to quantify the spatial resolution of both systems as a function of cortical location. Simulated MEG data were generated for pairs of dipoles as before (Equation 3.13), with the only difference that k ran for all dipole locations within one cortical hemisphere and n corresponded initially to k's nearest neighbour on the cortical mesh. In cases where $r(\hat{\mathbf{q}}_k, \hat{\mathbf{q}}_n)$ was

larger than $1/\sqrt{2}$, the simulation was repeated for k's next nearest neighbour, and so on, until the value of $r(\hat{\mathbf{q}}_k, \hat{\mathbf{q}}_n)$ fell below $1/\sqrt{2}$. Here, spatial resolution was assessed as the minimum distance between the dipole seed (k) and its neighbour (n) for which both sources can be considered separable. Both this spatial resolution value and the correlation between reconstructed time courses were assessed.

3.3 Results

Figure 3.5a shows an example of simulated magnetic fields (i.e. the forward field) for a single dipole located in the parietal lobe. Note that, for this particular dipole, the magnitude of the maximum measured magnetic fields is approximately a tenfold higher for the sOPM system than for the sSQUID set-up. As would be expected, the topographic pattern of the magnetic field is also more focal in the sOPM compared to the sSQUID system. Figure 3.5b shows the ratio of the Frobenius norms of the forward field vectors for the two systems, plotted as a function of dipole location on the cortex. The colours represent the ratio $(f_{j,\text{OPM}}/f_{j,\text{SQ}})$ such that a ratio of 5 would indicate a fivefold improvement in SNR of the sOPM compared to the sSQUID system. The figure shows clearly that the sOPM system offers an improvement in SNR for all dipole locations on the cortex; this improvement is approximately a factor of five (yellow) across most of the cortex, increasing to close to ten (red) for some areas of the frontal lobe. The improvement is less dramatic in deeper cortical areas (a consequence of the inverse square law), but the sOPM system still offers twice the SNR of the sSQUID system (blue). Note that the spatial variation of this improvement in SNR depends on the position of the subject's head in the CTF MEG helmet. As stated above, in the simulations the subject was positioned with the back of their head touching the back of the CTF helmet, thus the largest improvements in SNR are observed in the frontal lobes. Note also that these measurements

were based on an adult male, with a head size of 21.3 cm anterior to posterior and 14.6 cm left to right, meaning that this individual's head was well fitted to the size of the CTF helmet: in a subject with a small head, the improvements provided by the sOPM system would be more pronounced.

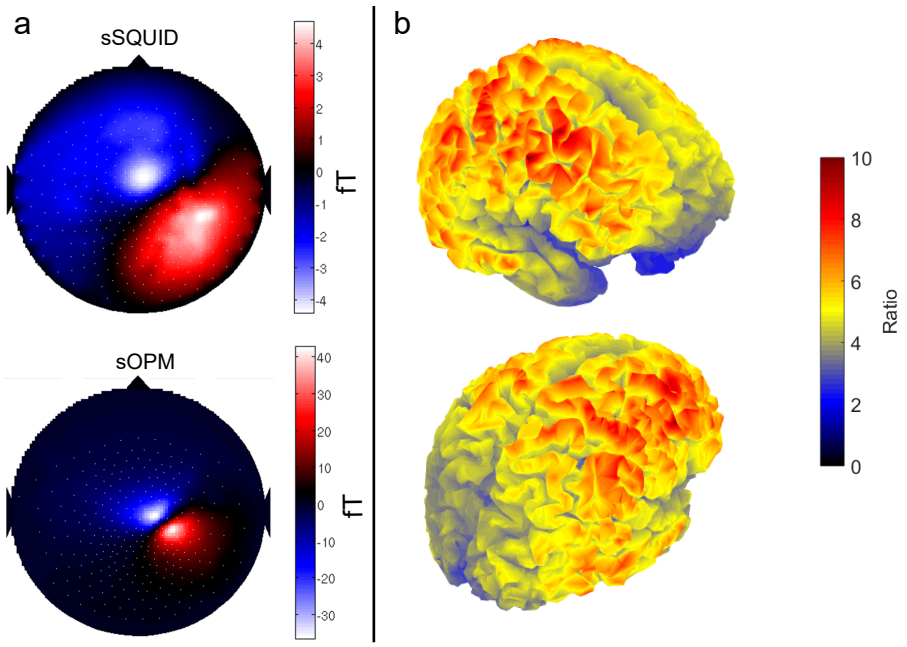


Figure 3.5: **SNR simulation results**. a) Simulated magnetic field from a single dipole located in the parietal lobe. b) The ratio of the Frobenius norms of the forward fields, plotted as a function of dipole location on the cortex. The colours represent the quantity $f_{j,\mathrm{OPM}}/f_{j,\mathrm{SQ}}$. The top and bottom panels show different aspects of the same data.

Figure 3.6a shows beamformer reconstruction accuracy in the single-dipole simulations (see Section 3.2.3 - **Single dipoles**). The left panel shows the sSQUID system and right panel shows the sOPM system. In both cases the colour bar indicates temporal correlation between the simulated and reconstructed dipole time courses; i.e. the left and right plots show $r_{\mathrm{SQ}}(\mathbf{q}_j, \hat{\mathbf{q}}_j)$ and $r_{\mathrm{OPM}}(\mathbf{q}_j, \hat{\mathbf{q}}_j)$ respectively, plotted against dipole location j on the cortical surface. A value of 1 would indicate perfect reconstruction. Here, the sSQUID system exhibits reasonably good performance with correlation greater than 0.8 across the vast majority of the cortex. However reconstruction accuracy is highest for the occipital lobe and drops in the frontal lobes – most likely due to the position of the subject's head in the MEG helmet. Reconstruction accuracy is lowest in the temporal lobes and this is likely due to lower sensor coverage for these

brain regions. In contrast, for the sOPM system we see excellent reconstruction accuracy across the entire cortex, with correlation greater than 0.9 everywhere on the cortical surface. Note particularly the improvements in reconstruction accuracy in the temporal lobe compared with the sSQUID system. Figure 3.6b shows spatial reconstruction accuracy for four different locations (shown overlaid in black on the central figure). Correlation coefficients between the original and reconstructed time courses for the simulated dipole location and 44 of its nearest neighbours, are plotted against the relative distance to the simulated dipole location. Results show that both systems generate an accurate spatial reconstruction of the source with maximum correlation at zero distance. However, temporal correlation falls off faster with distance for the sOPM system indicating a sharper (more focal) reconstruction.

Figure 3.7, shows beamformer reconstruction accuracy with "brain noise" (see Section 3.2.3 - **"Brain noise"**). Panel (a) shows results for Case 1 (Interference in close proximity) whilst panel (b) shows results for Case 2 (Deep sources). In both cases, the left-hand panel shows average temporal correlation between the simulated and the beamformer-reconstructed source of interest at j (i.e. graphs show the quantity $r(\mathbf{q}_j, \hat{\mathbf{q}}_j)$). For comparison, the case with and without the interference sources are both shown. Right-hand plots represent average correlation between each of the 5 simulated interference sources and the beamformer estimate of the source of interest at j (i.e. the quantity $r(\mathbf{q}_{\text{Int}_k}, \hat{\mathbf{q}}_j)$). In Figure 3.7a (left), it is clear that switching on the interference degrades the quality of the source estimate for both systems, as would be expected; however this degradation is more pronounced for the sSQUID system compared to the sOPM system. Regarding Figure 3.7a (right), first recall that interference sources were located progressively further away (in terms of Euclidean distance) from the source of interest with increasing index, k; this explains the decreasing temporal correlation with increasing k. Importantly, the beamformer's ability to reject interference (even in very close proximity) is improved markedly for the

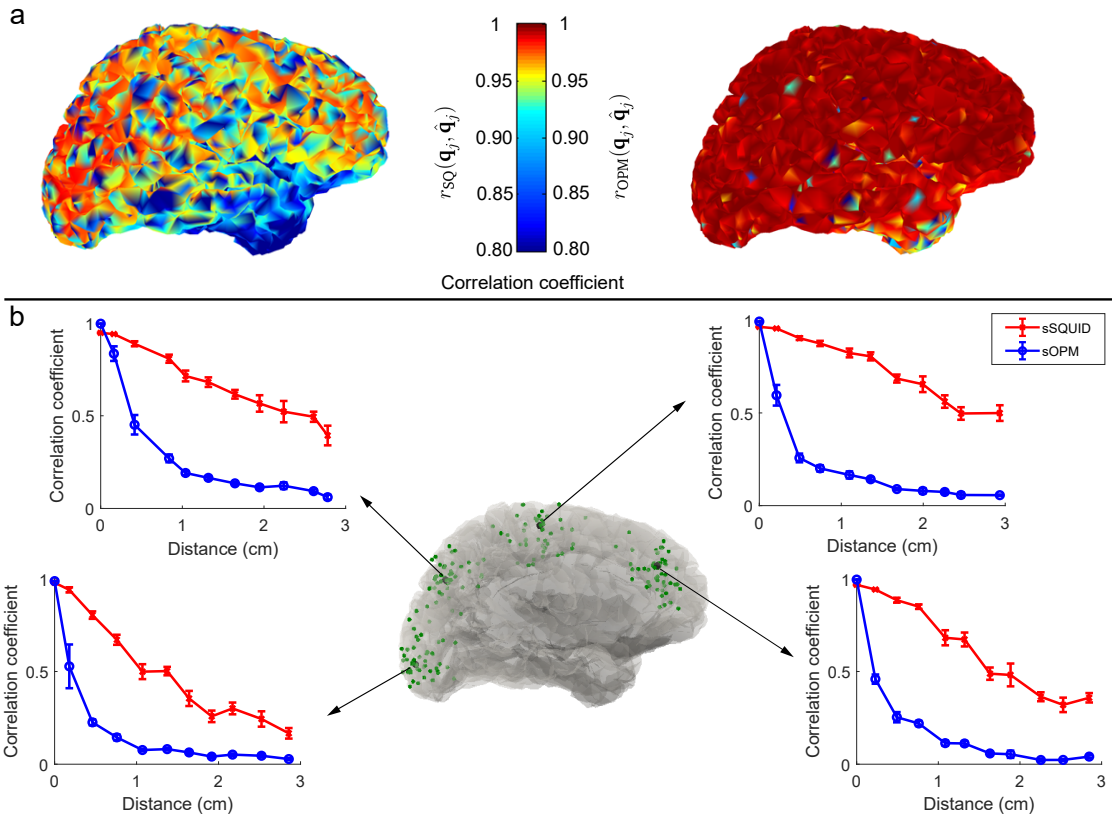


Figure 3.6: **Reconstruction accuracy**. a) The left (right) hand panel shows beamformer reconstruction accuracy for the sSQUID (sOPM) system. Colours represent the quantities $r_{SQ}(\mathbf{q}_j, \hat{\mathbf{q}}_j)$ and $r_{OPM}(\mathbf{q}_j, \hat{\mathbf{q}}_j)$ for left and right panels, respectively. b) Spatial reconstruction accuracy around four cortical locations (in black). The four inset graphs show correlation coefficients between the original simulated time course and reconstructed dipole time courses at the simulated source location and its nearest neighbours (shown in green on the central image). Correlation is plotted as a function of Euclidean distance to the simulated dipole.

sOPM system compared to the sSQUID system. Note that the temporal correlation between the beamformer-estimated source of interest and all interfering sources is lower for sOPM than for sSQUID; this is the case for interference in close proximity, and for deep sources.

Figure 3.8 shows how reconstruction accuracy is affected by errors in the forward field model (see Section 3.2.3 - **Forward field error**). In order to visualise results, dipole locations on the cortical surface were divided according to depth: those whose distance to the closest sOPM sensor, d_j, was less than 4 cm (shallow sources – shown in black in panel (a)) and those whose distance, d_j, to the closest sOPM sensor was between 4 cm and 6 cm (deep sources – shown in grey). To show the influence of forward field accuracy on beamforming, corre-

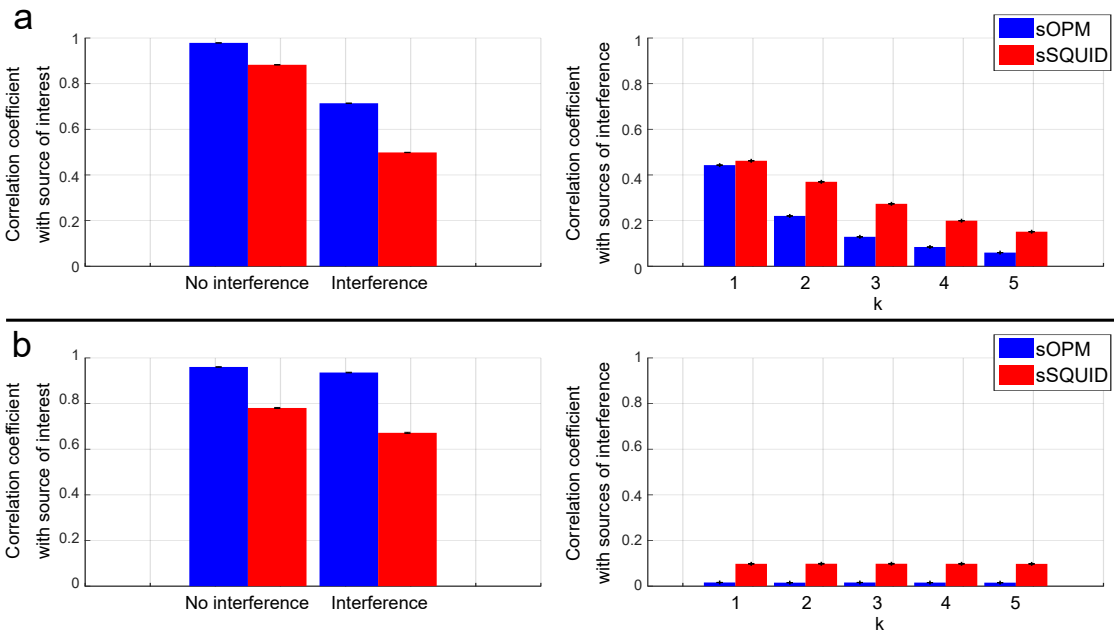


Figure 3.7: **Reconstruction accuracy with "brain noise"**. a) Case 1 (Interference in close proximity). b) Case 2 (Deep sources). In both panels, the left hand graph shows the average of correlation coefficients between simulated and reconstructed dipole time courses, $r(\mathbf{q}_j, \hat{\mathbf{q}}_j)$, with and without interference. The right-hand graph shows the average of correlation coefficients between each of the interference sources and the reconstructed main dipole time course, $r(\mathbf{q}_{\text{Int}_k}, \hat{\mathbf{q}}_j)$. sOPM is represented in blue and sSQUID in red.

lation coefficients between simulated and reconstructed time courses, $r(\mathbf{q}_j, \hat{\mathbf{q}}_j)$, were measured and plotted as a function of fractional error on the forward field $||\Delta\mathbf{l}_j||/||\mathbf{l}_j||$ (Figure 3.8b). The left graph shows results for deep sources whilst the right graph shows results for shallow sources. In both cases note that, with no forward field error, sOPM outperforms sSQUID. This is in agreement with the results given in Figures 3.6 and 3.7. However, as forward field error is increased, the reconstruction accuracy of both systems falls, with the sOPM system being more sensitive. This means that for dipoles close to the scalp surface (shallow dipoles) even an error of less than 5% in the forward field can negate the significant advantages afforded by the sOPM system. For deeper dipoles, this is less dramatic but a 25% error on the forward field would again mean that sSQUID and sOPM systems perform approximately equally well, with errors greater than this meaning the sSQUID system more accurately reconstructs dipole time courses. These results highlight a critical point: although the intro-

duction of an OPM system has the potential to generate a step change in the utility of MEG, the realisation of this potential depends not only on our ability to engineer such a system, but also critically on our ability to model accurately the forward field. This key point will be addressed further in the discussion below.

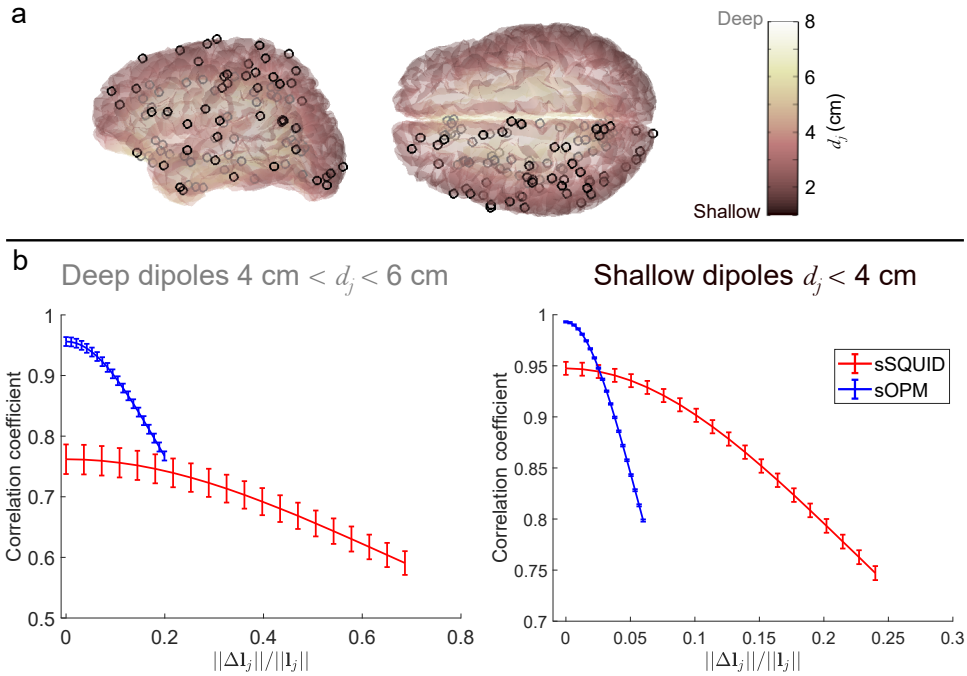


Figure 3.8: **Dependency of reconstruction accuracy on forward field error**. a) Dipole locations with deep sources shown in grey and shallower sources shown in black. b) Temporal correlation between the simulated and beamformer-reconstructed sources (i.e. $r(\mathbf{q}_j, \hat{\mathbf{q}}_j)$) plotted as a function of fractional error on forward field ($||\Delta \mathbf{l}_j||/||\mathbf{l}_j||$). The two separate plots show the case for deep (left) and shallow (right) dipoles. The sOPM system is shown in blue and the sSQUID system in red.

Figures 3.9 and 3.10 show the results of the spatial resolution measurements. Figure 3.9a shows how the correlation, between two reconstructed sources, $r(\hat{\mathbf{q}}_k, \hat{\mathbf{q}}_n)$ (also termed source leakage in connectivity literature – see Section 3.2.4 - **Spatial resolution and channel count**) varies with source separation for the sOPM (blue curve) and sSQUID systems (red curve). The simulated source time courses were orthogonal, so any non-zero value of $r(\hat{\mathbf{q}}_k, \hat{\mathbf{q}}_n)$ is purely an artefact of the limited spatial resolution of the beamformer. Two sources are deemed separable if $r(\hat{\mathbf{q}}_k, \hat{\mathbf{q}}_n) < 1/\sqrt{2}$. Note that no forward field error was simulated for results in Figure 3.9. It is clear that the 275-channel sOPM system offers much improved spatial resolution compared to the sSQUID system. Sources

become separable for the sSQUID system when the Euclidean separation is approximately 5 mm. Indeed this value is in approximate agreement with findings from real data (Barratt et al., 2018). However for the sOPM system, sources are separable at smaller separations, with temporal correlation never reaching more than 0.4 (16% shared variance). This finding shows clearly the significant advantages of an OPM system, particularly in the study of functional connectivity; this will be addressed further in the discussion below. In the inset figure, the correlation coefficients between simulated and reconstructed time courses for each dipole source ($r(\mathbf{q}_k, \hat{\mathbf{q}}_k)$ and $r(\mathbf{q}_n, \hat{\mathbf{q}}_n)$) are also plotted for both systems, as a function of distance between sources. This reflects the reconstruction accuracy for each dipole, showing that each dipole time course is better reconstructed as distance between them is increased. Note again improved performance of the sOPM system. The four simulated systems in Figure 3.4 were used to assess the advantages of increased channel counts for spatial resolution. Figure 3.9b shows results of this measurement: again $r(\hat{\mathbf{q}}_k, \hat{\mathbf{q}}_n)$ is plotted as a function of distance between sources for the 81-channel (orange), 275-channel (blue), 329-channel (green) and 1293-channel (purple) OPM systems. The sSQUID system is plotted for comparison. A marked improvement in spatial resolution is observed as channel count is increased.

Finally, Figure 3.10 shows spatial resolution plotted as a function of location on the cortical surface. Figure 3.10a shows the minimum spatial separation for which two dipoles become resolvable (i.e. the temporal correlation between time courses falls below $1/\sqrt{2}$). This in itself does not constitute a measure of spatial resolution because the discrete nature of the cortical mesh means that a dipole separation corresponding to a temporal correlation of precisely $1/\sqrt{2}$ is not possible. For this reason, the spatial separations in Figure 3.10a must be given alongside a corresponding value of temporal correlation at the derived minimum separation. These values are given in Figure 3.10b. Note that not only is the minimum spatial separation between dipoles reduced from an aver-

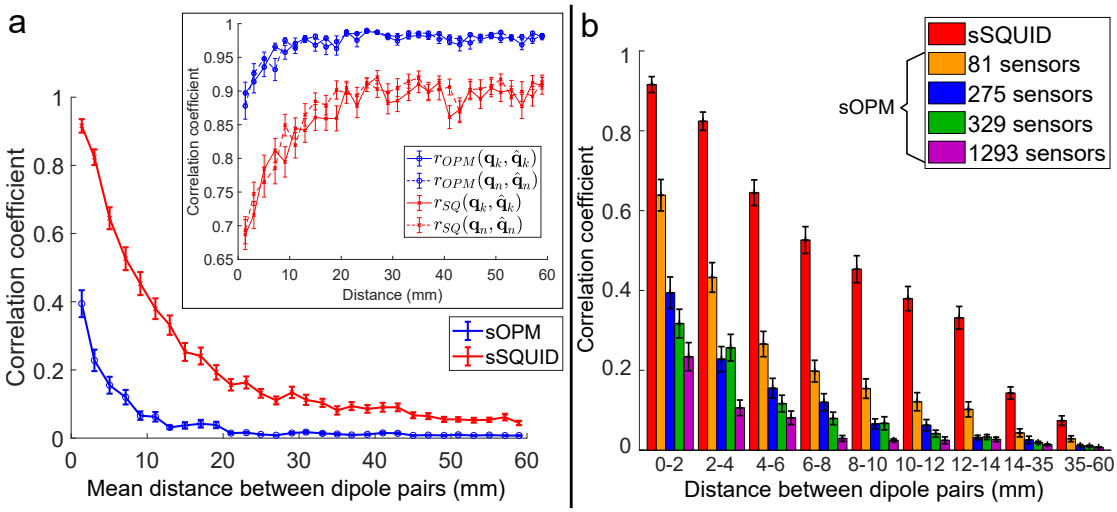


Figure 3.9: **Spatial resolution and channel count measurements**. a) Correlation coefficient between two simulated dipole sources after beamforming reconstruction, $r(\hat{\mathbf{q}}_k, \hat{\mathbf{q}}_n)$ plotted against Euclidean distance between the sources. The red and blue traces show the results for the sSQUID system and sOPM systems, respectively. The inset shows correlation coefficients between simulated and reconstructed time courses for the two sources separately, i.e. $r(\mathbf{q}_k, \hat{\mathbf{q}}_k)$ and $r(\mathbf{q}_n, \hat{\mathbf{q}}_n)$. b) Comparison of spatial resolution for the 81, 275, 329 and 1,293 sensor sOPM systems shown in Figure 3.4. Again, the graphs show correlation between reconstructed time courses plotted as a function of Euclidean distance between sources.

age of 6.3 mm in the sSQUID system to 2.5 mm in the sOPM system, but also the temporal correlation at those minimum separations is reduced from 0.49 in the sSQUID to 0.29 in the sOPM. This important result is in agreement with that shown in Figure 3.9 and further supports the finding that the sOPM system demonstrates dramatically better spatial resolution compared to the sSQUID system.

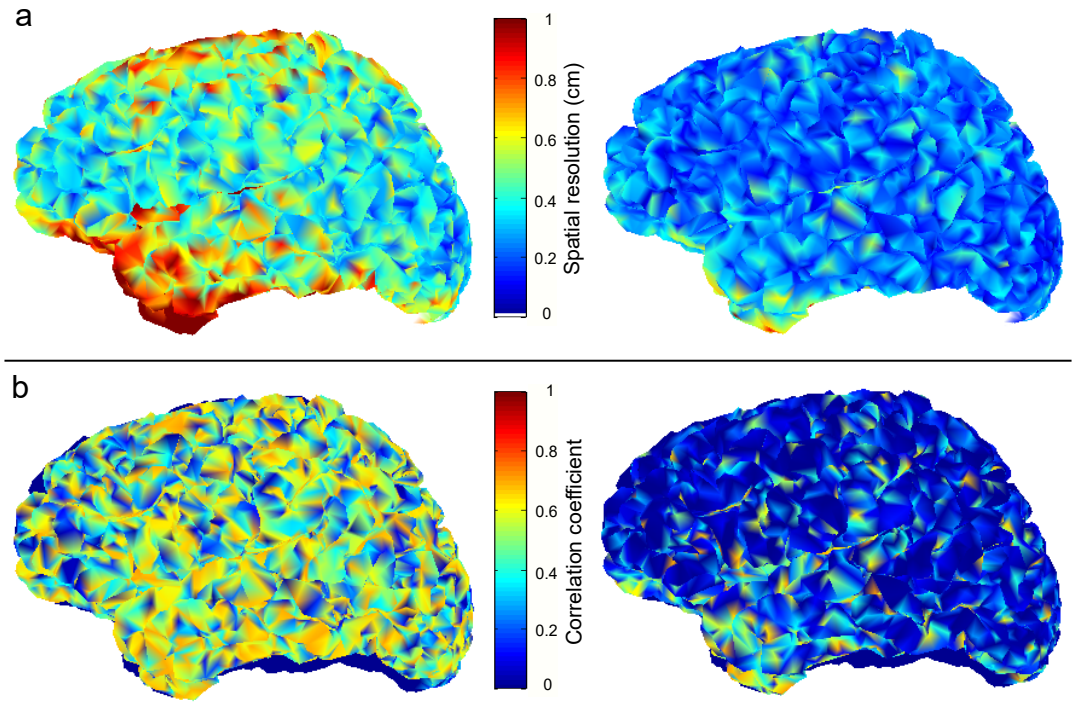


Figure 3.10: **Spatial resolution (275 channels)**. Left (right) hand panels show results for the sSQUID (sOPM) system. a) Minimum distance between the dipole seed and its neighbours for which two sources are separable, plotted as a function of seed dipole location. b) Their corresponding temporal correlation values.

3.4 Discussion

In this chapter, we have used simulations to quantify the potential advantages of an on-scalp OPM-based MEG system in terms of SNR, beamformer reconstruction accuracy and spatial resolution. Our results show that an OPM system, with an equivalent number of channels and equal noise floor to current SQUID systems, would offer approximately a fivefold increase in SNR across most of the cortex, and up to an order of magnitude improvement in SNR in some regions, for an adult brain. This improvement, which results from the closer proximity of the sensors to the cortex, would be even more dramatic for subjects with smaller heads (e.g. infants). These results also show a clear improvement in the accuracy of beamformer source reconstruction; average correlation between simulated and beamformer-reconstructed sources increased significantly for the

simulated OPM system and this was the case with and without interference from other brain sources. However, these simulations also show that such improvement depends critically on the accurate generation of forward models. Finally, our results show a marked improvement in spatial resolution of the simulated OPM system, which becomes more dramatic when increasing the channel count. Overall, results of this simulation work imply that the realisation of a multi-channel whole-head OPM system could generate a step change in the utility of MEG.

Since this simulation study was undertaken, Iivanainen and colleagues (Iivanainen et al., 2017) carried out a similar simulation work comparing a hypothetical whole-head OPM system to a current state-of-the-art SQUID-based Elekta Neuromag system. The simulated OPM system comprised 306 magnetometers (102 measured the normal component of the field and 204 measured the two orthogonal tangential components). They used BEM forward models and minimum-norm inverse methods. Their results, in agreement with those presented here, showed a marked improvement of the OPM system over the SQUID system in terms of signal power, information capacity and spatial resolution.

3.4.1 SNR

The SNR improvement afforded by OPM systems could revolutionise both the type of neuromagnetic effects that can be measured by MEG, and the brain regions to which MEG is sensitive. At present, MEG measurements are limited: in most task-based studies, responses must be averaged over trials to increase SNR; OPMs could offer a route to measuring single-trial responses and hence provide a new perspective on, for example, motor learning. In addition, the sensitivity of MEG measurements falls with frequency since neural networks oscillating at high frequencies tend to be small. However, invasive recordings show that

neuroelectrical effects up to and including frequencies of 200 Hz are measurable (Crone et al., 2006). OPM systems, if they could be implemented with a sufficiently high bandwidth, could offer a route to assess, non-invasively, networks of neurons oscillating at these high frequencies. The improvement in SNR also offers a better coverage of deep brain areas. This would enhance coverage for deep cortical regions such as cingulate and insula, and also sub-cortical grey matter nuclei including basal ganglia and hippocampi; signals from both of these regions have been measured successfully using conventional SQUID-based MEG systems (Timmermann et al., 2003; Luckhoo et al., 2012), however efforts to characterise their behaviour have been hampered by low SNR. Our simulations show that signals acquired from all deep structures using an OPM system would be enhanced in terms of SNR. However, the degree of improvement is a function of depth. Specifically, the non-linear nature of the inverse square law means that, although moving detectors closer to the scalp surface offers increased SNR for all regions, the improvement for shallow sources is proportionally larger than for deep sources. Indeed, Figure 3.5 shows that whilst improvements for shallow sources could be as high as tenfold, for deeper sources the gain may be closer to twofold. This observation has important consequences. Even in current systems the effective characterisation of deep sources relies on our ability to eliminate interfering signals for shallow sources. When using OPMs, the greater amplification of shallow compared to deep sources potentially makes this problem harder, since the ratio of deep source (of interest) to shallow source (of no interest) signals is markedly reduced. This observation provides more evidence that realising the benefits of an OPM system depends critically on accurate source modelling.

3.4.2 Reconstruction accuracy

Our simulations also showed that, as a result of improved SNR (Figure 3.5b) and the more focal nature of the forward field (Figure 3.5a), beamformer reconstruction accuracy was improved significantly when using OPMs compared to a SQUID-based system. Specifically, temporal correlation between simulated and beamformer-reconstructed cortical sources increased significantly ($p<0.05$) from 0.87 for a current SQUID-based system, to 0.98 for a 275-channel OPM system (single-dipole model). Improvements were also observed in the presence of interference fields from nearby cortical dipoles of no interest and the results in Figure 3.7 show that the beamformer algorithm, applied to the sOPM system, was better able to cancel out such interference compared to the sSQUID system.

Although beamformer performance is enhanced in an OPM system, our results in Figure 3.8 show clearly that such improvements would rely heavily on accurate forward modelling. In the case of shallow cortical dipoles, simulations showed that a forward field error of as little as 4–10% would negate the significant advantages afforded by OPM instrumentation. This effect was also seen for deeper dipoles although it is somewhat less pronounced, with OPMs still outperforming SQUIDs up to approximately a 25% error on the forward field. These findings have been supported by recent work by Zetter and colleagues (Zetter et al., 2018), who found that to obtain similar or higher accuracy than with SQUID-based systems, RMS sensor position and orientation errors of an OPM system should be less than 4 mm and 10°, respectively.

Whilst perhaps counter-intuitive, this observation is well known: in short, as SNR increases, inverse modelling becomes increasingly sensitive to the accuracy of the forward model. In the case of OPMs, the increase in SNR afforded by the shift in sensor locations towards the scalp surface drives this necessity for increased forward model accuracy. In the simulations presented, we used a simple mathematical method in order to artificially generate an error on the forward so-

lution. This simulated error is an abstract mathematical formulation, but nevertheless illustrates the problem. Experimentally, these forward field errors come from 1) inaccurate co-registration between the head location and the sensor geometry, 2) subject movement (the forward field is derived based on average head position) and 3) inaccuracy in the forward model itself (e.g. deviation from the dipole model). In recent years, significant improvements in the latter have been introduced via, for example, the use of boundary element methods (BEM) based upon high resolution MR images. However, the co-registration problem is still heavily reliant on techniques such as surface digitisation and matching; which often leads to significant systematic errors in estimating MEG sensor locations relative to the brain anatomy. In fact, previous work suggests that the largest source of forward modelling error in MEG comes from co-registration (Hillebrand and Barnes, 2003). Also, for OPMs, as a consequence of subject movement we might expect independent errors if the sensors are not mounted rigidly with respect to one another. In addition, the OPM's cell (sensitive volume to magnetic field) will have a smaller area than that of the SQUID coils, and may also have a variable gain (in terms of magnitude and directional sensitivity) which will depend not only on fabrication but also on the proximity (and crosstalk) of other sensors. These errors could also impact significantly on forward field accuracy. Here we demonstrate that an abstract modelling error causes a significant problem that could easily negate any advantages afforded by an OPM system, particularly in modelling shallow cortical dipoles. Practical implementation of a system must therefore take these problems into account.

3.4.3 Spatial resolution

Assuming that solutions to the forward modelling problem can be found, the spatial resolution measurements in Figures 3.9 and 3.10 show the clear advantages of an OPM system in separating dipoles in close proximity in the brain.

This is important for all studies, but would be particularly beneficial in the study of functional connectivity between brain regions. The study of connectivity (functional and effective) has caused a paradigm shift in the way in which neuroimaging experiments are conducted and, particularly given the recent advances in dynamic connectivity (temporal changes in connectivity between regions over time) MEG now offers the most attractive means to characterise the way in which the brain forms and dissolves a hierarchy of electrophysiological networks of communication, in order to support current processing demand (Baker et al., 2014; O'Neill et al., 2015b). Although new MEG methodologies allow for unique insights into such network formation, at present, functional connectivity can only be measured reliably via the use of techniques for post-hoc correction of source leakage between brain regions. This source leakage is a direct result of the limited spatial resolution of the MEG beamformer, and multiple techniques including the use of the imaginary part of the coherence (Nolte et al., 2004), the phase-lag index (Stam et al., 2007) or linear regression (Brookes et al., 2012; Hipp et al., 2012) must be employed. Whilst these techniques work, they all eliminate genuine zero-phase lag correlation between electrical signals from separate regions. Invasive measures show clearly that such zero-phase lag effects exist in the brain (Singer, 1999; Engel et al., 2001) and are currently missed by MEG. Our results imply that post-hoc correction methods would not be required for OPM systems, for the typical networks observed. This would prove of key importance in future characterisation of brain network behaviour and dynamics.

3.4.4 Limitations

It is important to point out the limitations of the simulations that have been undertaken. First, these simulations are simple: they are based on small numbers of dipoles. Second, the noise is assumed to be Gaussian-random and therefore

uncorrelated across MEG channels. Although these assumptions are unrealistic compared to experimental measurements, it is worth noting that our source reconstruction results are approximately in agreement with what is observed in real data from current SQUID-based systems (Barratt et al., 2018). Furthermore, simple simulations of this type have been used extensively in a wide variety of published research (Vrba, 2002; Barnes and Hillebrand, 2003) and these papers provided inspiration to the field of MEG source reconstruction for more than a decade. The quantitative observations made are therefore likely to be representative, and provide a benchmark to which any real system might aspire. Third, there are also many aspects of OPM system design which we have not touched upon. Most importantly, OPM sensors offer a means to measure the magnetic field in two orthogonal orientations perpendicular to the laser beam. This means that in addition to measuring magnetic field in the radial direction (the approach taken by all conventional systems), one additional tangential direction may also be measured using the same sensor. Practically, this requires extra instrumentation (an extra field modulation coil on each sensor is required, as well as an increased number of readout channels). From a modelling point of view, the tangential component of magnetic field is mainly affected by volume currents and so its measurement would necessitate the use of more complex finite element forward models (Iivanainen et al., 2017). From a system design point of view, it is not immediately obvious how one might orient the additional axis (i.e. at each measurement location, which tangential field component should be measured?). This latter point in particular is the reason that here we limited ourselves to assessing the radial field only. In fact, design of a system which measures vector field components would necessitate significant simulations to identify an optimal sensor arrangement. However, future simulation work should begin to assess this potentially significant advantage of OPMs compared to SQUIDs. There are other significant design problems with OPMs, for example, they operate around a zero-field resonance meaning that compen-

sation coils are often mounted on the OPM itself to cancel the remnant field inside the shield. In addition, the operation of a multi-channel array may be complicated by crosstalk between sensors from both the internal field-zeroing coils and from field modulation used for lock-in detection. Interfering fields between sensors in close proximity would significantly alter both the sensor gain and potentially the orientation of the sensitive axis of detection. This simulation work does not claim to solve these practical issues relating to the practical use of OPMs, rather the intention was to present a vision of the potential advantages of an OPM system as well as to elucidate the potential modelling problems that the realisation of such a system might generate. Finally, note that, in principle, the theoretical systems described here could result from any technology in which the external surface of the magnetic field sensor is such that the sensor can be scalp-mounted.

3.5 Conclusions

In this chapter we have quantified via simulation the advantages of an OPM system in terms of SNR, beamformer reconstruction accuracy and spatial resolution. Results show that such an OPM system could offer around a fivefold improvement in SNR for an adult brain. Further, our results show clear improvement in reconstruction accuracy and a marked improvement in spatial resolution. These results imply that the realisation of a multi-channel whole-head OPM system could generate a step change in the utility of MEG as a means to assess human electrophysiological brain activity and connectivity in health and disease. However, such a change is critically dependent, not only on the generation of new multi-channel OPM systems, but also on improved algorithms for forward modelling.

Chapter 4

Experimental MEG measurements using a single OPM

This chapter describes the use of a single commercial OPM to make measurements of evoked and induced signals in primary sensory cortex during median nerve stimulation. The use of interference cancellation via a reference array is shown to improve significantly the SNR of OPM measurements. Furthermore, the use of a 3D-printed scanner-cast helps to accurately inform sensor position and orientation, thus facilitating accurate forward modelling and source imaging. We show experimentally that OPMs generate the expected increases in signal magnitude over SQUID recordings, in agreement with the simulations in Chapter 3. Finally, using source modelling, the source of the evoked response is localised to somatosensory cortex, showing that with thirteen sequential OPM measurements, source-space SNR is comparable to that from a 275-channel SQUID system.
The work presented here was published in NeuroImage in 2017 (Boto et al., 2017).

4.1 Introduction

Recent advances in magnetometry have opened up the possibility of considering the next generation of MEG, based on on-scalp, cryogen-free magnetic field detectors. Thanks to the commercialisation of OPMs (QuSpin), OPM-MEG can now be envisaged. The simulation work described in Chapter 3 outlined the

potential of OPM-MEG in terms of SNR, reconstruction accuracy and spatial resolution. This chapter, and the rest of this thesis, is dedicated to the experimental realisation of this vision.

Although OPMs have the potential to form the basis of a high SNR and flexible MEG instrument, the practical implementation of such a system requires significant work. The increased signal provided by moving the detectors closer to the scalp is relatively easily achieved. However, translating this into high precision images of electrical brain function is non-trivial. First, most OPMs are configured as magnetometers (as distinct from gradiometers which are used in most SQUID-based MEG systems) and as such are more susceptible to environmental interference. Effective methods must therefore be employed to reduce this. Here, the use of interference cancellation in the OPM measurements via a reference array is explored (i.e. similar to ideas behind synthetic gradiometers (Vrba et al., 1991; Vrba and Robinson, 2001; Vrba, 2002)).

In addition, spatial specificity and reconstruction accuracy depend not only on SNR, but also on accurate modelling of magnetic fields generated by the brain (i.e. accurate forward solutions). This problem is exacerbated in OPMs since, perhaps counter-intuitively, increases in SNR mean that modelling accuracy must also increase. Indeed, this was shown in the simulations presented in Chapter 3, which predicted that even small (5%) modelling errors could negate any advantages in SNR afforded by OPM systems (Boto et al., 2016). One significant cause of modelling errors in current MEG systems comes from inaccurate knowledge of the head location relative to the sensor array (Hillebrand and Barnes, 2003; Liuzzi et al., 2017). It follows that to realise the benefits of an OPM system, detector locations and orientations relative to the brain anatomy must be known with high spatial accuracy. However, this is a big challenge for an OPM system where sensors are mounted flexibly on the head.

In this chapter, evaluation of a single, newly available, commercial OPM sen-

sor for MEG measurements is undertaken. We use this sensor in combination with a bespoke helmet, printed to fit a single individual based on their head shape and comprising slots for OPM housing. This allows for accurate placement of the sensor relative to brain anatomy. Sequential measurements of evoked and induced responses during median nerve stimulation are employed and simultaneous SQUID measurements are used to reduce environmental interference. We will show localisation of the source of the evoked response and compare source-space SNR between OPMs and SQUIDs.

4.2 Methods

4.2.1 Data acquisition

QuSpin OPM

The OPM used in this work was described in Section 2.1.2 - **The QuSpin sensor** of Chapter 2. As a recap: it has a theoretical noise level comparable to SQUIDs (10 fT/$\sqrt{\text{Hz}}$ above 1 Hz), a bandwidth of approximately 150 Hz, an operational dynamic range of $\pm$5 nT, a size of 14$\times$21$\times$80 mm^3, and can be placed such that the centre of the sensitive volume is 6.5 mm from the scalp head surface. The OPM sensor head is self-contained with all the necessary optical components, including a semiconductor laser for optical pumping, optics for laser beam conditioning, a 3$\times$3$\times$3 mm^3 ^{87}Rb vapour cell, and silicon photo-diode. The vapour cell is electrically heated to around 150 ^{o}C to achieve optimum ^{87}Rb vapour density. The sensor head connects to a small electronics controller via a 5-m cable. The electronics controller is placed outside the MSR to minimize magnetic interference. The output from the electronics controller is an analogue voltage proportional to magnetic field, with scaling factor being 2.8 V/nT.

Scanner-cast design

There are two practical problems with using a single (or a small number of) OPMs to detect neuromagnetic fields. First, the convoluted shape of the cortex means that, even if the approximate location of the region of interest in the subject's head (somatosensory cortex in our case) is known, the precise orientation of the local normal to the cortical surface is not. Since the locations of field maxima outside the head are strongly dependent on the direction of current flow, this means that it is difficult to predict where on the scalp sensors should be optimally placed. Second, in order to mathematically model the measured fields, and hence derive 3D images of changing cortical current flow, the precise location and orientation of the sensors relative to the brain anatomy must be known. We solved both of these problems via the use of 3D printing (see Figure 4.1).

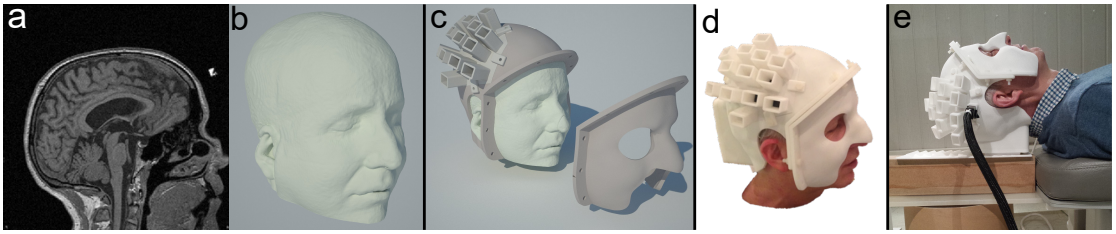


Figure 4.1: **Scanner-cast design and fabrication**. a) Single sagittal slice from the anatomical MRI. b) Outer head surface extracted from MRI. c) CAD model of the scanner-cast with slots designed to house the OPM sensors over sensorimotor cortex. d) 3D-printed scanner-cast on subject. e) Subject *in situ* with the OPM attached.

We used an anatomical MRI (Figure 4.1a) of the subject's head (as described in Tröebinger et al. (2014)) in order to extract a 3D mesh, representing the outer surface of the head and face (Figure 4.1b). Following this, a nylon cast of the outer head surface was fabricated using 3D printing[1], resulting in a scanner-cast that is moulded to the shape of the individual subject's head (Figure 4.1c/d). As part of the scanner-cast design, we digitally placed a nominally hexagonal array of slots for 13 radially-oriented OPMs over the subject's right somatosensory cortex. The array was located and oriented so as to sample the field max-

[1] `http://www.chalkstudios.co.uk/`

ima and minima expected at 6 mm from the scalp surface due to a dipole in the somatosensory cortex (whose location and orientation was estimated from previous SQUID-based dipole fits to the same subject). Importantly, since the scanner-cast was generated directly from the subject's MRI, the precise location and orientation of the slots for the sensors, with respect to the brain anatomy, were known. The multiple slots meant that the single OPM could be placed in any one of the 13 locations in order to sample the spatially varying scalp-level magnetic fields.

Median nerve stimulation and data collection

The somatosensory paradigm involved electrical stimulation of the subject's left median nerve, which was achieved by applying a series of 500-μs-duration current pulses to two gold electrodes placed on the subject's wrist. The current was delivered using a Digitimer DS7A (Digitimer Ltd., Welwyn Garden City, UK) constant current stimulator, and the amplitude was increased until movement of the thumb was observed. Each experimental run comprised 80 pulses delivered with an inter-stimulus-interval (ISI) of 3.0099 s; the ISI was selected not to be a multiple of the 20-ms period of the mains frequency (50 Hz). Data were recorded during a pre-stimulus baseline of 0.5 s and post-stimulus period of 2 s. A single run lasted four minutes. All recordings were carried out inside the MSR at the Sir Peter Mansfield Imaging Centre. During recording, the lights in the control suite (which operate at 50 Hz) were turned off, as was any unnecessary equipment, to minimize ambient interference. Lights in the MSR were also off, although these operate at DC and were not expected to generate interference.

The experiment was first carried out using a 275-channel whole-head CTF MEG system (MISL, Port Coquitlam, Canada) operating in third-order synthetic gradiometer configuration. The subject was positioned supine, with their head in the MEG helmet, whilst data were recorded at a 600-Hz sampling rate. Three

coils were attached to the participant's head as fiducial markers at the nasion, left and right pre-auricular points. These coils were energised periodically through acquisition to allow localisation of the head relative to the MEG sensor array. Before acquisition, the surface of the participant's head was digitised using a 3D digitiser (Polhemus Inc., VT, USA). Subsequent surface matching of the digitised head shape to an equivalent head shape extracted from the anatomical MRI allowed co-registration of brain anatomy to MEG sensor geometry. Note that the CTF system comprises 275 5-cm baseline axial gradiometers spaced evenly across the scalp surface, which are magnetically coupled to 275 SQUID sensors. Here, to simplify terminology, we refer to these as SQUID sensors throughout the chapter.

The median nerve experiment was repeated a further 13 times. The subject was positioned on the bed of the CTF system, with their head inside the scanner-cast and the scanner-cast fixed to the bed (Figure 4.1e). On each repeat of the experiment, the OPM was positioned in a different slot in the scanner-cast. In this way, a multi-channel MEG recording was simulated. The analogue output of the OPM was captured by analogue-to-digital converters (ADC) on the CTF MEG system (16-bit digitization, oversampled at 10 kHz to increase resolution). This allowed simultaneous data capture from the OPM as well as all channels in the CTF system. All channels were sampled at 600 Hz. Note that the CTF system also incorporates 29 reference channels, located in a separate array, distal to the subject's head. The simultaneous capture of OPM data alongside this reference array was exploited to compensate for interference. In addition to the median nerve experiment, 100 s of data were also recorded with no subject present, to assess ambient noise levels.

4.2.2 Data analysis

Initially, all MEG data (from the SQUIDs and the OPM) were filtered, either between 2 Hz and 80 Hz (empty room recording) or 0 Hz and 150 Hz (median nerve data – the 2-Hz high-pass filtering was omitted due to concerns regarding filter artefacts). For the median nerve data, the DC offset was removed based on the 100-ms pre-stimulus period. There was a delay between the SQUID and OPM recordings, with the SQUIDs leading the OPM by 3 data points (5 ms). This was caused by the digital signal processor running the OPM, and was measured by assessing the phase of the 50-Hz mains artefact measured using the OPM compared with the reference SQUID magnetometers. Having characterised the delay, it was corrected by time-shifting the SQUID measurements. All data analyses were undertaken using MatLab (Mathworks Inc., MA, USA).

Gradiometer formulation

In the current generation of commercial MEG devices, interference is compensated by the use of both hardwired gradiometers and reference arrays (e.g. used to form higher-order gradients). However, the OPM is configured as a magnetometer with no compensation for interference. Here, the simultaneous recording of our single OPM and multi-channel SQUID data was exploited in order to create a synthesised software gradiometer. The CTF instrument contains a 29-channel SQUID reference array, including 3 vector magnetometers (9 channels) as well as the 275 gradiometers in the helmet. Data from all channels were recorded simultaneously with the OPM and their locations (approximately between 50 cm and 100 cm from the OPM slots) were close enough for them to be sensitive to similar environmental interference, but far enough away that they were not sensitive to neuromagnetic signals. The CTF instrument was therefore used as a reference array: data were augmented by using their differentials with respect to time of the magnetometer channels, so as to allow any linear mix-

tures to have variable phase. These data were combined in a single (design) matrix and a linear regression was used to remove any linear combination of reference array (interference) signals from the OPM. In the median nerve data, this regression was applied trial-by-trial and in the 0–150-Hz range. For empty room data, the regression was applied over the full 100-s recording (since there were no trials). We also contrasted its application in the full 2–80-Hz frequency range, and independently within separate (overlapping, 5-Hz) frequency bands.

Evoked and induced responses

After correcting for interference using synthesised gradiometry, we assessed the sensor-level evoked and induced signals from the OPM and SQUIDs by forming the average over trials. The largest evoked responses for each of the 275 SQUID measurements, and the 13 OPM measurements, were extracted for comparison of both the temporal morphologies and response magnitudes. In addition to the averaged response, unaveraged evoked responses were also extracted from the OPM data (with and without synthetic gradiometer correction) to examine single-trial responses.

A time–frequency analysis was used to evaluate the induced (oscillatory) response. Sensor time series were frequency-filtered into a set of overlapping frequency bands and, for each frequency band, a Hilbert transform was used to calculate the analytic signal. The absolute value of the analytic signal was then derived to generate the amplitude envelope of oscillations (termed the Hilbert envelope). These Hilbert envelope time courses were averaged across trials and concatenated in the frequency dimension to generate a time–frequency spectrum (TFS). The SQUID/OPM locations with the largest response were used.

Source localisation and SNR

Inverse modelling was used to assess whether or not we could use OPM measurements to reconstruct the cortical generator of the evoked (N20) response. In doing so, the recordings made with the OPM sensor at different positions in the scanner-cast were used to simulate a "multi-channel" array, analysing all the data as if recorded simultaneously. Following the noise cancellation procedures, sensor data were baseline-corrected to the (–0.1)–0-s time window relative to stimulus onset. This allowed for identification of the temporal peak of the N20 response. Unfortunately, here, because the data from separate locations were recorded sequentially rather than simultaneously, we could not use the beamformer approach outlined in Chapter 3. We therefore employed a Bayesian dipole fitting procedure (similar to Kiebel et al. (2008)), implemented in SPM[2] to explain the OPM-measured fields at the time of the peak N20 response. A single-shell model of the inner skull was used for forward modelling. This Bayesian fitting scheme assigns a prior mean and precision to the dipole location and moment parameters. 20 starting points were randomly chosen (as the prior mean locations) within the brain and we assigned an uninformative prior spatial standard deviation of 10 cm to each of these locations. The prior mean and standard deviation of each moment parameter was set to 0 and 10 nAm respectively. The posterior location and moment parameters were optimised for each set of priors, so as to maximise the model evidence (or Free energy) over ten iterations (each iteration having a random starting point drawn from the prior distributions). Of these models and iterations, the most likely solution was taken to be the one with the highest overall model evidence. This same methodology was also applied to the SQUID recordings for comparison.

A direct comparison of sensor-space SNR using OPMs and SQUIDs is confounded for two reasons: first, it involves comparison of signals measured using

[2] http://www.fil.ion.ucl.ac.uk/spm

a SQUID gradiometer and OPM magnetometer. Second, significant "interference" in both systems comes from brain sources of no interest. By moving a detector closer to the brain (i.e. using an OPM rather than the SQUID), the sensitive brain volume (contributing the sources of no interest) changes (see Appendix). Specifically, a greater proportional sensitivity to shallow, compared to deep, sources is observed. This changing volumetric sensitivity profile means that the OPM and SQUID sensors have fundamentally different interference generators. For these reasons, the only means to generate unbiased estimates of SNR is to reconstruct source-space signals. Here, the dipole time course was reconstructed using a linear weighted sum of sensor measurements; weights were derived using the dipole fitting procedure. This was done independently for the 13 OPM measurements and the 275 SQUID measurements. SNR was measured in two ways: in both cases signal was estimated as the peak-to-peak change in the evoked response. In the first case, noise was estimated as the standard deviation in a baseline window between 0.6 s and 1.5 s post stimulus. In the second case, noise was estimated using a procedure whereby alternate trials were sign flipped prior to averaging. Following this anti-averaging procedure, the standard deviation of the whole trial was used to estimate noise.

4.3 Results

Figure 4.2 shows results of applying the synthetic gradiometer to the OPM data recorded in an empty room. Figure 4.2a shows magnetic field plotted as a function of time (left-hand plot) and in Fourier space as a function of frequency (right-hand plot). The red and blue traces represent OPM measurements with and without synthetic gradiometer correction, respectively. For comparison, the black trace shows a SQUID magnetometer (selected randomly from the reference array) and the green trace shows a SQUID gradiometer. Note that 97% of the variance measured at the OPM could be explained by interference measured

simultaneously by the SQUID reference array. In the Fourier plots, the centre panel shows the full frequency range, whilst the right-hand panel shows data around the 50-Hz peak. The uncorrected OPM has a mean noise level (MNL) of 31 fT/$\sqrt{\text{Hz}}$ in the 2–80-Hz frequency range, which reduces to 26.2 fT/$\sqrt{\text{Hz}}$ when using synthetic gradiometry. However, this reduction is clearly dominated by the 50 Hz mains frequency peak (which reduces from 12,512 fT/$\sqrt{\text{Hz}}$ to 180 fT/$\sqrt{\text{Hz}}$) and a 32-Hz peak (which reduces from 7,642 fT/$\sqrt{\text{Hz}}$ to 314 fT/$\sqrt{\text{Hz}}$). Whilst the origin of the 32-Hz peak is unclear, it was thought to relate to site-specific interference from an air conditioning system. The gradiometer formulation used here is simple: only a single (regression) mapping is employed to remove interference measured at the reference array from the OPM, meaning the necessary assumption that all interference sources have the same spatial profile. The mapping is thus dominated by the largest interference source (50 Hz) which explains why this gradiometer formulation is efficient in removing mains interference, but has little effect at other frequencies.

By comparison, Figure 4.2b shows gradiometer correction applied to individual frequency bands (5-Hz overlapping bands between 2–80 Hz). Here, we assume a different gradiometer mapping for each band (i.e. regression coefficients are derived optimally for all bands, allowing interference sources in different bands to exhibit different spatial profiles). The left panel shows the uncorrected (blue) and corrected (red) noise levels across 28 bands. The centre and right panels show time–frequency spectra before and after correction. Note that, as well as a marked reduction at 50 Hz, the efficiency of the synthesised gradiometer at other frequencies is also improved with mean interference (across bands) falling from 34.5 fT/$\sqrt{\text{Hz}}$ pre-correction to 15.9 fT/$\sqrt{\text{Hz}}$ post-correction.

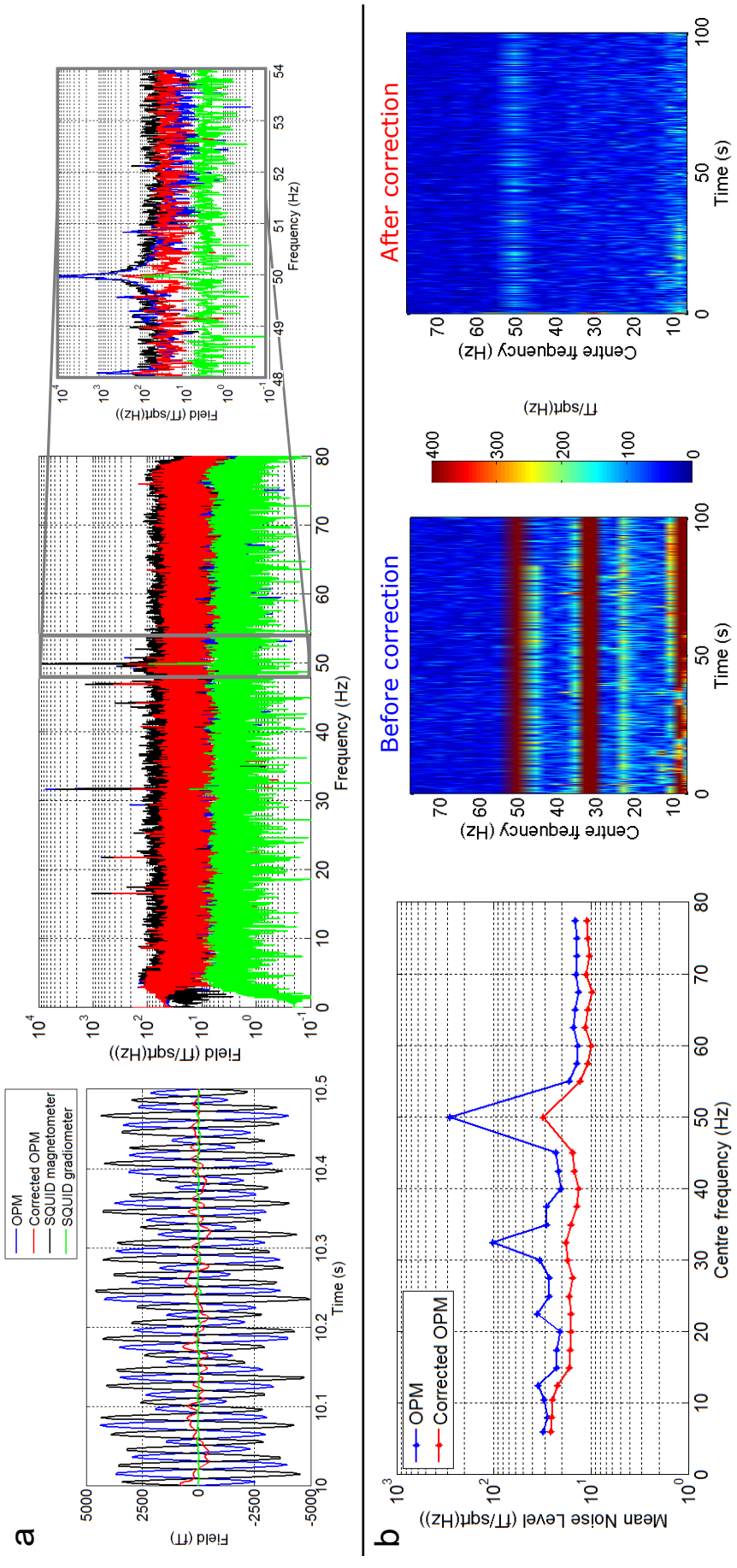


Figure 4.2: **Synthesised gradiometry.** a) Magnetic fields plotted in time (left) and frequency (right), measured in an empty room. Red and blue traces show the OPM data with and without gradiometer correction, respectively. The black trace shows a SQUID magnetometer and the green trace shows a SQUID gradiometer. b) Left hand side shows a noise amplitude spectrum when gradiometer correction is applied to individual frequency bands (empty-room noise). Uncorrected (blue) and corrected (red) OPM mean noise levels across 28 bands are shown. Centre and right panels show time–frequency spectra in fT/$\sqrt{\text{Hz}}$, before and after gradiometer correction.

Figure 4.3 shows a comparison of evoked and induced responses measured at the sensor level using the OPM and the SQUIDs. Figure 4.3a(i) shows the absolute magnitude of evoked responses (measured in fT) for the OPM (black) and the SQUID (red). In both cases, responses from the sensor location yielding the maximum response magnitude are shown. The close proximity of the OPM to the scalp surface produces approximately a fourfold increase in the magnitude of the measured signal, in line with previous simulations in Chapter 3 (Boto et al., 2016). Figure 4.3a(ii) shows the same signals, but the SQUID signal is multiplied by four such that temporal morphology can be compared: note the similarity in the OPM- and SQUID-measured responses. Figure 4.3a(iii) shows single-trial responses before and after gradiometer correction. Note here that the x-axis represents time, the y-axis represents trial number, and the colour represents measured field. Note that single-trial evoked responses can be seen following correction. Figure 4.3b shows TFSs representing the induced response to median nerve stimulation. It is well known that, in the sensorimotor system, movement and sensory stimulation is linked to changes in neural oscillations in the beta band (Hari and Salmelin, 1997; Cheyne, 2013; Kilavik et al., 2013). Specifically, following stimulation, a decrease in the amplitude of beta oscillations is observed followed immediately by a period of elevated amplitude, known as the post-stimulus beta rebound. This bimodal amplitude change, which occurs simultaneously with the evoked response, has been well characterised in previous work, and is extremely robust across individuals. Here, using both the SQUID and OPM, we observed the expected modulation with a stimulus-induced decrease and rebound in beta amplitude relative to baseline. Note again the similarity of time–frequency morphology of the response, and the approximate fourfold difference in scale of the two measurements. The left-hand plot shows the TFS for an OPM, the upper right plot shows the case for the SQUID, and the lower plot shows the SQUID measurement plotted on the same colour scale (–150 fT to 150 fT) as the OPM. Figure 4.3c shows the scalp-level

spatial topographies of both the evoked and induced responses.

Figure 4.4 shows source localisation of the evoked (N20) response. Figure 4.4a shows the averaged time courses across trials from all 13 OPM "channels" (in black) and 275 SQUIDs (in red). As expected, a bipolar response is observed with the positive and negative responses reflecting the direction of the magnetic field (out of the head and into the head, respectively). Left and right panels of Figure 4.4b show the spatial topography of magnetic field at the scalp level, across the 275 SQUID sensors and the 13 OPM scanner-cast locations, respectively. Both measured (bottom) and modelled (top) field maps are shown. The scatter plot in the centre panel shows the correlation between the modelled and measured fields for both OPMs (in black) and SQUIDs (in red). The degree of correlation for the OPMs is compelling, particularly given that the 13 "channels" were measured independently using only a single sensor and 13 separate runs. Figure 4.4c shows three separate views of the N20 evoked response localisation, overlaid onto the subject-specific (MRI-extracted) cortical mesh. The motor strip has been highlighted in green and the sensory strip in blue. The source location derived from OPMs is in black and the location derived from SQUIDs is in red. The coordinates and orientations of both dipole locations are shown in Table 4.1. Note that both dipoles localise to the right primary somatosensory cortex (S1) as would be expected. One should note here that these are source estimates based on different sensor types and for the OPMs these data represent the concatenation of 13 sequentially recorded runs, which were subsequently treated as being simultaneously acquired i.e. the OPM data are contaminated with an extra source of between-session physiological variability.

This evidence shows clearly that OPMs (even collected sequentially in the absence of a multi-channel system) can be employed to derive images of the spatial distribution of electrophysiological changes in the brain. Figure 4.4d shows source-space reconstructed dipole time courses, generated independently using OPMs (black) and SQUIDs (red). The shading represents standard error

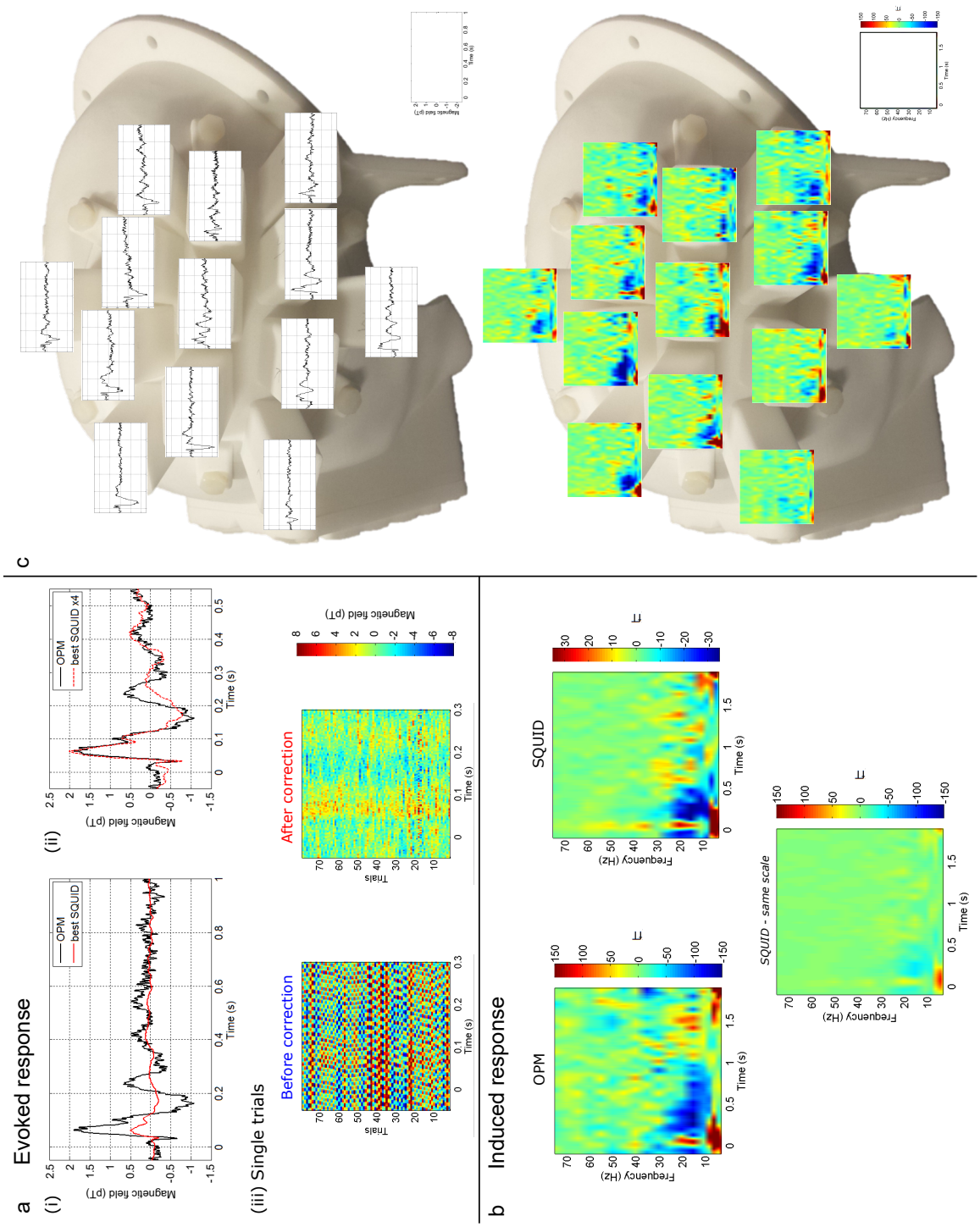


Figure 4.3: Sensor level results of the principal evoked and induced responses. a) (i) Measurements of the evoked response (in fT) for both the OPM (black) and SQUID (red). (ii) Same data as in (i) but with the SQUID time course multiplied by four to allow direct comparison of temporal morphology. (iii) Single-trial evoked responses measured using OPM with (right) and without (left) gradiometer correction. b) TFS showing the 0–80-Hz oscillatory signature of median nerve stimulation in fT. Upper left-hand panel shows OPM, upper right-hand panel shows SQUID, and lower panel shows SQUID plotted on the same colour scale as the OPM for comparison. c) The scalp-level spatial topographies of the evoked and induced responses, overlaid onto the scanner-cast.

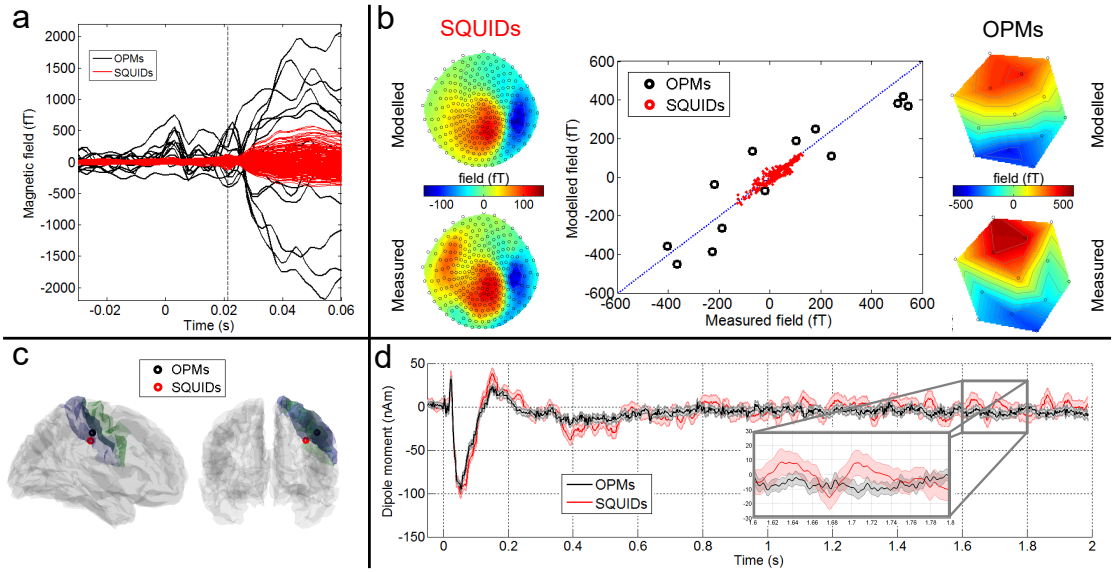


Figure 4.4: **Source localisation of the evoked response**. a) Averaged time courses of OPM data (black) recorded at the 13 different sensor locations across the scanner-cast, and SQUID data (red) corresponding to the 275 SQUID channels. b) Left and right panels show the scalp spatial topography for the SQUIDs and OPMs, respectively, of the measured (bottom) and modelled (top) fields. The centre plot shows correlation between the modelled and measured fields for the OPMs (black) and SQUIDs (red). c) Two views of the N20 evoked response location. Marker shown in black (red) corresponds to localisation using the OPM (SQUID) system. d) Reconstructed dipole time courses using the OPM (black) and SQUID (red) data.

across trials. Note the clear similarity in both morphology and amplitude. Note also that the standard error over trials (itself a measure of noise) is generally smaller in the OPMs compared to the SQUIDs.

Table 4.1: **Source localisation of the evoked response**. Coordinates (in mm) and orientation of the evoked response location in MNI coordinates for the OPMs and SQUIDs.

	Coordinates (mm)			**Orientation**		
	x	y	z	x	y	z
OPMs	45.21	–23.44	42.89	0.73	0.68	0.11
SQUIDs	34.76	–25.22	35.40	0.98	–0.19	0.01

Source-space SNR was estimated as described above for the evoked response. OPM SNR was estimated as 42.52 and 26.99 using the windowed and anti-averaging methods respectively. Similarly the SQUID evoked response SNR was estimated as 21.41 and 19.79 using the equivalent two methods. These measures show an improvement of either 1.99 or 1.36 in evoked response SNR of OPMs compared to SQUIDs, depending on measurement method used. It should

be noted that source-space SNR improves with the number of sensors used, and here we contrast 275 SQUIDs to only 13 OPMs.

4.4 Discussion

This chapter has shown that a commercially available QuSpin sensor is able to achieve a sensitivity similar to that of SQUIDs. This means that cryogen-free MEG, with a scalp-mounted sensor placement, higher SNR (see Chapter 3), and potentially lower cost, can now be considered possible. In this chapter, it has been shown that an appropriately configured OPM system based on prototype QuSpin sensors could have a source-space SNR comparable to or better than current SQUID systems. Chapter 3 suggested that the effective use of an OPM system in generating accurate 3D depictions of the changes in brain current depends not only on OPM data with high SNR but also accurate knowledge of sensor placement relative to the cortex. Here, synthetic gradiometry was shown to represent a useful means to cancel interference, whilst the use of 3D printing allowed to accurately locate the sensor on the scalp surface, with a known position and orientation relative to brain anatomy.

4.4.1 Gradiometry

The fabrication of a reference array, located sufficiently far from the head to be insensitive to the neuromagnetic field, but sufficiently close to pick up the same environmental interference, has been a strategy for reduction of interference since the earliest multi-channel SQUID devices were introduced (Vrba et al., 1991; Vrba and Robinson, 2001; Vrba, 2002; Vrba and Robinson, 2002). Indeed this is the idea behind the synthetic third-order gradiometer approaches used in commercially available CTF instruments. Here, a similar procedure was employed, using the SQUID system to remove interference recorded at the OPM.

The method used is based on a simple regression of the reference signal. Although this was effective (in empty room data, 97% of variance in the OPM signal was explained and removed by the technique) it represents only a simple demonstration and it relies on all interference fields having the same spatial signature. For example, consider a situation in which two separate interference sources exist, but with different spatial variation across the shielded room: interference source A has a greater magnitude at the OPM compared to the reference array, whereas interference source B has greater magnitude at the reference array compared to the OPM. In our simple regression formulation, a single set of weights would be used to map the reference to the OPM, meaning that a single mapping would have to account for both sources. This means that the prediction of source A interference at the OPM, based on the reference, would likely be an under-estimate, and similarly the prediction of source B interference would be an over-estimate. In other words, no single set of weights can account for both sources. In reality, the mapping will be best "tuned" to the largest source of interference, and this is why, in Figure 4.2a where a single mapping is used across all frequencies, the 50-Hz mains artefact is well suppressed, but little effect is noted at other frequencies. Here, this problem was ameliorated somewhat by assuming that separate interference sources manifest within different frequency bands, and therefore using regression coefficients derived independently for each band, resulted in a greater efficiency of interference cancellation (Figure 4.2b). However, if more than one interference source exists within a single band, then the same problem results. Importantly, a significant limitation of the approach taken here is that the reference channels cover a relatively small spatial volume within the MSR – meaning that the interference magnitude is approximately constant for all channels (i.e. the spatial variation of interference is poorly sampled). This is a consequence of using SQUID reference sensors since all reference sensors must be kept within the liquid helium dewar. If we were to employ non-cryogenic devices as references, no such limitation

would apply and the spatial variation of the interference inside the MSR could be better characterised and linear (or even non-linear) mappings to the OPM array at the scalp might yield more efficient interference cancellation. Further, extra channels could even be placed close to common sources of biological interference (e.g. the heart) such that interference from these sources could also be more efficiently removed. This, coupled with the band-specific approaches demonstrated here, could facilitate improved efficiency of synthetic gradiometer interference cancellation.

4.4.2 Scanner-casts

Perhaps one of the most important factors in this experimental set-up was the use of 3D printing to specify, *a priori*, the configuration of sensors and to stabilise them relative to the head and the MSR during data collection. 3D printing is becoming commonplace for fabrication of structures with unusual geometries. Here, the scanner-cast print was based on the surface of the subject's scalp extracted from their anatomical MRI. Then, the sensor locations were placed above the right somatosensory cortex to optimally capture the maximum and minimum of the magnetic field produced by the N20 response to median nerve stimulation. As such, the scanner-cast used was designed to target a specific region of interest, facilitating high specificity with relatively few (13) sensor locations. It is noteworthy that this same idea could be used to target any cortical (or subcortical) region, as long as one knows the location and orientation of the interesting segment of cortical surface, information which can be obtained from anatomical MRI. Equally important here was the fact that the 3D-printed scanner-cast meant that the location of the sensitive volume of each sensor, and its sensitive orientation relative to the brain anatomy, was known accurately. This information is critical if one is to perform accurate localisation of the neuronal generators of the recorded neuromagnetic signals (and becomes all the more important

now that the relative sensor locations are no longer fixed by cryogenics). As noted above, accurate forward modelling is extremely important in all MEG recordings, but becomes of greater importance when the SNR of the data is increased. Briefly, the previous chapter (and associated paper (Boto et al., 2016)) has shown that, with increasing error on the forward model, (beamformer) inverse solutions fail faster in the presence of high-SNR OPM data compared to lower-SNR SQUID data. It is for this reason that the 3D-printing technology used here is an important step to ensure a well characterised detector array. The approach taken, which involves an individual MRI followed by bespoke printing of a subject specific scanner-cast, may seem expensive and complex, however it removes a number of potential sources of modelling error. This is particularly important as we set out to characterize the sensitivity and crosstalk between these new sensors but one would hope with time, the positioning requirements will become less stringent as the sensors become more completely characterized (López et al., 2012; Martínez-Vargas et al., 2016). The future use of flexible (EEG/fNIRS type) caps and an optical system for sensor location and orientation measurements (Zetter et al., 2019) may also be viable.

4.4.3 Signal magnitude and SNR

One of the principal advantages of OPMs over SQUIDs is the reduced distance between cortical source(s) and sensors. Because neuroelectrical sources are dipolar, the fields that they generate follow the inverse square law, giving rise to a non-linear increase in signal magnitude as the sensors move closer to the skull. This means that the magnitude of the measured signal using an OPM is larger than that recorded using a SQUID. This comparison is illustrated in Figure 4.3a which shows an approximately fourfold increase in signal magnitude for evoked and induced responses. However, this comparison requires explanation: first, the degree of improvement afforded by the OPM is a function of the

location of the source of interest in the brain. This is shown by the calculation in the Appendix to this chapter. The non-linear nature of the inverse square law means that, although moving detectors closer to the scalp will offer an increase in signal magnitude for all brain regions, the improvement for shallow sources will be larger than for deep sources. More specifically, whilst improvements in the cortex (shallow sources) could be as high as eightfold, improvements for deeper sources (e.g. thalamus) may be closer to twofold. This means that the observed increases in signal magnitude, whilst typical for the cortex, will not be achievable across the whole brain. Second, here we compare the magnitudes of effects measured using a magnetometer (OPM) and gradiometer (SQUID). The gradiometer is hardwired and comprises two coils, oriented radially with a 5-cm baseline. Both coils will pick up the neuromagnetic field and the subtraction of the signal measured at the coil farthest from the head, from that closest to the head, will mean a slight reduction of the response magnitude compared to a SQUID magnetometer (in which only the closest coil would be used). In this case, we estimate a SQUID magnetometer at the position of the closest gradiometer coil would likely increase the signal by approximately 36% (based on nearest sensor to source distance of 53 mm). In summary, this result confirms that OPMs offer increased signal magnitude compared to SQUIDs. However, this advantage is inhomogeneous with respect to location, and is tempered marginally by gradiometer measures.

For the above reasons, these two systems were compared in source space. Such a comparison takes into account both the ability to reduce environmental interference (e.g. via gradiometry) and to suppress brain sources of no interest from modelled time courses (itself a function of sensor-space SNR). Less variability was found in the source-level evoked response over trials when using the OPM, even though the OPM data were recorded over multiple sessions (i.e. had an extra source of physiological noise). The other SNR metrics agreed with this in showing a comparable or marginally better SNR from OPMs compared

to SQUIDs, even despite the fact that we use 275 SQUID locations and only 13 OPM locations.

4.5 Conclusions

In this chapter, we have presented MEG recordings made with a single OPM in combination with a 3D-printed scanner-cast designed to accurately locate and orient the sensor. Because OPMs are configured as magnetometers (as distinct from gradiometers) they are highly sensitive to environmental interference. However, this problem was ameliorated via the use of simultaneous reference sensor recordings. Using median nerve stimulation, it was shown that the OPM can detect both evoked and induced changes when placed over somatosensory cortex, with signals exhibiting $\sim$4 times the magnitude of equivalent metrics made using SQUIDs. OPMs were able to localise the source of the evoked response to somatosensory cortex, showing comparable or better SNR than SQUIDs. These results highlight the opportunity to now move forward towards a multi-channel OPM-MEG device.

4.A Appendix

The improvement in the magnitude of the measured MEG signal afforded by moving a detector closer to the head is dependent on the location in the head of the source generating the signal. To show this dependence, a simple analytical calculation can be undertaken. Consider the system in Figure 4.5a where a current source is located at position $\mathbf{r}_Q$ inside a volume conductor, G, and a detector is located at position $\mathbf{r}$ outside G. As shown in Chapter 1 (Equations 1.8 and 1.9), the magnetic field, $\mathbf{B}$, at $\mathbf{r}$ is given by the Geselowitz formula:

$$\begin{aligned}\mathbf{B}(\mathbf{r}) = \frac{\mu_0}{4\pi}\int_G \mathbf{J}_p(\mathbf{r}_Q) \times \frac{\mathbf{r}-\mathbf{r}_Q}{|\mathbf{r}-\mathbf{r}_Q|^3} dv' \\ - \frac{\mu_0\sigma}{4\pi}\int_S V(\mathbf{r}) \cdot \hat{\mathbf{n}}(\mathbf{r}') \times \frac{\mathbf{r}-\mathbf{r}'}{|\mathbf{r}-\mathbf{r}'|^3} dS.\end{aligned} \tag{4.1}$$

Here, $\mathbf{J}_p$ denotes primary current flow and thus the first term, which represents a volume integral over G, computes the magnetic field arising from primary (dendritic) current flow. In the second term, which represents an integral over the surface S that bounds the conductor, G, V denotes electrical potential, σ represents conductivity inside the conductor, $\mathbf{r}'$ is any point on the surface, S and $\hat{\mathbf{n}}(\mathbf{r}')$ is a unit vector normal to S at $\mathbf{r}'$. The second term describes the contribution of volume currents to the magnetic field at $\mathbf{r}$. To simplify the calculation, we assume that G is spherical. Further, we assume that only the radial component of the field is measured (which is the case for the experiments carried out here so that the measured field, $B_r(\mathbf{r}) = \mathbf{B}(\mathbf{r}) \cdot \hat{\mathbf{e}}_r(\mathbf{r})$ where $\hat{\mathbf{e}}_r(\mathbf{r})$ is a unit radial vector at $\mathbf{r}$. In this case, since $\hat{\mathbf{n}}$ is parallel to $\mathbf{r}'$ and the radially-oriented detector means that $\hat{\mathbf{e}}_r$ must be parallel to $\mathbf{r}$, the volume current term is reduced to zero and the measured field is approximated as

$$B_r(\mathbf{r}) = \frac{\mu_0}{4\pi}\int_G \mathbf{J}_p(\mathbf{r}_Q) \times \frac{\mathbf{r}-\mathbf{r}_Q}{|\mathbf{r}-\mathbf{r}_Q|^3} \cdot \hat{\mathbf{e}}_r(\mathbf{r})\, dv'. \tag{4.2}$$

If we further assume that the primary current, $\mathbf{J}_p$, is a current dipole, so that $\mathbf{J}_p = \mathbf{Q}\delta(\mathbf{r}' - \mathbf{r}_Q)$ (where $\delta(\mathbf{r}' - \mathbf{r}_Q)$ is the Dirac delta function and $\mathbf{Q}$ represents the magnitude and direction of the dipole). The measured radial field then reduces to

$$B_r(\mathbf{r}) = -\frac{\mu_0}{4\pi}\frac{(\mathbf{Q} \times \mathbf{r}_Q) \cdot \hat{\mathbf{e}}_r}{|\mathbf{r} - \mathbf{r}_Q|^3}. \tag{4.3}$$

Considering a dipole oriented normal to the radial direction (specifically, the $\hat{\mathbf{z}}$-direction – see Figure 4.5a) and (without loss of generality) limiting $\mathbf{r}$ and $\mathbf{r}_Q$ to a single plane, Equation 4.3 reduces further to

$$B_r(\mathbf{r}) = -\frac{\mu_0|\mathbf{Q}||\mathbf{r}_Q|\sin(\phi)}{4\pi(|\mathbf{r}|^2 + |\mathbf{r}_Q|^2 - 2|\mathbf{r}||\mathbf{r}_Q|\cos(\phi))^{3/2}} \tag{4.4}$$

This simple expression allows an approximation of the measured field, for different scalp-detector distances (which can be set using $|\mathbf{r}|$) and different source depths (which can be set using $|\mathbf{r}_Q|$). The expression in Equation 4.4 is asymmetric with respect to the angle ϕ (between $\mathbf{r}$ and $\mathbf{r}_Q$) and the angle at which the maximum field is found varies as a function of both $|\mathbf{r}|$ and $|\mathbf{r}_Q|$. Specifically, the optimal angle at which a sensor is placed is found by differentiating 4.4 so that

$$\cos(\phi) = \frac{-(|\mathbf{r}|^2 + |\mathbf{r}_Q|^2) + \sqrt{|\mathbf{r}|^4 + |\mathbf{r}_Q|^4 + 14|\mathbf{r}|^2|\mathbf{r}_Q|^2}}{2|\mathbf{r}||\mathbf{r}_Q|}. \tag{4.5}$$

In order to assess the improvement in signal magnitude afforded by OPMs, as a function of dipole depth in the head, Equations 4.4 and 4.5 were used. We assumed that the head was spherical with radius 10 cm. A superconducting gradiometer (5-cm baseline) was placed 3 cm from the scalp surface (i.e. a gradiometer was simulated by computing B_r twice, with $|\mathbf{r}| = 13$ cm and $|\mathbf{r}| = 18$ cm, and subtracting the results). An OPM (magnetometer) was placed 6 mm from the scalp surface (i.e. $|\mathbf{r}| = 10.6$ cm). A source magnitude of $|\mathbf{Q}| = 10$ nAm was used and the dipole depth was varied by changing $|\mathbf{r}_Q|$ between 1 cm and 9 cm. The angle at which the detector was placed, ϕ, was defined independently

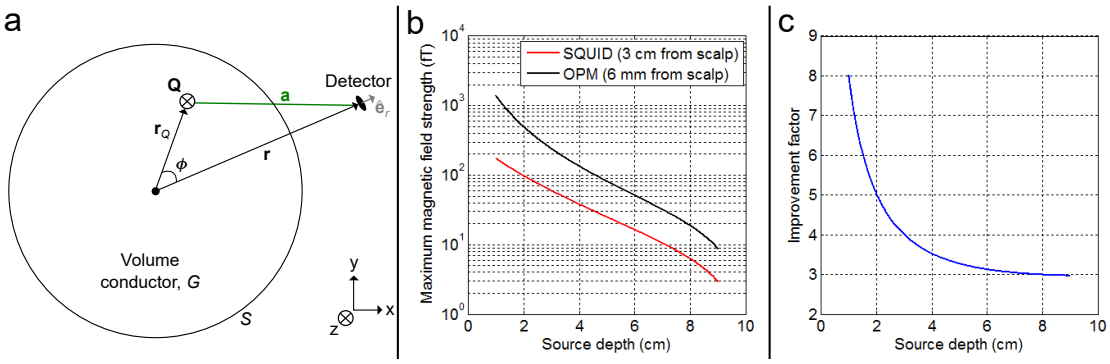


Figure 4.5: **Assessing signal magnitude as a function of source depth**. a) Schematic of a simple analytical model. b) Magnitude of the measured radial magnetic field as a function of source depth for SQUID (red) and OPM (black). c) The measured improvement (ratio of fields measured by OPM and SQUID) as a function of depth.

for all by Equation 4.5, and was larger for deeper sources as expected. Results are shown in Figures 4.5b and 4.5c.

Figure 4.5b shows the analytically-calculated magnitude of the magnetic field, for an OPM (black) and a superconducting coil (red), as a function of source depth in the brain (source depth = $10-|\mathbf{r}_Q|$ cm). Note that the OPM offers an improvement in source magnitude for sources anywhere in the brain, however, the field magnitude falls off faster with increasing depth in the OPM compared to the SQUID gradiometer. This means a greater amplification of nearby sources compared to distal sources when using an OPM detector. This effect, which is a consequence of the inverse square nature of Equation 4.1, is further demonstrated by Figure 4.5c which shows the improvement afforded by an OPM compared to a SQUID gradiometer as a function of depth. Note that improvement is calculated as the ratio of fields measured by OPM and SQUID gradiometer (i.e. a value of 5 means the OPM signal is 5 times that of the SQUID). For shallow sources, an eightfold improvement in signal magnitude is predicted, however, this improvement falls to only a threefold increase when considering sources close to the centre of the brain. This observation has important consequences for understanding SNR differences between the two systems. In this chapter, in both the SQUID and OPM systems, (following gradiometer correction) signal from the brain dominates environmental interference and so

the challenge of enhancing SNR becomes more about suppressing “brain noise” rather than environmental noise. For relatively shallow (cortical) sources like the somatosensory source in our experimental results, the more rapid fall-off of signal with depth gives the OPM a natural advantage compared to the SQUID.

Chapter 5

Towards wearable OPM-MEG

This chapter builds on the previous two chapters by describing the fabrication and testing of a prototype multi-channel MEG instrument based on OPMs. Unlike conventional MEG systems where subjects are forced to remain still, our OPM-MEG device allows subjects to make natural movements while being scanned. This is possible due to a novel system for nulling the background magnetic field allowing the OPM sensors to operate normally while experiencing subject movement. Here, we demonstrate measurement of reliable electrophysiological data whilst a subject is free to move their head around.
The work presented here was published in Nature in 2018 (Boto et al., 2018).

5.1 Introduction

In Chapter 4 the viability of a single commercially available QuSpin sensor to detect MEG signals was demonstrated. High-SNR MEG data were afforded by gradiometry, and precise localisation of the sensor on the scalp was facilitated via a 3D-printed scanner-cast. This now opens up an opportunity to begin constructing a multi-channel MEG device based on QuSpin sensors.

It is important to note the limitations of the work described in Chapter 4: first, the OPM measurements were undertaken sequentially, moving a single sensor between different locations (or slots) within the scanner-cast. It is for this reason that adaptive source localisation methods like beamforming could not be

employed. Second, the scanner-cast itself was attached to the bed and therefore the subject was unable to move, like in conventional SQUID-based MEG. Third, high-SNR measurements were afforded by gradiometry, which required the SQUID reference channels, making OPMs reliant on the SQUID system. Finally, all OPM-MEG data were collected using the CTF DAQ system. In order to fully realise the potential of OPM technology, these limitations must be lifted, meaning that significant engineering challenges remain.

In principle, moving from sequential to multi-channel measurements only requires increasing the number of OPM sensors. However, the operation of a multi-channel array is complicated by crosstalk between sensors from both the internal field-zeroing coils, and from the field modulation used for lock-in detection. These interfering fields between sensors in close proximity could significantly alter the sensor gain, and potentially the orientation of the sensitive axis of detection.

The flexible and lightweight nature of OPMs means that an OPM-MEG system could be adaptable to any head size or shape and potentially be worn on the head allowing the subject to move freely during data acquisition (like e.g. EEG). This would not only mean that babies, children and adults could be scanned in the same system, with no loss of SNR, but would further increase the patient populations that can be studied (e.g. patients with movement disorders). This type of non-restrictive MEG would also allow new neuroscientific paradigms and more natural stimuli to be delivered in MEG experiments, (e.g. virtual reality or social interaction). The flexibility of sensor positioning would also allow for unconstrained positioning of reference sensors, lifting the reliance on a nearby SQUID-based device.

However, a barrier to free movement during scanning is the remnant magnetic field inside the MSR. Even in the best (practical) shielded rooms, the remnant magnetic field is 6–9 nT (3-layer MSR) or even $\sim$30–60 nT (2-layer). Any

rotation of an OPM in this offset field will cause a massive change in the field experienced by the sensor, much larger than both the fields from the brain, or indeed the dynamic range of the sensor – e.g. even a 4 degree rotation would generate a 1.5-nT change in field, rendering an OPM inoperable. In addition, the remnant magnetic field in the room is unlikely to be homogeneous (in fact spatial changes are $\sim$10 nT/m in our MSR), meaning that even small translations of an OPM would generate artefacts and a 15-cm translation would take an OPM outside its dynamic range. For these reasons, a system to null the residual magnetic field inside the MSR would be required.

Finally, if the head were to be allowed to move, a solution for movement tracking would be required.

In this chapter, the fabrication and testing of a multi-channel OPM-MEG system will be described. In Section 5.2 the system itself will be described, including fabrication of a multi-channel array, field-nulling coils, reference array, crosstalk and gain changes in a changing background field. The initial demonstrations of this system are then described, showing that it can be used to capture MEG data even in the presence of large subject movements.

5.2 OPM-MEG instrument description

In this section, first a general overview of our OPM-MEG system is given. Following that, some of the considerations critical to its operation are described in detail.

It should be noted that the fabrication of this system was a collaborative effort. The field-nulling coils were designed and built by Niall Holmes. The digital acquisition system was built by James Leggett. The crosstalk measurements were undertaken by Gillian Roberts. For completeness in this thesis, I describe all of these.

5.2.1 System overview

A schematic diagram of the OPM-MEG system is shown in Figure 5.1. It comprises 13 QuSpin OPM sensors (these are similar to that used in the previous chapter, with the only difference being that the ones used here had a slightly smaller footprint, see also Section 2.1.2 - **The QuSpin sensor** in Chapter 2). These are mounted in a 3D-printed scanner-cast worn by the subject (*scalp array*). A further four sensors are located close to the head (but far enough away not to measure neuromagnetic fields) which are used as reference channels (*reference array*). Each sensor produces an analogue voltage output, proportional to the magnetic field perpendicular to the laser beam (scaling factor = 2.7 V/nT). The sensor outputs are digitised at a sample rate of 1,000 Hz, using a 16-bit digital acquisition (DAQ) system (National Instruments, Austin, TX) controlled using custom-written software in LabVIEW. The system is housed inside the MSR and all control equipment is kept outside the room to minimise its effect on MEG measurements.

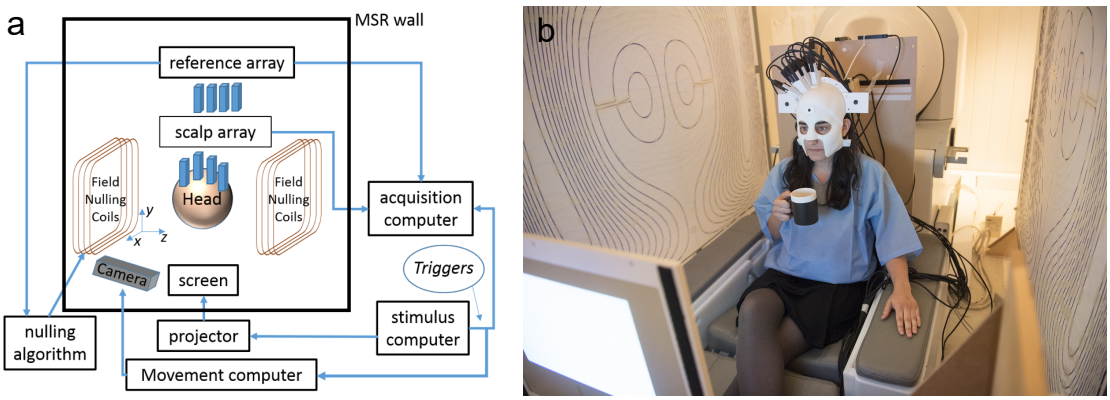


Figure 5.1: **System overview.** a) Schematic diagram showing an overview of system hardware. b) Photograph of subject *in-situ*.

The subject is surrounded by two planar electromagnetic coils (field-nulling coils, shown in Figure 5.1). Before acquiring MEG data, the residual static magnetic field and first-order gradients present inside the MSR are nulled. This is achieved using the reference array, which measures the background field and thus enables identification of the current needed for the coils to best cancel the

remnant magnetic field. The reference sensors were located and oriented such that the three Cartesian components of the magnetic field (B_x, B_y and B_z), and the two dominant gradients of the field components (dB_x/dz and dB_z/dz) could be measured close to the head. Reference array measurements were input to a proportional integral derivative (PID) algorithm, which was used to control the currents in the field-nulling coils. This allows the calculation of coil currents which generate fields that are equal and opposite to those measured by the reference array, thus attenuating the static field over the volume spanning the subject's head. This step is critical if the head is to be allowed to move during MEG data acquisition, since without field-nulling, changes in head position or orientation produce large variations of the field at the scalp array sensors, because they rotate or move in the remnant field.

During data acquisition, all 17 sensors (13 sensor scalp array and 4 sensor reference array) were operated simultaneously, with the reference sensors used to characterise temporally varying background magnetic interference, which was later regressed from the signals recorded by the scalp-mounted sensors.

The visual cue for paradigm control was generated by a separate stimulus computer. This was coupled to a data projector which projected the cue image through a waveguide onto a back-projection screen positioned $\sim$40 cm in front of the subject. The stimulus computer also generated TTL trigger pulses of 1 s duration denoting the onset of the stimulation. These trigger signals were input to the DAQ and sampled, simultaneously with the OPM data, at 1,000 Hz. Throughout data acquisition, an Xbox Kinect camera (Microsoft, Redmond, WA, USA) was used to measure head movement. Video data were captured using a third computer, which also recorded the trigger channels so that movement data could be later analysed on a trial-by-trial basis.

5.2.2 Nulling coils[1]

Even though our OPM-MEG system is housed inside the MSR, the remnant magnetic field inside is ∼30 nT, and spatially inhomogeneous. Any sensor movement through this field during a MEG recording would result in a field change much larger than the fields of interest, and would likely exceed the OPM's narrow (±5 nT) operational range. In addition, such changes can modulate the sensor gain (see Section 5.2.3 - **Sensor gain**). To ameliorate this problem, we constructed a set of bi-planar electromagnetic coils designed to generate fields equal and opposite to the remnant magnetic field, thereby cancelling it out (Holmes et al., 2018).

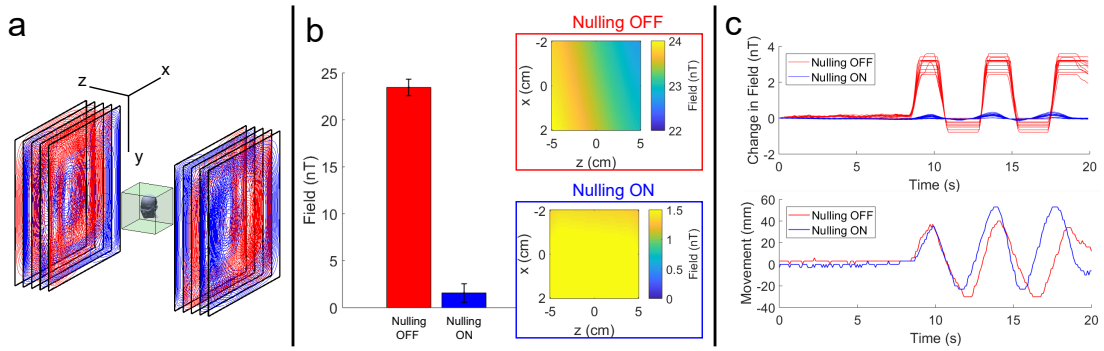


Figure 5.2: **Bi-planar nulling coils.** a) Schematic of the coils, which are confined to two planes surrounding a 40×40×40-cm^3 region of interest in which the head is allowed to move. The 5 separate layers represent wire paths that generate fields B_x, B_y, B_z, dB_x/dz and dB_z/dz. b) Bar chart showing field magnitude of B_x with (blue) and without (red) the field nulling. Inset images show spatial field variation of B_x. c) The upper plot shows the output of the 13 OPMs over time whilst the subject nods their head (head movement shown in lower plot). Blue and red traces show the cases where the field-nulling system was on and off, respectively.

The coils were designed on two 1.6×1.6-m^2 planes, placed either side of the subject with a 1.5-m separation (Figure 5.2a). Three coils generated spatially uniform fields (B_x, B_y and B_z) whilst two additional coils were used to remove the dominant spatial field variations (dB_x/dz and dB_z/dz). In this way, unlike standard field-nulling technologies (e.g. tri-axial Helmholtz coils), the system was able to account for spatial variation of the field over a 40×40×40-

[1]Work in this section was undertaken by Niall Holmes. A summary is given here for completeness.

cm^3 volume of interest enclosing the head. Further, we were able to cancel all components of the field vector using coils confined to just two planes, hence retaining easy access to the subject. Four reference OPM sensors were coupled to the coils in a feedback loop to null the residual static field in the volume of interest. Figure 5.2b is an example of how the magnitude of B_x and its variation across a 10-cm region around the subject's head are reduced after field-nulling. The static field was reduced from 23.5±0.9 nT to 1.6±1.0 nT and dB_x/dz was reduced from 10 nT/m to 0.28 nT/m. Figure 5.2c shows OPM measurements made during 7-cm head movements, with (blue) and without (red) field nulling. The results show that without field nulling the OPM sensors fail (evidenced by the saturation), however with field nulling the OPMs are able to capture MEG data even with the head moving.

5.2.3 Sensor gain

At any single point in time, the OPM cell can be thought of as experiencing two magnetic fields: one (time-varying) field due to the brain, and a second (temporally invariant) field due to the background static magnetic field. At the beginning of the experiment, the latter is reduced by the field-nulling coils over a large volume through which the head can move. Although inevitably this cancellation is imperfect, it is sufficient to allow the sensors to remain operational in the presence of head movements, and to reduce the movement-related artefact to a manageable level (see Figure 5.2c). However, a more subtle effect is that changes in the background field also alter the gain of the OPM. Specifically, as the background field increases the gain of the sensor reduces and the OPM sensitivity to neuromagnetic fields drops. For the purposes of the present work, it is critical that this effect is characterised, since significant variation in the gain across an experiment would degrade the accuracy of the beamformer spatial filter used to process the data.

As seen in Section 2.5 - **Signal equations** of Chapter 2, the measured output of a single OPM channel (i.e. the output of the photo-diode) is a Lorentzian function of the magnetic field inside the vapour cell. In practice, an oscillating field of frequency ω, oriented perpendicular to the laser beam, is added by on-board coils. This allows us to read out a signal proportional to the component of the time-varying field that is parallel to the modulation field. To illustrate this mathematically, we assume that the laser beam is oriented along the $\hat{\mathbf{z}}$-axis, and the field of interest in the cell, B_x, is oriented in the $\hat{\mathbf{x}}$ direction, as is the modulation field. In this case, the output OPM signal (which is proportional to polarisation in the $\hat{\mathbf{z}}$ direction, $P_z(\omega)$) is given by a solution to the Bloch Equation (Cohen-Tannoudji et al., 1970; Shah and Romalis, 2009):

$$P_z(\omega) \propto \frac{\gamma\tau B_x}{1+(\gamma\tau B_x)^2} \sin\omega t \; J_0\left(\frac{\gamma B_{\text{mod}}}{\omega}\right) J_1\left(\frac{\gamma B_{\text{mod}}}{\omega}\right). \tag{5.1}$$

Here, γ is the electron gyromagnetic ratio and $\tau\,(= R + 1/T_2)^{-1}$ is the atomic spin coherence time, which is a function of both the optical pumping rate, R, and the relaxation time T_2. J_0 and J_1 are Bessel functions of the first kind and B_{mod} is the modulation field amplitude. Assuming a lock-in process is used to measure the component of P_z varying at frequency ω then, since the product $\left(\frac{\gamma B_{\text{mod}}}{\omega}\right)$ is constant, we can write

$$P_z(\omega) \propto \frac{\gamma\tau B_x}{1+(\gamma\tau B_x)^2}. \tag{5.2}$$

Now assume that the field component of interest, B_x, comprises two parts: a static or background field, $B_x^{(\text{static})}$, and a neuromagnetic field δB_x so that

$$B_x = B_x^{(\text{static})} + \delta B_x. \tag{5.3}$$

Assuming that the remnant background magnetic field is larger than the neu-

romagnetic field (i.e. $B_x^{(\text{static})} \gg \delta B_x$) then

$$P_z(\omega) \propto \left(\frac{\gamma\tau}{1 + \left(\gamma\tau B_x^{(\text{static})}\right)^2} \right) B_x^{(\text{static})} + \left(\frac{\gamma\tau}{1 + \left(\gamma\tau B_x^{(\text{static})}\right)^2} \right) \delta B_x. \tag{5.4}$$

Here, the first term relates to the sensor response to the changing static field (i.e. the movement artefact) and the second term corresponds to the sensor response to neuromagnetic field changes. Importantly, the effective gain, G, of the output due to the neuromagnetic field, which can be written as

$$G = \frac{\gamma\tau}{1 + \left(\gamma\tau B_x^{(\text{static})}\right)^2}, \tag{5.5}$$

is sensitive to the static field component, $B_x^{(\text{static})}$. The gain is largest when $B_x^{(\text{static})} = 0$, and if the sensor moves, and the background field magnitude increases, the gain will drop, making the sensor less sensitive to neuromagnetic fields.

To measure the magnitude of this effect, 6 OPM sensors were placed inside the field-nulling coil, oriented with their long axes parallel to the field produced by the bi-planar B_z-coil. The background field was nulled as in normal operation. To simulate a neuromagnetic field, small oscillating currents were applied to each of the sensors at known frequencies (131, 137, 139, 141, 143 and 145 Hz) using the on-board coils. To simulate a changing background field, rather than moving the sensors, the current through the B_z-coil was varied, changing the background field approximately from –1.5 nT to +1.5 nT in 9 sequential steps. This resulted in 9 data segments, in which the small oscillating field could be measured in the presence of 9 known background fields. We then plotted the amplitude of the simulated neuromagnetic field against the background field.

Figure 5.3a shows example data from a single sensor: the effect of stepping

the background field can be seen clearly, and the inset plot shows a few cycles of the 137-Hz oscillating field which mimics neuromagnetic activity. Figure 5.3b shows power spectra of each of the 9 data segments independently, for the same sensor. In the inset graph, note that the magnitude of the 137-Hz peak changes depending on which data segment is studied. Finally, Figure 5.3c shows the fractional change of the oscillating field amplitude as a function of background field. The red line shows a fitted Lorentzian curve (showing that our data agree with the analytical analysis above (Equation 5.5)). Error bars show standard deviation over the six sensors. Over the $\pm$1.5-nT range, the gain changes by $\sim$4%.

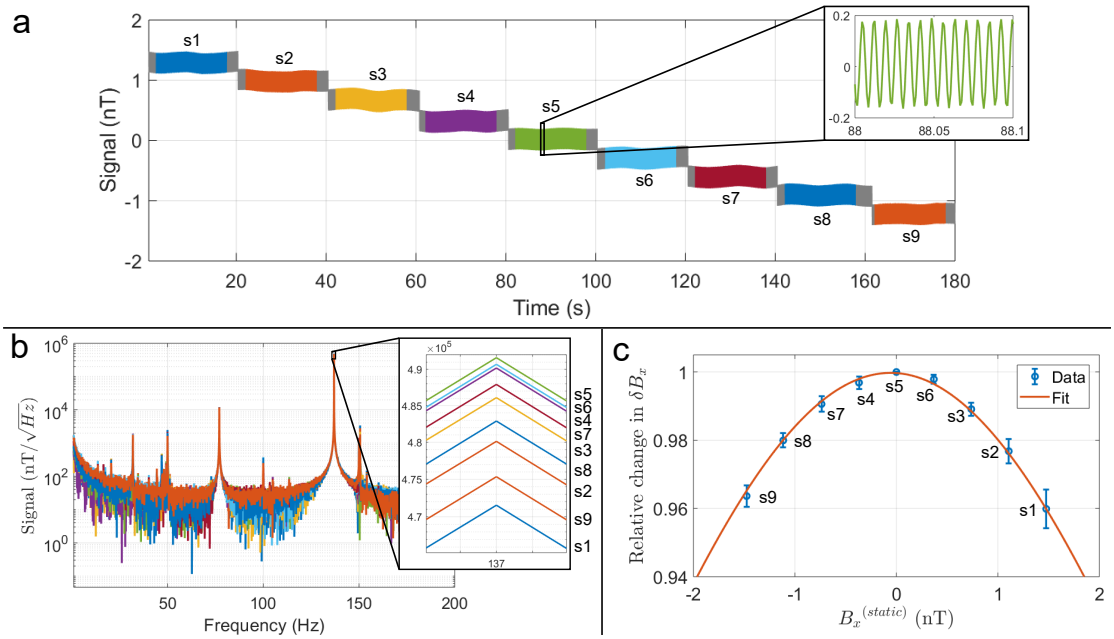


Figure 5.3: **Gain changes with static magnetic fields.** a) Raw OPM-MEG data recorded from a single channel during the gain experiment. The 9 colour-coded segments correspond to 9 different static background magnetic fields. The inset plot shows the small oscillating field, applied (in this sensor) at 137 Hz. b) Fourier transforms of each data segment. The inset figure shows the height of the 137-Hz peak for different segments. c) Fractional change as a function of background field. The blue circles show the measured data with the standard deviation over the six sensors. The red line shows a fitted Lorentzian function.

Importantly, measurement of the standard deviation of the static field was estimated to be around 0.25 $\pm$ 0.2 nT, when the subject was moving and 0.12 $\pm$ 0.04 nT when the subject was stationary. This means that, approximately,

95% of our data will experience a gain error of less than 0.5%. For the purposes of our proof-of-principle demonstration, this error was considered acceptable. However, future system modification could take this changing gain into account in data modelling.

5.2.4 Crosstalk[2]

A potential concern in the operation of an OPM scalp sensor array is that nearby OPMs may interfere with each other. Specifically, the oscillating modulation field is applied with the same amplitude, frequency and phase at all sensors. If two sensors, A and B (see Figure 5.4a) are placed in close proximity, the cell in sensor A will not only see its own modulation field, but also that of sensor B. These two modulation fields will interfere, meaning that both the gain and sensitive orientation of sensor A may be modulated simply by the presence of sensor B, and vice versa. Using both simulations and experiments, we attempted to examine the magnitude of this effect.

The known geometry of the on-board sensor coils (i.e. the coils that generate the modulation field) was used to produce a physically accurate discrete element model ($N = 360$ current elements) of each coil. The Biot-Savart law was used to calculate the magnetic field, at each sensor location, from each current element, and the fields from all elements were summed. In the present OPM array, we only measured neuromagnetic field components radial to the head – therefore only the radial coils were used for modulation and simulations consider this arrangement. The coil currents were set to an arbitrary constant value (0.35 μA giving a 200-pT field in the centre of the cell on which the coil was mounted). Using a 3D digital model of the scanner-cast, the locations and orientations of the sensor slots were determined, and the location of the sensor cell was taken to be the centre of the $3\times3\times3$-mm^3 cell which was assumed to have a stand-

[2]Work in this section was undertaken by Gillian Roberts. A brief summary is included here for completeness.

off distance of 6 mm from the end of the sensor casing (and the scalp surface). Sensors were simulated at all 13 slots in the scanner-cast.

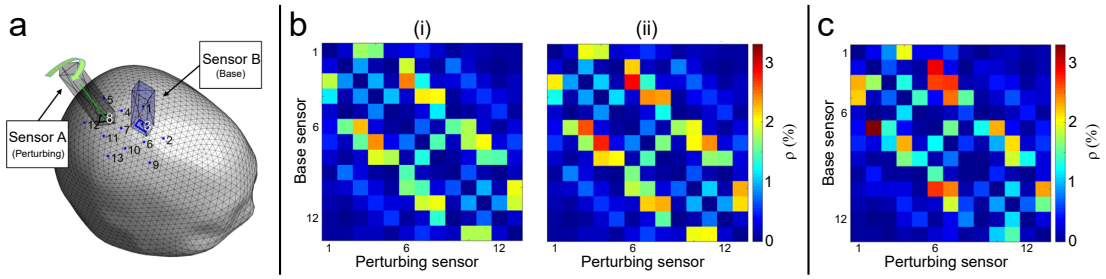


Figure 5.4: **Crosstalk characterisation across an OPM array.** a) Schematic 3D representation of the crosstalk simulation. The head surface is shown alongside two example sensors. The locations of all 13 sensors are also indicated. b) Simulated crosstalk between sensors measured as the ratio of fields (in percentage) generated by the perturbing sensor and the base sensor at the position of the base sensor. This ratio is a periodic function of sensor rotation about the radial orientation, the minimum interaction is shown in (i), the maximum is shown in (ii). c) Experimentally measured crosstalk matrix.

For every sensor pair in the array, we computed the relative field strength of the perturbing sensor (A) to the base sensor (B): i.e. if the field from coils in sensor A in cell B is $\mathbf{B}_{\text{perturb}}(\mathbf{r})$, and the field from coils in sensor B in cell B is $\mathbf{B}_{\text{base}}(\mathbf{r})$, we computed

$$\rho(\mathbf{r}) = \frac{|\mathbf{B}_{\text{perturb}}(\mathbf{r})|}{|\mathbf{B}_{\text{base}}(\mathbf{r})|} \tag{5.6}$$

Here, $\mathbf{r}$ represents the location of the base sensor cell. These strengths of interaction were used to generate a 13×13 matrix which offers a complete characterisation of crosstalk across the 13 sensor array.

It is noteworthy that the ratio is a periodic function, with respect to rotation of the perturbing sensor about its radial axis (i.e. rotation marked by the green arrow in Figure 5.4a). For this reason both the minimum and maximum values of this function were computed and plotted as two separate crosstalk matrices. Simulation results are given in Figure 5.4b, which shows the minimum (i) and maximum (ii) sensor interaction. Crosstalk, as would be expected, is largely a function of sensor proximity, with adjacent sensors demonstrating the largest effects.

Figure 5.4c shows the experimental results: the scanner-cast was set up with 13 sensors but with no subject present. Each sensor has a continuous calibration setting, which outputs a current through its radially-oriented coil, producing a sinusoidal field of amplitude 0.5 nT and frequency 130–150 Hz. By turning on the continuous calibration on each sensor sequentially, and taking a 2-minute recording of magnetic fields from all sensors, peaks in the power spectral density of all of the sensors were generated corresponding to the strength of the stray field from the perturbing sensor. By dividing the maximum height of the stray field peaks by the height of the peak of the sensor producing the varying field, we enabled estimation of the relative strength of crosstalk, as a measure directly comparable to that in Equation 5.6. The experimental results agree with those obtained through simulation, concluding that, in the present array, the maximum crosstalk between sensors is around 3%. For the purposes of the present demonstration, this small change was deemed acceptable and was therefore ignored in the measurements presented in this chapter.

5.2.5 Motion tracking[3]

To quantify head movement, we used a simple optical tracking system based upon a Microsoft Kinect V1-2010 camera (Figure 5.5a) which was placed $\sim$1 m in front of the subject. This camera provides a simultaneous 8-bit RGB video stream (640$\times$480 pixel display, with 57° horizontal and 43° vertical field of view) and an 11-bit depth image, reconstructed from an infrared projected field. Data from both streams were captured using the MatLab image acquisition toolbox, at 12 frames per second.

A motion-tracking algorithm was used to track the positions of three black dots on the outer surface of the white scanner-cast (Figure 5.5b). The algorithm was initiated via manual selection of the three dots in the first frame of the video.

[3]Work in this section was undertaken by Gillian Roberts. A brief summary is included here for completeness.

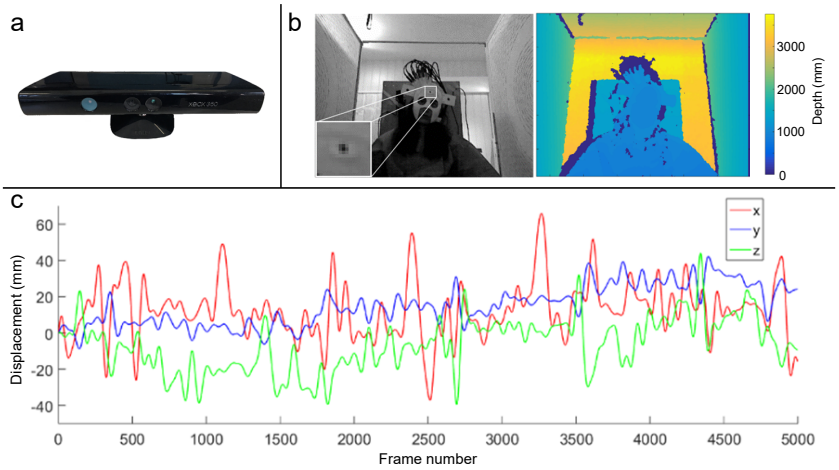


Figure 5.5: **Motion tracking using an Xbox Kinect camera.** a) The camera. b) Example data from the video stream (left) and the depth field (right). c) Example data showing the movement of one dot (zoomed-in on (b)) during a typical run with head movement.

A threshold detect routine then identified the dots and their centre of mass in all subsequent frames. Pixel numbers were converted to absolute locations in three dimensions by integrating the video data with the depth field. In this way, we defined parameters describing the motion of the three markers throughout the experiment. To quantify motion, movement parameters for all three orientations and all three fiducial locations were concatenated.

5.3 Methods

5.3.1 Data acquisition

As a first demonstration of the system, we measured electrophysiological activity in the sensorimotor cortex. A single subject (female, age 27, right-handed) performed two different tasks.

Finger abduction paradigm

The subject performed a visually-cued abduction of their left index finger, a task that robustly elicits a reduction of endogenous beta band (13–30 Hz) oscillations during movement and a rebound (increase above baseline) following movement cessation (Pfurtscheller and Lopes Da Silva, 1999). This simple task has been applied widely, with beta modulation being used as a marker of brain plasticity (Gaetz et al., 2010; Mary et al., 2015), psychosis (Robson et al., 2016; Uhlhaas and Singer, 2010) and white matter degradation (Barratt et al., 2017). A single experiment comprised 50 trials, each involving 1 s of finger abduction and 3 s of rest. 50 'dummy' trials (where the subject did nothing) were interleaved to allow an estimate of baseline activity. A subject undertook the experiment 12 times: 6 where they kept as still as possible and 6 where they made natural head movements, including nodding and shaking, stretching and drinking. Head motion was measured as explained in Section 5.2.5 - **Motion tracking**. We also undertook the same experiment using a cryogenic MEG system (CTF MEG at the Sir Peter Mansfield Imaging Centre).

Ball game paradigm

The same single subject was seated in the OPM-MEG system and asked to play a simple ball game in which they continually bounced a table tennis ball on a bat. 10-s bursts of "ping-pong" were interspersed with 10 s of baseline activity (during which the subject was told to simply hold the bat and ball on their knee). This gave a total trial length of 20 s, and the subject repeated this 29 times. Due to the location of the OPM sensors in the scanner-cast, the experiment was undertaken with the subject's non-dominant hand. Trials were cued by a second experimenter who was positioned inside the MSR throughout the experiment and gave verbal instructions to cue the game (they shouted either "ping-pong" or "rest" to begin or stop the game). This experiment was undertaken once in

the OPM-MEG system. Note that the purpose of this experiment was to elicit measurable brain activity in the motor cortex (i.e. due to controlling the bat) whilst the head was in motion (i.e. the head necessarily moves during the task).

5.3.2 Data collection

Data collection using the OPM system was as described above, with data digitised at a sample rate of 1,000 Hz. Co-registration between the brain anatomy and the sensor geometry was enabled simply by the digital representation of the scanner-cast. The orientation of the measurement itself was assumed to be parallel to the sensor slot.

To compare OPM-MEG to cryogenic-MEG recordings, we undertook the finger abduction experiment, in the same subject, using a 275-channel CTF MEG system operating in third-order synthetic gradiometer configuration (Vrba and Robinson, 2001). Data were acquired at a sampling frequency of 600 Hz, and the subject was seated. Three electromagnetic position indicator coils were placed on the head as fiducial markers (at the nasion, left pre-auricular and right pre-auricular points). The locations of these fiducials were tracked continuously during the recording by sequentially energising each coil and performing a magnetic dipole fit to these data. This allowed both continuous assessment of head movement throughout the measurement, and knowledge of the location of the head relative to the MEG sensors. Prior to the MEG recording, a 3D digitisation of the subject's head shape, relative to the fiducial markers, was acquired using a 3D digitiser (Polhemus Inc., VT, USA). Co-registration of the MEG sensor geometry to the subject's anatomical MRI was achieved by fitting the digitised head surface to the equivalent head surface extracted from the anatomical image. The subject undertook the experiment six times, and a different head digitisation was acquired each time.

5.3.3 Data analysis

Interference rejection

Following data collection, OPM-MEG data were processed in order to remove magnetic interference. The reference array sensors were located close enough to the scalp array to capture largely the same environmental magnetic interference, but sufficiently far away to be insensitive to the neuromagnetic fields of interest. This meant that the scalp and reference arrays could be used to synthesise a "gradiometer" measurement whereby the scalp array data are de-noised via regression of the reference array signals. The reference array data from all four channels were combined in a single (design) matrix and a regression was used to remove any linear combination of reference array (interference) signals from the scalp array (neuromagnetic) signals. This correction was applied to the raw (i.e. unfiltered) data.

Beamforming

Following interference rejection, all data (OPM and cryogenic) were processed in the same way. Data were inspected visually and those trials with excessive interference were discarded. Then, a beamformer adaptive spatial filtering approach was employed, as per Equations 1.22 – 1.24, but with the regularised weights equation:

$$\mathbf{w}_{\boldsymbol{\theta}}^{T} = \frac{\mathbf{l}_{\boldsymbol{\theta}}^{T}\left\{\mathbf{C}+\mu\boldsymbol{\Sigma}\right\}^{-1}}{\mathbf{l}_{\boldsymbol{\theta}}^{T}\left\{\mathbf{C}+\mu\boldsymbol{\Sigma}\right\}^{-1}\mathbf{l}_{\boldsymbol{\theta}}}. \tag{5.7}$$

In order to derive images showing the spatial signature of electrical responses, we used a pseudo-T-statistical ($\mathfrak{T}$) approach where:

$$\mathfrak{T} = \frac{\mathbf{w}_{\boldsymbol{\theta}}^{T}\mathbf{C}_{a}\mathbf{w}_{\boldsymbol{\theta}} - \mathbf{w}_{\boldsymbol{\theta}}^{T}\mathbf{C}_{c}\mathbf{w}_{\boldsymbol{\theta}}}{2\mathbf{w}_{\boldsymbol{\theta}}^{T}\mathbf{C}_{c}\mathbf{w}_{\boldsymbol{\theta}}}. \tag{5.8}$$

Note here that $\mathbf{C}_a$ and $\mathbf{C}_c$ represent data covariance in an 'active' and 'control' windows, respectively. Pseudo-T-statistics were computed at the vertices of a regular 4-mm grid spanning the entire brain. Unlike in Chapter 3, where in the simulations the dipole orientation was taken to be perpendicular to the cortical surface, here, orientation was unknown and so was estimated for each voxel, based on a non-linear search for the orientation that gave the maximum SNR (Robinson and Vrba, 1999). The beamformer was used to investigate both induced and evoked responses:

- **Induced response.** In both the finger abduction and ball game datasets, modulations in the beta band (13–30 Hz) were examined. Equation 1.24 was resolved with covariance matrix $\mathbf{C}$ computed using data filtered to the beta band over a time window spanning the entire experiment (400 s in the finger abduction and 580 s in the ball game paradigm). The 'active' time window (to compute $\mathbf{C}_a$) spanned the 0 s $< t <$ 1 s window (relative to trial onset) in the case of the finger abduction paradigm, and the 1 s $< t <$ 9 s window in the case of the ball game paradigm. To construct $\mathbf{C}_c$, the 'control' window spanned the 1 s $< t <$ 2 s and 11 s $< t <$ 19 s for the finger abduction and ball game paradigms, respectively. Using Equation 5.8, Pseudo-T-statistical 3D images were obtained, showing the spatial signature of maximum change in beta power. These images were averaged across experiments (static, moving and cryogenic) in the case of the finger abduction paradigm. Note that $\mathbf{C}$ was regularised (μ changed) to maximise signal-to-interference ratio (SIR) (see below for how it was computed).

  To examine the spectro–temporal signature of electrophysiological activity at the location of peak change, a time–frequency spectrogram (TFS) was derived. The peak location/orientation, $\boldsymbol{\theta}_{\text{peak}}$, was extracted from the beamformer images (Equation 5.8), and a time course of electrophysiological activity for that location derived using Equation 1.22 (the data covari-

ance for the weights calculation (Equation 5.7) was expanded to a broad (1–150 Hz) frequency range). The resulting data were frequency filtered into 31 overlapping frequency bands, and a Hilbert transform was used to generate the amplitude envelope of oscillations within each band. These envelope time courses were then averaged across trials and experiments, and concatenated in the frequency dimension to generate a single TFS.

The same method was used (with beta-band-filtered covariance for weights calculation) to examine beta band modulations. Averaged time courses of beta modulation for the task and 'dummy' trials were generated, and a measure of SIR was computed as the variance in the beta envelope for the task trials divided by the variance in the beta envelope for the 'dummy' trials. Note that the word 'interference' is used here instead of 'noise', since data from 'dummy' trials do not represent environmental noise but "brain noise".

- **Evoked response.** In addition to neural oscillatory responses, we sought to examine the time- and phase-locked evoked responses to stimuli, i.e. the broad-band transient component of the electrophysiological response (in this case to finger movement). Here, unfortunately, movement onset depends on reaction time to the visual cue, and therefore differences in this will attenuate the averaged evoked response. Nevertheless, data were frequency filtered between 2 and 30 Hz to best capture the evoked response. To attenuate low frequency artefacts, raw data at the OPM sensor level were treated on a trial-by-trial basis, with a 10^{th}-order polynomial fitted to, and removed from each trial (and each sensor). The beamformer was applied with covariance $\mathbf{C}$ computed using unaveraged data in the 2-30 Hz band and a time window spanning the entire set of six experiments. Pseudo-T-statistical images were generated using Equation 5.8. $\mathbf{C}_a$ was defined as the covariance computed using the trial averaged data in an active window spanning 0 s $< t <$ 0.5 s relative to trial onset. $\mathbf{C}_c$ was defined

using trial averaged data with the control window set to 1.5 s $< t <$ 2 s. Electrophysiological time courses were extracted from the peak in the pseudo-T-statistical images, and averaged across both finger abduction and rest trials. The SIR was computed as the ratio of the standard deviation of the average signal in the finger abduction trials (in the 0 s $< t <$ 1 s window) to the equivalent standard deviation in the rest trials. SIR values were calculated for each of the 12 OPM experiments (6 static and 6 moving) independently.

Trial-by-trial analysis

An additional analysis was carried out on the data from the six finger abduction experiments, where the subject was asked to make naturalistic movements of their head during data acquisition. Data from the Xbox Kinect camera and OPM-MEG channels were combined to examine the effect of subject movement on beta-band response magnitude, on a trial-by-trial basis. Initially, all data (movement, trigger and OPM-MEG) were concatenated across all six experiments. Motion data were divided into trials and the maximum movement within every trial computed as the largest difference between measured fiducial marker coordinates (the maximum movement of the three different fiducials in any of the three Cartesian axes was selected). For each trial, the mean beta amplitude during the window containing the power decrease (0.4 s $< t <$ 0.9 s), and the rebound (1.05 s $< t <$ 4.0 s) was also computed. The difference between these two metrics was taken as the peak-to-peak response magnitude. We then tested for any significant correlation between response magnitude and movement.

5.3.4 Quantifying spatial resolution

To compute a measure of spatial resolution, we measured the correlation between two beamformer-reconstructed time courses as a function of the spatial

separation between them (Brookes et al., 2010). A 'seed' location was selected in sensorimotor cortex. 4,000 'test' locations, within 3 cm of the seed, were then selected randomly. Data were filtered into the beta frequency band, and the beamformer used to extract time courses of electrophysiological activity for the seed and all test locations. Pearson correlation was measured between all seed–test pairs, and correlation values were binned according to seed–test distance and averaged within each bin. 20 bins were used, spaced evenly between 0 and 3 cm meaning that 200 seed–test pairs were averaged for each bin. In order to avoid confounds associated with source orientation, all reconstructed orientations were forced to be the same as that of the seed. To estimate spatial specificity of the system, we computed the average seed–test distance for which shared variance between reconstructed time courses fell to $<50\%$ – this metric serves as a quantification of spatial resolution, as shown in Section 3.2.4 - **Spatial resolution** in Chapter 3. This measurement was made independently for the 18 separate experiments (6 static OPM, 6 moving OPM and 6 cryogenic MEG). Spatial resolution was averaged for each experimental condition and we tested for differences between conditions using a non-parametric Wilcoxon rank-sum test.

5.4 Results

5.4.1 Finger abduction paradigm

Induced response

Results of the finger abduction paradigm for the three conditions are shown in Figure 5.6. Figure 5.6a contains results from when the subject remained still and Figure 5.6b when the subject moved. In Figure 5.6c, the cryogenic MEG results are shown. Panel (i) contains the subject motion data: histograms show

the movement of all three orientations and all three fiducial locations, on a logarithmic scale. The insets show the change in marker positions over an example experiment, where the colours represent movement in three Cartesian axes of the three markers. In the static case, subject movement was less than ± 1 cm whereas in the moving case it exceeded ± 10 cm. The subject moved less than ± 2 mm in the cryogenic system, which is a requisite for getting reliable data. Panel (ii) shows an image of change in beta power overlaid (in pink) onto axial, sagittal and coronal slices of the subject's anatomical MRI. Panel (iii) shows a TFS of oscillatory change, where blue indicates a loss in oscillatory amplitude relative to baseline and yellow indicates an increase. Line-plots of beta amplitude are shown inset. In all cases, the results are averaged over trials and experiments and the shaded region shows standard error over six experiments. OPM-MEG performed consistently across experiments with the characteristic beta decrease and post-movement rebound delineated clearly, and localised to sensorimotor cortex. SIR ranged from 4.3 to 8.2 for static OPM measures, 4.2 to 5.8 for moving OPM, and 4.9 to 7.9 for the cryogenic system. Despite an order-of-magnitude increase in head movement, there was no significant difference in SIR between the moving and static runs ($p = 0.39$; two-sided Wilcoxon rank-sum test).

Evoked response

Results from the evoked-response analysis are shown in Figure 5.7: experiments where the subject was asked to remain still are shown in Figure 5.7a and experiments where the subject was asked to make natural head movements whilst performing the finger abductions are shown in Figure 5.7b. In both cases, panel (i) shows the beamformer image and panel (ii) shows the evoked-response time courses. The functional image shows the spatial signature of the 2–30-Hz component of the evoked response, overlaid onto axial, sagittal and coronal slices of the subject's anatomical MRI. Figure 5.7c shows a direct comparison of the evoked response to finger abduction for static (blue) and moving (yellow) data.

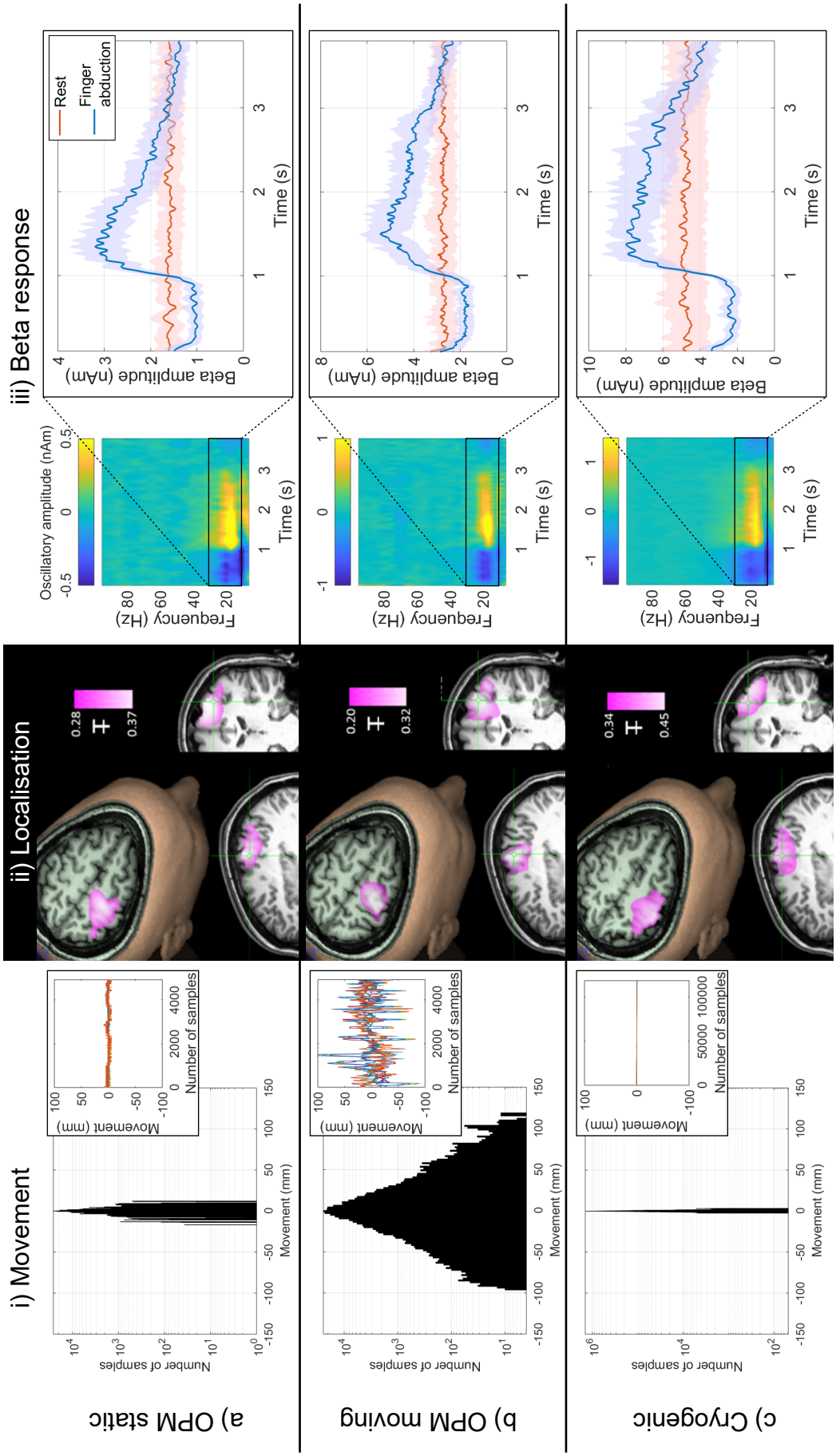


Figure 5.6: **Induced response results.** a) OPM static, b) OPM moving, c) Cryogenic MEG. In all 3 panels: i) Histogram showing movement of 3 fiducial markers on the subject's head. The inset graph shows the change in marker positions over a typical experiment; different colours show movement in 3 Cartesian axes of the three markers. ii) The change in beta-band power due to finger abduction (pink). iii) TFS depicting changes in neural oscillations during finger abduction. The inset graph shows the characteristic beta-band response for finger abduction (blue) and rest trials (red).

Importantly, the spatio-temporal signature of the response in the two cases is largely similar. Quantitatively, for the static case, SIR ranged from 1.4 to 2.1, whilst for the moving case SIR ranged from 1.0 to 1.9; no significant difference was observed ($p = 0.24$; two-sided Wilcoxon rank-sum test).

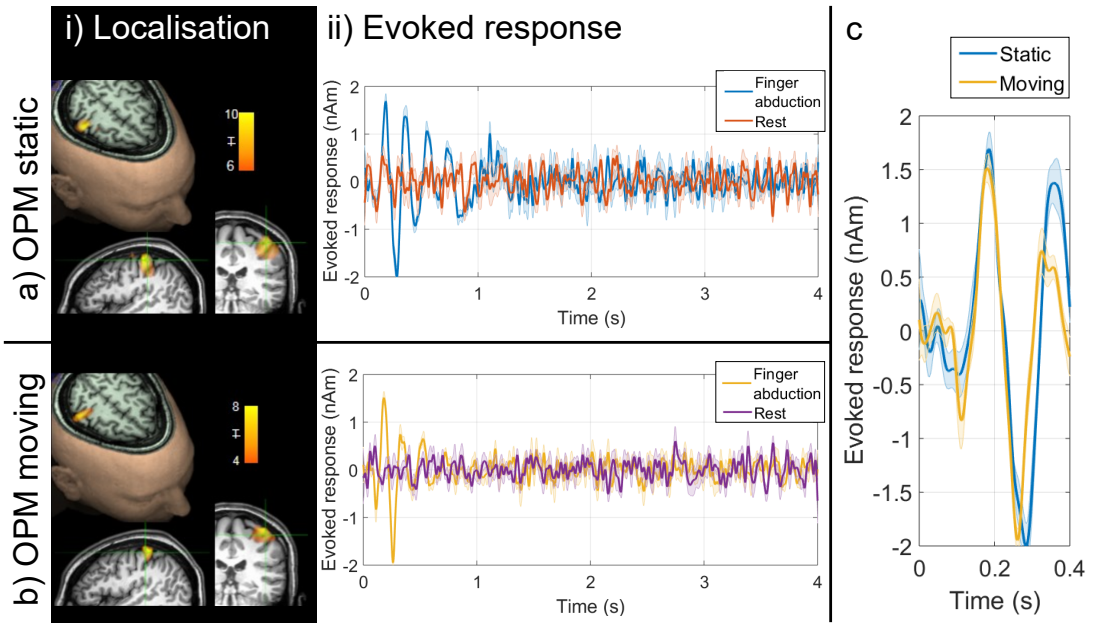


Figure 5.7: **Evoked response results.** a) OPM static, b) OPM moving. On both: (i) beamformer image overlaid onto the subject's MRI, (ii) time courses of the evoked response for the finger abduction trials (blue/yellow) and rest trials (red/purple). The shaded area shows standard error across 6 experiments. c) Direct comparison of the evoked response in the case where the subject was asked to remain still (blue) and was moving (yellow).

Trial-by-trial analysis

Figure 5.8a shows beta envelopes (for both the finger abduction and the rest trials) in the presence of large (50% of trials with highest movement) and small (50% of trials with smallest movement) motion. Here, the yellow trace shows the beta-band amplitude in finger abduction trials in the presence of (on average) a 4.3-cm within-trial head movement; the blue trace shows a similar plot for data recorded in the presence of a 1.7-cm movement. The purple and red traces show the case for resting trials with 4.4-cm and 1.7-cm movements, respectively. There was a significant increase in baseline beta-band oscillatory amplitude for the larger head movement, in both the resting and finger abduction trials. This

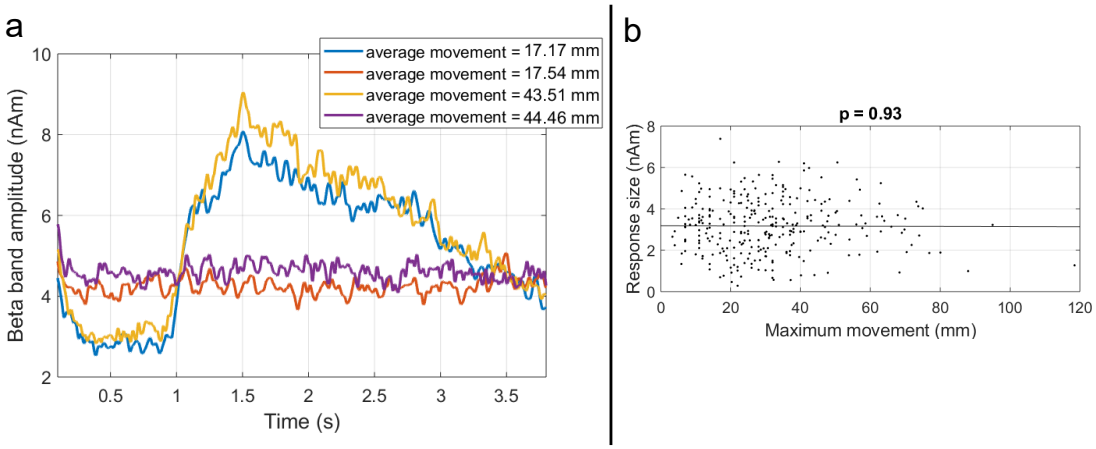


Figure 5.8: **Response magnitude as a function of subject movement**. a) Beta envelopes for finger abduction trials (blue/yellow) and resting trials (red/purple) in the presence of large (yellow/purple) and small (blue/red) movements. b) Response size as a function of maximum movement during a trial.

was thought to relate to an increase in artefact due to electrophysiological activity in the muscles in the neck. However, despite a more than doubling of the head movement, the actual beta response magnitude to finger abduction remains similar. To quantify this, Figure 5.8b shows the measured peak-to-peak response amplitude plotted against motion for all trials. No measurable relationship between movement and beta response magnitude was observed, showing that data quality was unaffected by movement.

5.4.2 Ball game paradigm

Results of the ball game paradigm are shown in Figure 5.9. Panel (a) shows a photograph of the subject *in-situ* bouncing a table tennis ball off a bat. On panel (b) the change in beta-band power is overlaid in pink onto the three anatomical MRI slices. Panel (c) shows a TFS (averaged over the 29 trials) of the oscillatory modulation at the peak location, where again, blue indicates a loss in oscillatory amplitude and yellow indicates an increase in amplitude above baseline. A lineplot of the beta-band modulation is shown inset. A decrease in amplitude during the first 10 s, corresponding to when the subject was bouncing the ball, followed by an increase in amplitude and return to baseline can be seen clearly.

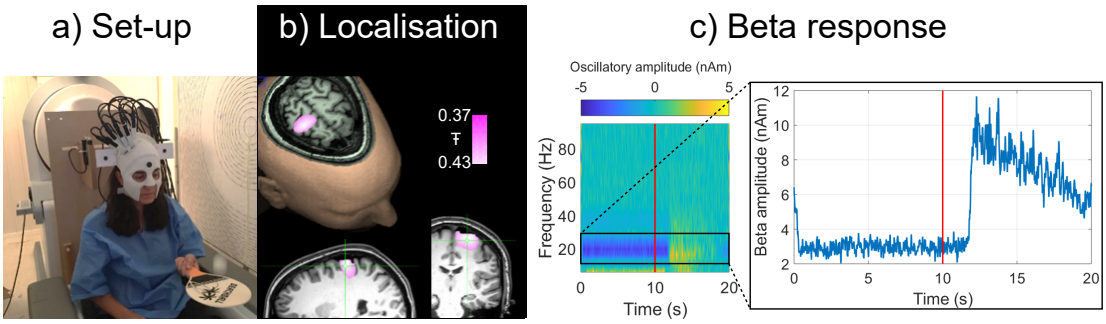


Figure 5.9: **Ball game results**. a) Experimental set-up: the seated subject bouncing a table tennis ball. b) Spatial signature of beta-band oscillatory change during periods of playing the ball game compared to rest. c) Trial averaged TFS (left) and amplitude of beta oscillations averaged over time (right).

When looking at the 3D images of source localisation for both paradigms (panel (ii) on Figure 5.6 for the finger abduction and panel (b) on Figure 5.9 for the ball game task), one can spot a slight shift in peak location. Figure 5.10a contains the sagittal slices for each of the paradigms and on Figure 5.10b a schematic of the homunculus's motor strip is shown. As shown, the areas of the cortex responsible for arm/wrist movements are slightly superior on the strip than those associated with finger movements. It can be seen on panel (a) that the peak location for the ball game task is higher than that of the finger abduction paradigm.

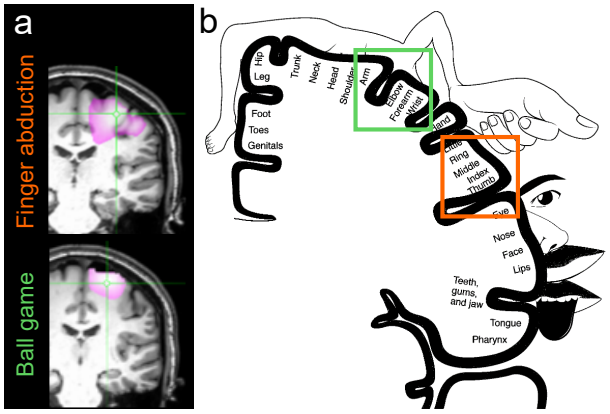


Figure 5.10: **Comparison of source localisation between the two paradigms.** a) Coronal slices showing the peak locations from the finger abduction (top) and the ball game paradigm (bottom). b) Schematic representation of the homunculus's motor strip. Green square located around the arm area, orange square over the hand area. Figure b) adapted from Wikipedia.

5.4.3 Spatial resolution

The spatial resolution measurements are shown in Figure 5.11. Panel a) shows three slices of the anatomical MRI where an example 'seed' is represented by the

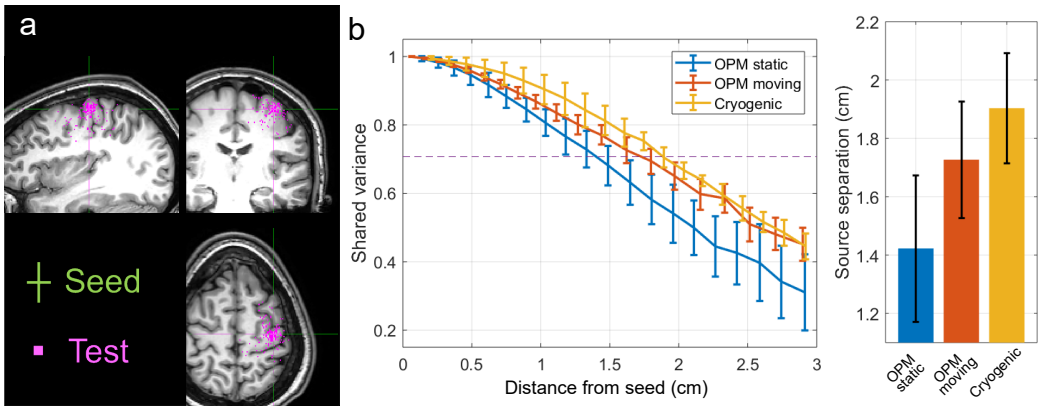


Figure 5.11: **Spatial resolution results.** a) Sagittal, coronal and axial slices from the anatomical MRI, containing an example 'seed' location at the green cross-hairs over the somatosensory cortex and 4,000 'test' locations plotted as pink squares. b) Lines show correlation between the seed and test time courses plotted as a function of spatial separation. Blue is for the OPM static, green for the OPM moving and orange for the cryogenic system. The bar chart shows the source separation (in cm) at which shared variance dropped to less than 50%. Error bars show standard deviation over test locations.

cross-hairs and the 4,000 'test' locations are plotted in pink squares. In panel b), the line graph shows correlation between the seed and test time courses plotted as a function of separation between them. The bar chart shows source separation for which shared variance dropped to $< 50\%$. In both cases, results are shown for the three different experimental conditions and error bars show standard deviation over six experiments. The highest spatial resolution was achieved in the static OPM case. Spatial resolution dropped (although not significantly ($p = 0.09$)) when the subject made naturalistic head movements. This is a consequence of the beamformer and is a well characterised effect (Brookes et al., 2010): the limited degrees of freedom in the MEG data mean that spatial resolution drops if the beamformer is forced to suppress artefacts. Here, artefacts were generated by the muscles in the neck controlling head movement – in nulling these artefacts, the spatial resolution would be expected to decrease slightly. Spatial resolution was lowest for the cryogenic system. The difference in spatial resolution between static OPMs and the cryogenic system was significant ($p = 0.002$). The difference between OPMs with movement and the cryogenic system was not significant ($p = 0.09$).

5.5 Discussion

In this chapter, the construction of a prototype multi-channel MEG system based on OPMs, that can be worn like a helmet, has been described. Along with some of the principal challenges underlying its fabrication. Distinct from Chapter 4, this OPM-MEG prototype system does not rely on the CTF DAQ system, making it an independent MEG device. The central core of the system is 13 OPM sensors held in a scanner-cast. The use of a subject specific 3D-printed scanner-cast has again demonstrated that the accurate and rigid placement of the sensors relative to the brain anatomy is possible. The difference here, however (relative to Chapter 4), is that subject movement was not restricted: indeed they were allowed to make natural head movements while being scanned, and results of source localisation and SIR calculations showed no loss of data quality when compared to a current state-of-the-art SQUID-based MEG system. This natural movement was made possible by the design and fabrication of a novel set of nulling coils that reduced the background magnetic field allowing the OPMs to remain operational even in the presence of movement. An example of a naturalistic paradigm has also been shown, where a subject played a ball game, something incompatible with current SQUID-based MEG technology. While simple, this demonstration paves the way for a new generation of neuroscience experiments, yet to be explored, e.g. motor learning tasks or hand-eye coordination.

5.5.1 Signal-to-interference

The SIR measurements were approximately the same in all three conditions, regardless of the subject movement. This was the case for both the induced and the evoked responses. However, it is worth mentioning that the work undertaken here has focused on relatively high frequency (13–30 Hz) responses. We speculate that, if one were to look at lower frequency bands like alpha or theta, slow (i.e. low frequencies) changes in field related to movement of sensors in

the remnant field (after nulling), would become more challenging to eliminate. One possible solution would be to use the motion-tracking system to regress out the movement parameters: indeed in a recent work, Holmes et al. (2018) used an OptiTrack V120:Duo camera system (NaturalPoint Inc., Corvallis, OR, USA) to regress out 6 movement parameters (3 translation and 3 rotation) from OPM-MEG data, showing a significant decrease in the movement artefact. Another plausible solution could make use of further reference sensors which moved with the subject but were located distal to the head. Overall, whilst here we show that beta activity in the presence of movement is unaffected, lower frequencies should be a topic of future work.

5.5.2 Spatial resolution

The spatial resolution measurements employed in this chapter were simple (and similar to those described in Section 3.2.4 - **Spatial resolution**). Nevertheless they show that only 13 OPMs can compete with a current state-of-the-art MEG device consisting of 275 sensors in terms of measurable spatial specificity. These measurements tell us about how signal falls off around a large source, and this represents a useful measure of e.g. full width at half maximum of a peak. However, this does not represent "true" spatial resolution. A genuine metric for spatial resolution comes from the ability to separate two regions in close proximity generating temporally independent source time courses (e.g. Chapter 3 Figure 3.7). In order to have a better quantification of spatial resolution, different experiments should therefore be performed. For example somatotopic/retinotopic mapping of the sensorimotor/visual cortex could exploit the known organisation of primary cortices to generate spatially separate but independent sources, which we could then try to map using an OPM array (Barratt et al., 2018). As seen from simulations, bringing MEG sensors closer to the scalp means that the spatial patterns of the magnetic fields have a more focal topology than those of

cryogenic sensors which are necessarily further away. As a consequence, higher spatial harmonics exist for OPM-MEG and therefore source separation should be improved (assuming sufficient sensor density on the scalp). This should be a topic of further work.

5.5.3 Wearable technology

The OPM-based MEG device described in this chapter affords a demonstration of the potential of this technology to become a wearable neuroimaging tool, as opposed to the restrictive MEG devices available to date. This means that MEG has now the potential to compete with other wearable neuroimaging tools such as EEG and fNIRS. In principle, OPM-MEG could outperform both of these technologies: e.g. fNIRS has temporal resolution limited by the latency and longevity of the BOLD (blood oxygenated level dependent) response whilst EEG has limited spatial resolution. However, a principled comparison between technologies is a topic for future work.

5.6 Conclusions

In this chapter, the construction of an OPM-based MEG device to measure reliable electrophysiological data while a subject moves freely, has been described. It has been shown that wearable OPM-MEG can be used to collect electrophysiological data, with no loss of quality even when the subject moves. Performance of the OPM system is comparable to a 275-channel cryogenic MEG system in terms of signal-to-interference ratio and spatial resolution. A simple naturalistic paradigm has also been demonstrated, showing the potential of our OPM-MEG prototype. These findings open up a wealth of new paradigms and subject groups for investigation, potentially changing the scope of the neuroscientific experiments possible with MEG.

Chapter 6

Comparison with EEG

In this final experimental chapter, a comparison between EEG and OPM-MEG is described. The effect of subject movement and task-correlated muscle artefacts on both modalities are explored. We show that these complementary wearable neuroimaging techniques produce similar results when the subject is stationary, but EEG data are highly compromised by artefacts generated by electrical activity in the muscles when the subject moves.
The work presented here was published in Nature in 2018 (Boto et al., 2018).

6.1 Introduction

The OPM-based MEG device reported in the previous chapter opens up the possibility of a new type of wearable functional neuroimaging technique: a MEG device which can be worn like a helmet and which could compete with current portable neuroimaging tools like functional near-infrared spectroscopy (fNIRS) and electroencephalography (EEG):

fNIRS (Ferrari and Quaresima, 2012) is a portable, non-invasive, optical imaging tool that provides an indirect measure of brain function by detecting changes in haemoglobin concentrations within the brain. Such changes are related to and triggered by neural activity. They can be measured by means of the characteristic absorption spectra of haemoglobin in the near-infrared range. In

modern fNIRS systems, a number of detectors (optodes), ranging from tens to hundreds, are mounted in a flexible cap, making fNIRS a wearable brain imaging system. It is an attractive tool which is widely used in a broad range of applications, with neurodevelopment being one of the largest growth areas. However, the relatively poor temporal resolution and indirect nature of the measurements led us to conclude that fNIRS is not in direct competition with OPM-MEG.

EEG works by measuring the electrical potentials generated at the scalp by the same underlying neural current flow that gives rise to the MEG signal (Berger, 1929). It is wearable, lightweight and cheap, and is sometimes used simultaneously with conventional MEG systems. There is no reason why OPM-MEG and EEG could not be measured simultaneously, but EEG alone offers direct competition to our wearable OPM-MEG device.

The similarity between EEG and MEG, makes a comparison both possible and appealing. In this chapter, sensor-level results will therefore be compared when using the same visuo-motor task employed in Chapter 5, to assess how subject movement affects data quality. Previous publications (Zimmermann and Scharein, 2004; Claus et al., 2012; Muthukumaraswamy, 2013) have suggested a difference in the manifestation of muscle artefacts between MEG and EEG, and for this reason we aim to assess, specifically, how muscle artefacts affect both modalities.

6.2 Methods

6.2.1 System

EEG

EEG data were acquired using BrainAmp MRplus EEG amplifiers (Brain Products, Munich, Germany) with a 1,000 Hz sampling rate and a frequency range

of 0.06–250 Hz (30 dB roll-off at high frequencies). A standard 64-channel EEG cap (EasyCap, Herrsching, Germany) was fitted to the subject by an experienced EEG user, with electrode impedances maintained below 10 kΩ for the duration of the study (these were checked regularly between data recordings). The electrode layout followed the extended international 10-20 system (see Figure 6.1) with an additional channel for recording the electrocardiogram (ECG). FCz was used as the reference electrode during acquisition. All data were acquired using BrainVision Recorder software (v1.2, Brain Products, Munich, Germany).

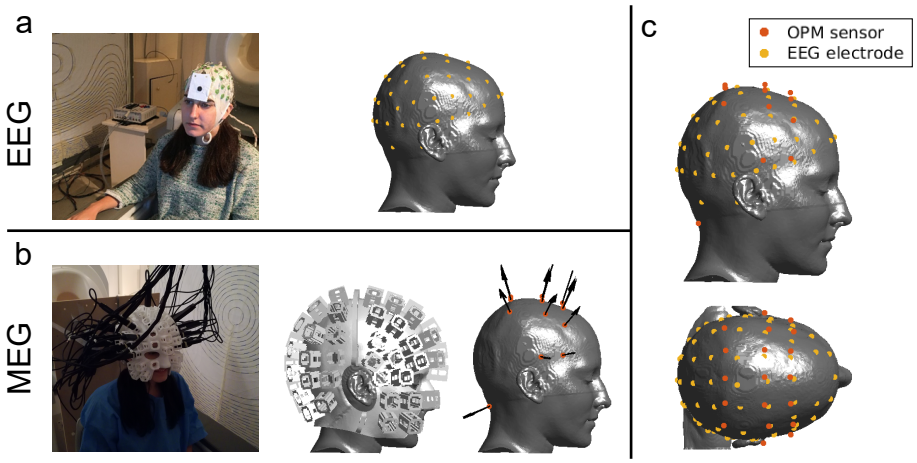


Figure 6.1: **System set-up.** a) EEG and b) MEG set-ups. The EEG cap comprises 64 channels. The 21 OPM sensors were placed in the OPM-MEG scanner-cast as shown in the figure to measure muscle artefacts. c) Both OPM sensors and EEG electrodes overlaid onto the subject's scalp.

OPM-MEG

MEG data were recorded employing the same OPM-MEG device described in the previous chapter. Further recordings were undertaken using a new scanner-cast comprising 81 slots around the whole head. This was designed and built to fit the same female subject who took part in the previous study. The scanner-cast can be seen in Figure 6.1b. A total of 25 OPM sensors were available to use: 4 were again used as reference sensors, both to measure the background fields needed for the field-nulling system and to regress out interference. The remaining 21 sensors were placed in the scanner-cast as shown in Figure 6.1b/c.

6.2.2 Data acquisition

To facilitate a comparison between EEG and OPM-MEG data, we undertook two sets of experiments:

Finger abduction paradigm

We first aimed to compare OPM-MEG data recorded during the finger abduction task (i.e. data reported in Chapter 5) to EEG. The same finger abduction experiments were therefore repeated, while EEG data were collected. Again, a single experiment comprised 50 trials, each involving 1 s of finger abduction and 3 s of rest. 50 'dummy' trials were interleaved. The subject who previously participated in the OPM-MEG study, undertook the experiment 12 times, 6 where they kept as still as possible, and 6 where they made natural head movements during the task. Head motion was again measured using the Xbox Kinect camera (as described in Section 5.2.5 - **Motion tracking**), which tracked the movement of a single head marker located on the subject's forehead (this can be seen in the photograph in Figure 6.1a). These experiments were directly equivalent to those undertaken using OPM-MEG and reported in Figure 5.6.

Muscle-tensing paradigm

We ran the same finger abduction paradigm but asked the subject to tense the muscles in their jaw and neck during the 1-s long movement period (as well as move their finger) so as to produce task-correlated muscle artefacts. Note that this represents a worst possible case scenario. This experiment was repeated twice: once with data recorded with the OPM-MEG device (21 channels, Figure 6.1), and once with data recorded using EEG.

6.2.3 Data analysis

EEG data were initially analysed in BrainVision Analyzer2 (Brain Products, Munich, Germany). For each experiment, data were visually inspected for noisy channels; only electrode Tp10 was found to be noisy (in 2 out of 13 recordings) and was excluded (in these 2 runs). Data were referenced to an average of all remaining channels to provide as clean a reference signal as possible (with minimal neuronal or artefactual signals (Mullinger et al., 2013)). Following this, data were exported to MatLab where a sensor space analysis was carried out.

For each sensor (OPM and EEG), a TFS was employed to visualise the neural oscillatory response to finger movement. Baseline oscillatory amplitude, computed in the 3 s $< t <$ 3.5 s time window, was subtracted so that the TFS showed absolute change from baseline (for a clearer comparison between both modalities). For the muscle-tensing paradigm, quantitative analysis was carried out in the 20–55 Hz frequency range: absolute change in oscillatory amplitude from baseline, in the 0.25 s $< t <$ 1 s time window (during the muscle clench), was normalised by the baseline estimate to assess fractional change in amplitude. EEG and OPM-MEG results were compared.

Beamforming

A final analysis was performed to investigate the effect of a beamformer on the reduction of muscle artefacts in OPM-MEG. To this end, data from the muscle-tensing paradigm were analysed in two ways: first, a beamformer spatial filter was employed to look at a location of interest in the right sensorimotor region. The beamformer data covariance was computed in the 10–50-Hz frequency band and using a time-window spanning the entire experiment (400 s). In this case, no regularisation was applied. Second, an overly-regularised beamformer was applied (with the regularisation parameter equal to 100 times the maximum eigenvalue in the unregularised matrix). The effect of this over-regularisation is

seen clearly in Equation 5.7, since in a case where $\mathbf{C} \ll \mu\mathbf{\Sigma}$, the equation for the beamformer weights collapses to

$$\mathbf{w}_{\boldsymbol{\theta}_{\text{reg}}}^{T} = \frac{\mathbf{l}_{\boldsymbol{\theta}}^{T}}{\mathbf{l}_{\boldsymbol{\theta}}^{T}\mathbf{l}_{\boldsymbol{\theta}}} \tag{6.1}$$

i.e. the weights become a scaled version of the lead fields, and the beamformer solution becomes analogous to a dipole fit. In both cases, a TFS was constructed from the beamformer-reconstructed signal. Finally, for comparison, a single sensor with the largest beta-band response was selected and a channel level TFS was constructed.

6.3 Results

6.3.1 Finger abduction

Figure 6.2 shows a direct comparison of EEG and OPM-MEG data recorded during the finger abduction task. For both modalities, data from a single sensor with the largest beta band fluctuation (for data recorded in the static case) have been chosen for visualisation. Movement data, recorded using the Xbox Kinect camera, are also shown as histograms. For both EEG and MEG data, and static and moving conditions, TFSs are shown from data averaged over all six experiments (300 trials, left column), and also from a single representative experiment (50 trials, right column). Both finger abduction (top) and rest trials (bottom) are shown. With the head static, OPM-MEG and EEG offer similar results at the channel level: the expected beta modulation is shown clearly, and rest trials show no obvious modulations. However, with the head freely moving, whilst OPM-MEG data show a clear response, EEG data suffer from significant artefact generated by muscle activity (as well as, potentially, movement degrading the contact of the electrode with the scalp). Whilst averaging over more trials (300

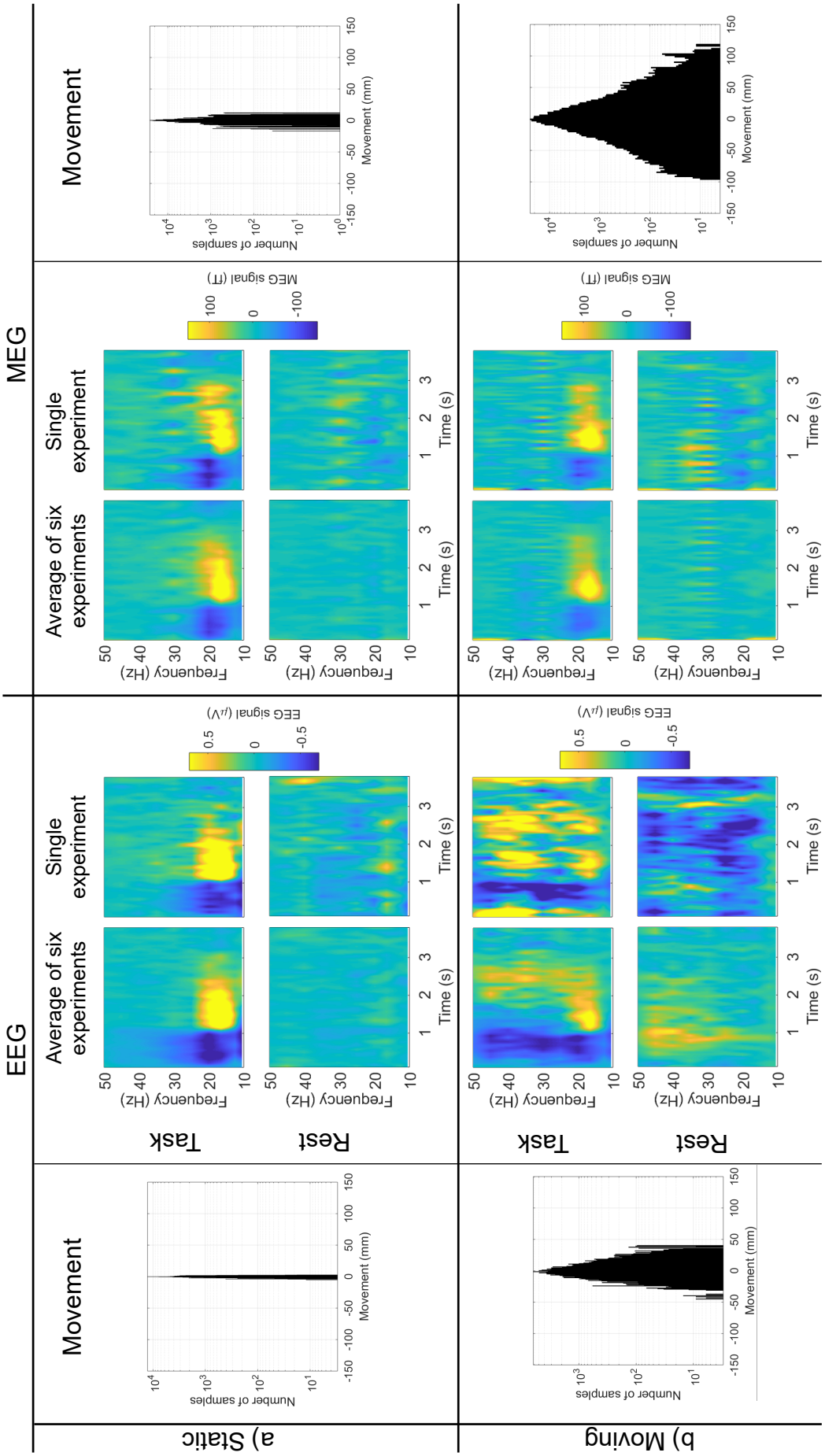


Figure 6.2: **Finger abduction results.** a) Static condition. b) Moving condition. In both panels, EEG results are shown on the left and MEG results on the right. Histograms show the movement from the single (three) tracking dot(s) located on the subject's head (scanner-cast). In both (a) and (b), TFS plots are shown for both finger abduction (top) and rest (bottom) trials. Averaged TFSs from 6 experiments (300 trials) are shown on the left while a single experiment (50 trials) is shown on the right.

compared to 50) reduces the contribution of muscle artefact to the processed EEG signal, it does not eliminate it.

6.3.2 Muscle tensing

Figure 6.3 shows results of the muscle-tensing paradigm. Panel (a) shows a visualisation of the 64-channel EEG montage using the extended 10-20 system (top) alongside the 21-channel OPM-MEG montage used to assess muscle artefacts (bottom). Panel (b) shows TFS plots extracted from three channels of interest, again for EEG (top) and OPM-MEG (bottom). Note that these channels (indicated by the yellow stars in (a)) were selected because they showed the largest beta band response to finger abduction in separate experiments (non muscle tensing). Notice that, for OPM-MEG, although a muscle artefact is observed, the beta response is still clearly visible. However, in the EEG channels, the beta response is completely obscured by the muscle artefact (this was the case in all channels). The bar chart in panel (c) shows the size of the muscle artefact (averaged across 13 sensors covering the sensorimotor strip as indicated by the red circles in (a)) relative to baseline. Note that the size of the artefact in EEG is $\sim$10 times larger than the equivalent artefact in OPM-MEG. For completeness we also measured the size of the artefact relative to the beta rebound (the only phase of the beta response still visible in the EEG data). This was done for the three (EEG and MEG) channels shown in (a): in EEG, the artefact was 32 ± 4 times larger than the rebound. In MEG, this value dropped to 3 ± 2.

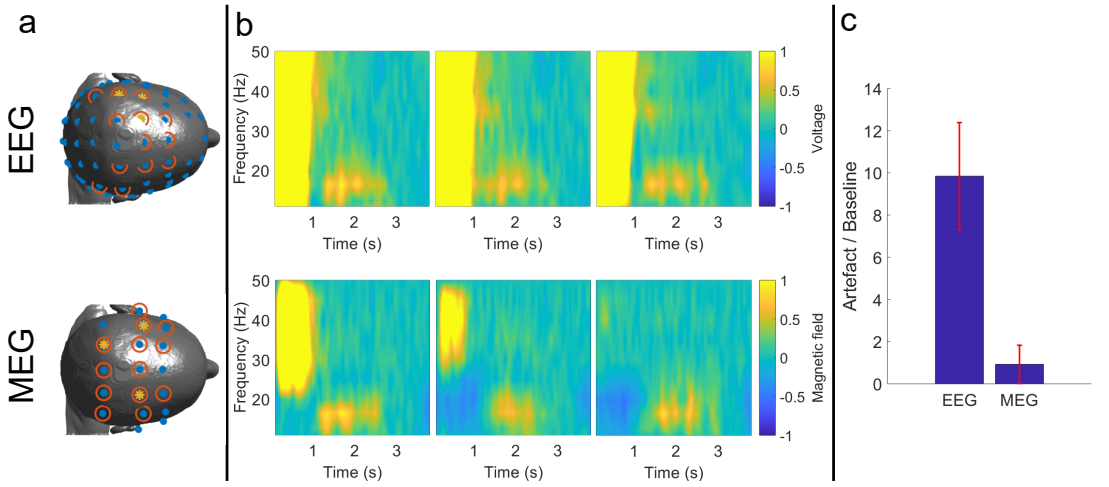


Figure 6.3: **Muscle-tensing results.** a) Channel montages for EEG (top) and OPM-MEG (bottom). Yellow stars denote channels used to create (b) and red circles show channels used to create bar chart in (c). b) TFS showing fractional change in oscillatory amplitude, relative to baseline for the 3 channels. c) Quantitative analysis of the magnitude of the muscle artefact in the 0–1-s window, and 20–55-Hz frequency range for the 13 sensors shown as red circles in (a). Error bars show standard deviation across sensors.

Effect of regularisation

Finally, we aimed to see if, using beamforming applied to OPM-MEG we could reduce/remove the muscle artefact. Results of this analysis are shown in Figure 6.4. Panel (a) shows a beamformer image, highlighting a location of interest in right sensorimotor cortex. Panel (b) shows the time–frequency response for the best OPM-MEG sensor (shown as a yellow star in the inset figure), whilst panel (c) shows equivalent time-frequency spectra, reconstructed at the location of interest identified in panel (a). The left-hand panel of (c) shows the over-regularised beamformer reconstruction and the right-hand panel shows the unregularised beamformer reconstruction. Note that a large muscle artefact, overlapping with the beta response to finger movement, is clear in the best sensor and over-regularised beamformer data. However, following beamforming, the power minimisation ensures that the artefact is effectively reduced in magnitude. This example shows that even in a "worst possible" case, where high-amplitude, task-correlated muscle artefacts contaminate the data, those artefacts are readily controlled.

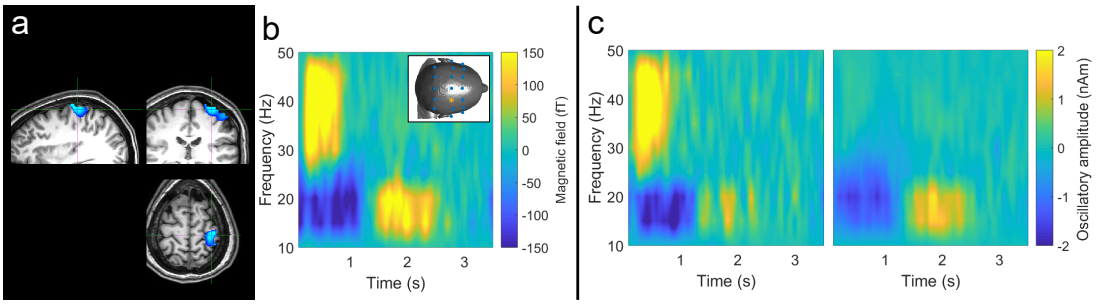


Figure 6.4: **Effect of regularisation on source localisation.** a) Beamformer image, highlighting the location of interest in right somatosensory cortex. b) TFS for the best OPM channel, marked as a yellow star in the inset. c) Reconstructed TFS responses from the over-regularised (left) and un-regularised (right) beamformer.

6.4 Discussion

The comparison between EEG and MEG provided in this chapter has been centred on the effect that muscle activity has in both modalities. With no subject movement, both EEG and MEG gave similar results, where the beta band modulation was visible in the TFS. The difference comes when the subject makes natural movements: EEG sensor level data were highly contaminated by muscle artefacts, as opposed to OPM-MEG data, which still showed a clear response. Furthermore, in the muscle-tensing paradigm, which provided a worst-case scenario with task-correlated muscle artefact, the EEG response to finger movement was completely obscured. In the OPM sensors, however, the beta modulation was again clear, and beamforming proved to be an effective technique to remove the artefact. Whilst beamforming is not the only solution to this problem, the example given in this chapter is in agreement with previous literature (Sekihara et al., 2004; Brookes et al., 2008, 2009) in showing the interference reduction, properties of spatial filtering. These results have therefore shown that EEG data, acquired in a freely moving subject, do not produce the same quality of neuronal responses as that afforded by OPM-MEG.

6.4.1 Muscle artefacts

The results above show that muscle artefacts in EEG and MEG begin in the low beta band (∼15-20 Hz) and extend into the higher (gamma) frequency range. This result is in good agreement with previous findings: for example, Whitham et al. (2007) recorded EEG data with and without neuromuscular blockade, with results showing that EEG data are contaminated at frequencies above ∼20 Hz. Our data also show that EEG is markedly more sensitive to such artefacts than MEG. Again this is not a new finding (Zimmermann and Scharein, 2004; Claus et al., 2012; Muthukumaraswamy, 2013), and it occurs because the magnetic field falls off rapidly as distance to the primary dipole generator increases, whereas volume conduction in EEG facilitates greater (and less predictable) spatial spread of the measured electrical potential.

Muscle artefacts are clearly an issue in a wearable neuroimaging system, particularly during paradigms (such as those employed in the present work) where head and face movement is either expected or task related. Given its lower sensitivity to muscle artefacts, MEG offers significant advantages in this area. Crucially however, in standard MEG systems this benefit has not been realised due to the fixed nature of cryogenic equipment and thus EEG is the current go-to modality for wearable monitoring of neuronal activity (Kranczioch et al., 2014). The primary neuroscientific applications of wearable neuroimaging technology include scanning babies and toddlers, adults with movement disorders, paradigms with free head movement (e.g. spatial navigation and 3D virtual reality). In all of these cases, muscle artefact would be a big concern. Further, clinically, a useful application of wearable neuroimaging is in epilepsy: it is widely acknowledged that the ictal discharge initiates an epileptic seizure and that the site of this discharge is an appropriate target for surgical resection, however such events are often obscured in EEG by associated muscle artefact (Hajipour Sardouie et al., 2015). It therefore follows that OPM-MEG technology, with its

reduced artefact sensitivity, offers a distinct advantage over EEG for clinical and neuroscience-focused studies.

6.4.2 Spatial resolution

Beyond muscle artefacts, there are other significant advantages to the use of OPM-MEG over EEG, with perhaps the most obvious being the increased spatial specificity. Indeed, this was eloquently highlighted in a recent review (Baillet, 2017) which explained that EEG signals are strongly affected by the substantial difference in electrical conductivity between the scalp, skull, brain, and other biological tissues. The extracranial magnetic fields are much less sensitive to these variations in tissue conductivity. Consequently, the spatial topography of MEG sensor data is less smeared and distorted than that of EEG electrical potentials produced by the same physiological sources. This contributes to a clearer interpretation of MEG sensor topography. Further, MEG has more accurate forward models (due to the low complexity of these models relative to EEG), which, in turn, improves the accuracy of inverse modelling resulting in a better spatial resolution of MEG compared to EEG.

6.4.3 Practicalities

Finally, OPM-MEG offers a number of practical benefits above and beyond EEG. EEG electrodes must be placed in electrical contact with the head – in the experiments described here, contact is maintained using a conductive gel placed between the electrode and the scalp. Use of abrasive gel is also often required to remove dead skin cells and grease from the scalp in order to limit the contact impedance of the electrode. The fact that each electrode must be treated separately in this regard makes EEG set-up time long. The process can also be uncomfortable for the subject and may not be tolerated by some subject groups. OPM-MEG set-up time on the other hand is relatively short since no electri-

cal contact is required. The requirement for electrical contact also raises other potential issues: electrical contact between electrodes via the conductive gel (bridging) is undesirable since it acts to spatially blur the measured spatial topography, but can be difficult to avoid in high-density EEG studies. This is not a problem for OPM-MEG (where sensor crosstalk can be controlled). OPM-MEG also potentially offers greater scan-to-scan consistency between experiments in the same subject. This is because whilst the sensitivity of OPMs does not change between experiments, the sensitivity of EEG is dependent on the quality of connection to the scalp (hence there exists a subject and operator dependency). It also means that long-term (12–24-hour) OPM recordings could be considered without any concerns regarding data quality (due to impedance changes). Finally, in clinical studies, OPMs, being contactless, reduce any risks of infection and for studies following surgery (for example in epilepsy) recordings could be made through bandages (which is impossible using EEG).

6.5 Conclusions

In this chapter, a comparison between EEG and OPM-MEG has been undertaken to assess the effect of movement artefacts on data quality. Both MEG and EEG showed similar results when the subject's head was stationary, however, in the moving case, while OPM-MEG data still showed a clear response, EEG suffered from significant artefact generated by muscle activity. The task-correlated muscle-tensing paradigm supported these results: in this case the beta response in EEG was completely obscured by the muscle artefact. However, this was not the case for OPM-MEG in which beta modulation was observed clearly. Quantitatively, in the 20–55-Hz frequency range, the muscle artefact showed to be 10 times worse in EEG compared to MEG. These results show clearly that EEG data, acquired in a freely moving subject, are highly compromised by muscle artefact.

Chapter 7

Concluding remarks

The work presented in this thesis represents one of the possible routes that the next generation of MEG technology might take in the coming years. The simulation work described in Chapter 3 outlined the hypothetical advantages that scalp-mounted MEG systems could have over current cryogenic devices. In Chapter 4, the use of a single OPM to experimentally measure the MEG signal was described, and the evoked response due to median nerve stimulation was compared with similar measurements made using a state-of-the-art SQUID-based MEG device. Chapter 5 described the fabrication of a scalp-mounted multi-channel OPM-MEG system, bringing field-nulling technology on board to allow the subject to move whilst being scanned. Finally Chapter 6 presented a comparison of our system with EEG, looking at the effect of movement on the data quality.

7.1 Signal-to-noise ratio

Simulations concluded that a whole-head MEG system, based on scalp-mounted sensors like OPMs, would offer around a fivefold improvement (or higher) in signal and SNR. In addition, spatial resolution could be improved by approxi-

mately an order of magnitude. The experimental results presented in Chapter 4 confirmed a fourfold improvement in signal when measuring the evoked response due to median nerve stimulation. This was the result of simply reducing the scalp-to-sensor distance, afforded by placing the OPM in the scanner-cast. However, improvement in SNR of OPMs compared to SQUIDs was only around a factor of 2. Similarly, whilst significant improvement in spatial resolution was demonstrated in Chapter 5, this improvement was not as dramatic as simulations predicted. This is a direct consequence of the higher noise floor of OPMs compared to SQUIDs and both the SNR and spatial-resolution improvements, predicted by the simulations, could be realised in the future with the development of more sensitive sensors (see below) as well as better interference cancellation approaches. For example, better MSRs could aid with reducing the noise level in zero-field magnetometers. In addition, as shown in Chapter 4, OPMs benefit from gradiometric approaches and therefore, either OPM-based gradiometers, or improved reference arrays (afforded by more flexible sensor placement) could be explored to reduce interference and consequently improve spatial resolution and SNR.

7.2 Improved practicality

The MEG measurements presented in Chapter 5 demonstrated the improved practicality of our system: by combining multi-channel OPM arrays with bespoke scanner-casts which allow co-registration of the sensor location to brain anatomy, the MEG device becomes a wearable technology which can adapt to anyone's head shape or size. This, added to field-nulling coil technology, allows for non-restrictive scanning and even large head movement. Currently, our coil system allows movement within a $40\times40\times40$-cm^3 volume surrounding the subject's head. However, this is only limited because the bi-planar coils described in Chapter 5 were designed to fit around an existing cryogenic MEG system and in-

side the MSR. In principle, they could be modified to fit different specifications. Future work will therefore explore different coil configurations to e.g. provide a larger volume of homogeneous field, allowing not only head movements, but people walking inside the MSR. In addition, active cancellation during scanning (and not only before the experiment) could be possible allowing improvement in SNR and indeed has been demonstrated using a different type of coil system (Iivanainen et al., 2019).

7.3 3D printing and future helmet design

3D-printed scanner-casts served as a proof of concept, and allowed for an easy and straightforward co-registration, which was needed for source reconstruction. However, they are not practical for scanning multiple subjects due to the high cost of 3D printing and also they do not seem suitable for scanning children. Future work should therefore focus in the design of different helmets, ideally being adaptable and flexible, like an EEG/fNIRS cap. The challenge of these flexible configurations, however, would be to work out where the sensors are located on the head. This remains a significant challenge, however, optical digitisation of the sensors and head shape could become a useful tool for co-registration (Zetter et al., 2019), and even methods currently used for conventional MEG (like the use of a Polhemus 3D digitiser), could be revisited.

7.4 New OPM designs

All of the work carried out in this thesis used first generation (Gen-1) QuSpin OPMs. However, as of August 2018, the second generation (Gen-2) of QZFM sensors has been released[1]. Figure 7.1 shows a photograph of a Gen-1 sensor next to a Gen-2, and Table 7.1 summarises their specifications for comparison.

[1] https://quspin.com/qzfm-gen-2-update/



Figure 7.1: **QuSpin Gen-1 and Gen-2 sensors.**

Table 7.1: **QuSpin Gen-1 and Gen-2 QZFM sensor specifications.** Adapted from `https://quspin.com/qzfm-gen-2-update/`.

Metric	**Gen-1**	**Gen-2**
Sensitivity	15 fT/$\sqrt{\text{Hz}}$	7–10 fT/$\sqrt{\text{Hz}}$
Bandwidth	135 Hz	135 Hz
Maximum background field	50 nT	200 nT
Stand-off	6 mm	6.5 mm
Size	13×19×110 mm^3	12.4×16.6×24.4 mm^3
Sensor weight	20 g	4 g
Cable weight	10 g/ft	1 g/ft
Surface temperature	∼45°C	∼41°C

Gen-2 sensors are smaller, lighter and overall have a better performance than the previous generation. These modifications, the author believes will have a significant impact on the future design of OPM-MEG systems, in particular for use in infant populations and for studies in freely moving subjects.

7.5 Epilogue

Whole-head MEG systems have been available since the mid 90's, and since then we have seen remarkable progress, with the introduction of new techniques for data modelling enabling significant new insights into how brain electrophysiol-

ogy supports cognitive function in the healthy brain, and how such mechanisms are perturbed in disease. However, in over a quarter of a century, there has been relatively little development in MEG hardware, and no improvement in the fundamental limitations introduced by cryogenic sensors. OPMs offer an opportunity to lift these limitations. OPM-MEG is in its infancy: a large number of physics and engineering challenges remain to be solved, and the system presented in this thesis is not yet a viable platform upon which to launch medical research programmes. Nevertheless, this proof of principle of our wearable system and the unique capabilities that it brings, potentially represents the "end of the beginning" of a new chapter in MEG development: one which will see a fundamental shift not only in MEG technology, but also in the type of questions that can be addressed by functional neuroimaging.

Bibliography

Ahlfors, S. P., Ilmoniemi, R. J., and Hämäläinen, M. S. (1992). Estimates of visually evoked cortical currents. Electroencephalography and Clinical Neurophysiology, 82(3):225–236.

Allred, J. C., Lyman, R. N., Kornack, T. W., and Romalis, M. V. (2002). High-Sensitivity Atomic Magnetometer Unaffected by Spin-Exchange Relaxation. Physical Review Letters, 89(13):130801.

Andersen, L. M., Oostenveld, R., Pfeiffer, C., Ruffieux, S., Jousmäki, V., Hämäläinen, M., Schneiderman, J. F., and Lundqvist, D. (2017). Similarities and differences between on-scalp and conventional in-helmet magnetoencephalography recordings. PLoS ONE, 12(7):e0178602.

Baillet, S. (2017). Magnetoencephalography for brain electrophysiology and imaging. Nature Neuroscience, 20(3):327–339.

Baker, A. P., Brookes, M. J., Rezek, I. A., Smith, S. M., Behrens, T., Smith, P. J. P., and Woolrich, M. W. (2014). Fast transient networks in spontaneous human brain activity - Figures and figure supplements. eLife, 2014(3):e01867.

Bardeen, J., Cooper, L. N., and Schrieffer, J. R. (1957). Microscopic Theory of Superconductivity. Physical Review, 106(1):162–164.

Barnes, G. R. and Hillebrand, A. (2003). Statistical flattening of MEG beamformer images. Human Brain Mapping, 18(1):1–12.

Barratt, E. L., Francis, S. T., Morris, P. G., and Brookes, M. J. (2018). Mapping the topological organisation of beta oscillations in motor cortex using MEG. NeuroImage, 181(6):831–844.

Barratt, E. L., Tewarie, P. K., Clarke, M. A., Hall, E. L., Gowland, P. A., Morris, P. G., Francis, S. T., Evangelou, N., and Brookes, M. J. (2017). Abnormal task driven neural oscillations in multiple sclerosis: A visuomotor MEG study. Human Brain Mapping, 38(5):2441–2453.

Berger, H. (1929). Über das Elektrenkephalogramm des Menschen. Archiv für Psychiatrie und Nervenkrankheiten, 87(1):527–570.

Bloch, F. (1946). Nuclear Induction. Physical Review, 70(7- 8):460.

Boto, E., Bowtell, R., Krüger, P., Fromhold, T. M., Morris, P. G., Meyer, S. S., Barnes, G. R., and Brookes, M. J. (2016). On the potential of a new generation of magnetometers for MEG: A beamformer simulation study. PLoS ONE, 11(8):e0157655.

Boto, E., Holmes, N., Leggett, J., Roberts, G., Shah, V., Meyer, S. S., Muñoz, L. D., Mullinger, K. J., Tierney, T. M., Bestmann, S., Barnes, G. R., Bowtell, R., and Brookes, M. J. (2018). Moving magnetoencephalography towards real-world applications with a wearable system. Nature, 555(7698):657–661.

Boto, E., Meyer, S. S., Shah, V., Alem, O., Knappe, S., Kruger, P., Fromhold, T. M., Lim, M., Glover, P. M., Morris, P. G., Bowtell, R., Barnes, G. R., and Brookes, M. J. (2017). A new generation of magnetoencephalography: Room temperature measurements using optically-pumped magnetometers. NeuroImage, 149:404–414.

Brookes, M. J., Vrba, J., Mullinger, K. J., Geirsdóttir, G. B., Yan, W. X., Stevenson, C. M., Bowtell, R., and Morris, P. G. (2009). Source localisation in concurrent EEG/fMRI: Applications at 7T. NeuroImage, 45(2):440–452.

Brookes, M. J., Vrba, J., Robinson, S. E., Stevenson, C. M., Peters, A. M., Barnes, G. R., Hillebrand, A., and Morris, P. G. (2008). Optimising experimental design for MEG beamformer imaging. NeuroImage, 39(4):1788–1802.

Brookes, M. J., Woolrich, M. W., and Barnes, G. R. (2012). Measuring functional connectivity in MEG: A multivariate approach insensitive to linear source leakage. NeuroImage, 63(2):910–920.

Brookes, M. J., Zumer, J. M., Stevenson, C. M., Hale, J. R., Barnes, G. R., Vrba, J., and Morris, P. G. (2010). Investigating spatial specificity and data averaging in MEG. NeuroImage, 49(1):525–538.

Cheyne, D. O. (2013). MEG studies of sensorimotor rhythms: A review. Experimental Neurology, 245:27–39.

Claus, S., Velis, D., Lopes da Silva, F. H., Viergever, M. A., and Kalitzin, S. (2012). High frequency spectral components after Secobarbital: The contribution of muscular origin-A study with MEG/EEG. Epilepsy Research, 100(1-2):132–141.

Cohen, D. (1968). Magnetoencephalography: Evidence of magnetic fields produced by alpha-rhythm currents. Science, 161(3843):784–786.

Cohen, D. (1972). Magnetoencephalography: Detection of the brain's electrical activity with a superconducting magnetometer. Science, 175(4022):664–666.

Cohen-Tannoudji, C., Dupont-Roc, J., Haroche, S., and Laloë, F. (1970). Diverses résonances de croisement de niveaux sur des atomes pompés optiquement en champ nul. I. Théorie. Revue de Physique Appliquée, 5(1):95–101.

Colombo, A. P., Carter, T. R., Borna, A., Jau, Y.-Y., Johnson, C. N., Dagel, A. L., and Schwindt, P. D. D. (2016). Four-channel optically pumped atomic magnetometer for magnetoencephalography. Optics Express, 24(14):15403.

Crone, N. E., Sinai, A., and Korzeniewska, A. (2006). High-frequency gamma oscillations and human brain mapping with electrocorticography. Progress in Brain Research, 159:275–295.

Dale, M. W. and Morley, G. W. (2017). Medical applications of diamond magnetometry: commercial viability. arXiv preprint arXiv:1705.01994.

Dang, H. B., Maloof, A. C., and Romalis, M. V. (2010). Ultrahigh sensitivity magnetic field and magnetization measurements with an atomic magnetometer. Applied Physics Letters, 97(15):151110.

Engel, A. K., Fries, P., and Singer, W. (2001). Dynamic predictions: Oscillations and synchrony in top–down processing. Nature Reviews Neuroscience, 2(10):704.

Fang, Q. and Boas, D. A. (2009). Tetrahedral mesh generation from volumetric binary and grayscale images. In Proceedings - 2009 IEEE International Symposium on Biomedical Imaging: From Nano to Macro, ISBI 2009, pages 1142–1145. IEEE.

Ferrari, M. and Quaresima, V. (2012). A brief review on the history of human functional near-infrared spectroscopy (fNIRS) development and fields of application. NeuroImage, 63(2):921–935.

Fischl, B., Liu, A., and Dale, A. M. (2001). Automated manifold surgery: Constructing geometrically accurate and topologically correct models of the human cerebral cortex. IEEE Transactions on Medical Imaging, 20(1):70–80.

Fox, P. T., Mintum, M. A., Raichle, M. E., and Herscovitch, P. (1984). A noninvasive approach to quantitative functional brain mapping with H215O and positron emission tomography. Journal of Cerebral Blood Flow and Metabolism, 4(3):329–333.

Gaetz, W., MacDonald, M., Cheyne, D., and Snead, O. C. (2010). Neuromagnetic imaging of movement-related cortical oscillations in children and adults: Age predicts post-movement beta rebound. NeuroImage, 51(2):792–807.

Geselowitz, D. B. (1967). On Bioelectric Potentials in an Inhomogeneous Volume Conductor. Biophysical Journal, 7(1):1–11.

Giacometti, P., Perdue, K. L., and Diamond, S. G. (2014). Algorithm to find high density EEG scalp coordinates and analysis of their correspondence to structural and functional regions of the brain. Journal of Neuroscience Methods, 229:84–96.

Griffith, W. C., Knappe, S., and Kitching, J. (2010). Femtotesla atomic magnetometry in a microfabricated vapor cell. Optics Express, 18(26):27167.

Gross, J., Baillet, S., Barnes, G. R., Henson, R. N., Hillebrand, A., Jensen, O., Jerbi, K., Litvak, V., Maess, B., Oostenveld, R., Parkkonen, L., Taylor, J. R., van Wassenhove, V., Wibral, M., and Schoffelen, J. M. (2013). Good practice for conducting and reporting MEG research. NeuroImage, 65:349–363.

Hadamard, J. (1902). Sur les problèmes aux derivées partielles et leur signification physique. Princeton University Bulletin, 13(4):49–52.

Hajipour Sardouie, S., Shamsollahi, M. B., Albera, L., and Merlet, I. (2015). Denoising of ictal EEG data using semi-blind source separation methods based on time-frequency priors. IEEE Journal of Biomedical and Health Informatics, 19(3):839–847.

Hämäläinen, M. S., Hari, R., Ilmoniemi, R. J., Knuutila, J., and Lounasmaa, O. V. (1993). Magnetoencephalography – theory, instrumentation, and applications to noninvasive studies of the working human brain. Reviews of Modern Physics, 65(2):413–497.

Hanle, W. (1925). Die magnetische Beeinflussung der Resonanzfluoreszenz. Ergebnisse der exakten naturwissenschaften, 4:214.

Happer, W. (1972). Optical pumping. Reviews of Modern Physics, 44(2):169–249.

Happer, W. and Tang, H. (1973). Spin-exchange shift and narrowing of magnetic resonance lines in optically pumped alkali vapors. Physical Review Letters, 31(5):273–276.

Hari, R., Karhu, J., Hämäläinen, M. S., Knuutila, J., Salonen, O., Sams, M., and Vilkman, V. (1993). Functional Organization of the Human First and Second Somatosensory Cortices: a Neuromagnetic Study. European Journal of Neuroscience, 5(6):724–734.

Hari, R., Pelizzone, M., Mäkelä, J. P., Hällström, J., Leinonen, L., and Lounasmaa, O. V. (1987). Neuromagnetic responses of the human auditory cortex to on- and offsets of noise bursts. International Journal of Audiology, 26(1):31–43.

Hari, R. and Salmelin, R. (1997). Human cortical oscillations: a neuromagnetic view through the skull. Trends in Neurosciences, 20(1):44–49.

Hillebrand, A. and Barnes, G. (2002). A Quantitative Assessment of the Sensitivity of Whole-Head MEG to Activity in the Adult Human Cortex. NeuroImage, 16(3):638–650.

Hillebrand, A. and Barnes, G. R. (2003). The use of anatomical constraints with MEG beamformers. NeuroImage, 20(4):2302–2313.

Hipp, J. F., Hawellek, D. J., Corbetta, M., Siegel, M., and Engel, A. K. (2012). Large-scale cortical correlation structure of spontaneous oscillatory activity. Nature Neuroscience, 15(6):884–890.

Holmes, N., Leggett, J., Boto, E., Roberts, G., Hill, R. M., Tierney, T. M., Shah, V., Barnes, G. R., Brookes, M. J., and Bowtell, R. (2018). A bi-planar coil system for nulling background magnetic fields in scalp mounted magnetoencephalography. NeuroImage, 181:760–774.

Hounsfield, G. N. (1973). Computerized transverse axial scanning (tomography): I. Description of system. British Journal of Radiology, 46(552):1016–1022.

Huang, M. X., Mosher, J. C., and Leahy, R. M. (1999). A sensor-weighted overlapping-sphere head model and exhaustive head model comparison for MEG. Physics in Medicine and Biology, 44(2):423–440.

Iivanainen, J., Stenroos, M., and Parkkonen, L. (2017). Measuring MEG closer to the brain: Performance of on-scalp sensor arrays. NeuroImage, 147:542–553.

Iivanainen, J., Zetter, R., Grön, M., Hakkarainen, K., and Parkkonen, L. (2019). On-scalp MEG system utilizing an actively shielded array of optically-pumped magnetometers. NeuroImage, 194:244–258.

Jaklevic, R. C., Lambe, J., Silver, A. H., and Mercereau, J. E. (1964). Quantum interference effects in Josephson tunneling. Physical Review Letters, 12(7):159–160.

Johnson, C. N., Schwindt, P. D., and Weisend, M. (2013). Multi-sensor magnetoencephalography with atomic magnetometers. Physics in Medicine and Biology, 58(17):6065–6077.

Johnson, C. N., Schwindt, P. D. D., and Weisend, M. (2010). Magnetoencephalography with a two-color pump-probe, fiber-coupled atomic magnetometer. Applied Physics Letters, 97(24).

Josephson, B. (1962). Possible new effects in superconductive tunnelling. Physics Letters, 1(7):251–253.

Kamada, K., Sato, D., Ito, Y., Natsukawa, H., Okano, K., Mizutani, N., and Kobayashi, T. (2015). Human magnetoencephalogram measurements using newly developed compact module of high-sensitivity atomic magnetometer. Japanese Journal of Applied Physics, 54(2):026601.

Kastler, A. (1973). The Hanle effect and its use for the measurements of very small magnetic fields. Nuclear Instruments and Methods, 110(C):259–265.

Kiebel, S. J., Daunizeau, J., Phillips, C., and Friston, K. J. (2008). Variational Bayesian inversion of the equivalent current dipole model in EEG/MEG. NeuroImage, 39(2):728–741.

Kilavik, B. E., Zaepffel, M., Brovelli, A., MacKay, W. A., and Riehle, A. (2013). The ups and downs of beta oscillations in sensorimotor cortex. Experimental Neurology, 245:15–26.

Kim, K., Begus, S., Xia, H., Lee, S. K., Jazbinsek, V., Trontelj, Z., and Romalis, M. V. (2014). Multi-channel atomic magnetometer for magnetoencephalography: A configuration study. NeuroImage, 89:143–151.

Knuutila, J. E. T., Ahonen, A. I., Hämäläinen, M. S., Kajola, M. J., Laine, P. P., Lounasmaa, O. V., Parkkonen, L. T., Simola, J. T. A., and Tesche, C. D. (1993). A 122-Channel Whole-Cortex SQUID System for Measuring the Brain'S Magnetic Fields. IEEE Transactions on Magnetics, 29(6):3315–3320.

Kominis, I. K., Kornack, T. W., Allred, J. C., and Romalis, M. V. (2003). A subfemtotesla multichannel atomic magnetometer. Nature, 422(6932):596–599.

Kranczioch, C., Zich, C., Schierholz, I., and Sterr, A. (2014). Mobile EEG and its potential to promote the theory and application of imagery-based motor rehabilitation. International Journal of Psychophysiology, 91(1):10–15.

Lauterbur, P. C. (1973). Image formation by induced local interactions: Examples employing nuclear magnetic resonance. Nature, 242(5394):190–191.

Liuzzi, L., Gascoyne, L. E., Tewarie, P. K., Barratt, E. L., Boto, E., and Brookes, M. J. (2017). Optimising experimental design for MEG resting state functional connectivity measurement. NeuroImage, 155:565–576.

Lopes da Silva, F. (2013). EEG and MEG: Relevance to neuroscience. Neuron, 80(5):1112–1128.

López, J. D., Penny, W. D., Espinosa, J. J., and Barnes, G. R. (2012). A general Bayesian treatment for MEG source reconstruction incorporating lead field uncertainty. NeuroImage, 60(2):1194–1204.

Luckhoo, H., Hale, J. R., Stokes, M. G., Nobre, A. C., Morris, P. G., Brookes, M. J., and Woolrich, M. W. (2012). Inferring task-related networks using independent component analysis in magnetoencephalography. NeuroImage, 62(1):530–541.

Mansfield, P. (1977). Multi-planar image formation using NMR spin echoes. Journal of Physics C: Solid State Physics, 10(3):L55—-L58.

Mansfield, P. and Grannell, P. K. (1973). Nmr 'diffraction' in solids? Journal of Physics C: Solid State Physics, 6(22):L422–L426.

Martínez-Vargas, J. D., López, J. D., Baker, A., Castellanos-Dominguez, G., Woolrich, M. W., and Barnes, G. R. (2016). Non-linear parameter estimates from non-stationary MEG data. Frontiers in Neuroscience, 10(AUG):336.

Mary, A., Bourguignon, M., Wens, V., Op de Beeck, M., Leproult, R., De Tiège, X., and Peigneux, P. (2015). Aging reduces experience-induced sensorimotor plasticity. A magnetoencephalographic study. NeuroImage, 104:59–68.

Mhaskar, R., Knappe, S., and Kitching, J. (2012). A low-power, high-sensitivity micromachined optical magnetometer. Applied Physics Letters, 101(24):241105.

Mullinger, K. J., Mayhew, S. D., Bagshaw, A. P., Bowtell, R., and Francis, S. T. (2013). Poststimulus undershoots in cerebral blood flow and BOLD fMRI responses are modulated by poststimulus neuronal activity. Proceedings of the National Academy of Sciences, 110(33):13636–13641.

Murakami, S. and Okada, Y. (2006). Contributions of principal neocortical neurons to magnetoencephalography and electroencephalography signals. Journal of Physiology, 575(3):925–936.

Muthukumaraswamy, S. D. (2013). High-frequency brain activity and muscle artifacts in MEG/EEG: a review and recommendations. Frontiers in Human Neuroscience, 7:138.

Nolte, G., Bai, O., Wheaton, L., Mari, Z., Vorbach, S., and Hallett, M. (2004). Identifying true brain interaction from EEG data using the imaginary part of coherency. Clinical Neurophysiology, 115(10):2292–2307.

Ogawa, S., Lee, T. M., Kay, A. R., and Tank, D. W. (1990). Brain magnetic resonance imaging with contrast dependent on blood oxygenation. Proceedings of the National Academy of Sciences, 87(24):9868–9872.

Öisjöen, F., Schneiderman, J. F., Figueras, G. A., Chukharkin, M. L., Kalabukhov, A., Hedström, A., Elam, M., and Winkler, D. (2012). High-T c superconducting quantum interference device recordings of spontaneous brain activity: Towards high-T c magnetoencephalography. Applied Physics Letters, 100(13):132601.

O'Neill, G. C., Barratt, E. L., Hunt, B. A. E., Tewarie, P. K., and Brookes, M. J. (2015a). Measuring electrophysiological connectivity by power envelope correlation: A technical review on MEG methods. Physics in Medicine and Biology, 60(21):R271–R295.

O'Neill, G. C., Bauer, M., Woolrich, M. W., Morris, P. G., Barnes, G. R., and Brookes, M. J. (2015b). Dynamic recruitment of resting state sub-networks. NeuroImage, 115:85–95.

Onnes, H. K. (1911). Further experiments with Liquid Helium. D. On the change of Electrical Resistance of Pure Metals at very low Temperatures, etc. V. The Disappearance of the resistance of mercury. In Koninklijke Nederlandse Akademie van Weteschappen Proceedings, volume 14, pages 113–115. Amsterdam.

Oostenveld, R. and Praamstra, P. (2001). The five percent electrode system for high-resolution EEG and ERP measurements. Clinical Neurophysiology, 112(4):713–719.

Orrison, W. W., Lewine, J. D., Sanders, J. A., and Hartshorne, M. F. (1995). Functional Brain Imaging. Mosby.

Osborne, J., Orton, J., Alem, O., and Shah, V. (2018). Fully integrated, standalone zero field optically pumped magnetometer for biomagnetism. Steep Dispersion Engineering and Opto-Atomic Precision Metrology XI, 10548.

Petrashov, V. T., Antonov, V. N., Delsing, P., and Claeson, T. (1995). Phase controlled conductance of mesoscopic structures with superconducting "mirrors". Physical Review Letters, 74(26):5268.

Pfurtscheller, G. and Lopes Da Silva, F. H. (1999). Event-related EEG/MEG synchronization and desynchronization: Basic principles. Clinical Neurophysiology, 110(11):1842–1857.

Riaz, B., Pfeiffer, C., and Schneiderman, J. F. (2017). Evaluation of realistic layouts for next generation on-scalp MEG: Spatial information density maps. Scientific Reports, 7(1).

Robinson, S. E. and Vrba, J. (1999). Recent advances in biomagnetism. Functional neuroimaging by synthetic aperture magnetometry (SAM). In Yoshimoto, T., Kotani, M., Kuriki, S., Karibe, H., and Nakasato, N., editors, Tohoku University Press, Sendai, pages 302–305. Tohoku University Press, Sendai, Japan.

Robson, S. E., Brookes, M. J., Hall, E. L., Palaniyappan, L., Kumar, J., Skelton, M., Christodoulou, N. G., Qureshi, A., Jan, F., Katshu, M. Z., Liddle, E. B., Liddle, P. F., and Morris, P. G. (2016). Abnormal visuomotor processing in schizophrenia. NeuroImage: Clinical, 12:869–878.

Rondin, L., Tetienne, J. P., Hingant, T., Roch, J. F., Maletinsky, P., and Jacques, V. (2014). Magnetometry with nitrogen-vacancy defects in diamond. Reports on Progress in Physics, 77(5):056503.

Sander, T. H., Preusser, J., Mhaskar, R., Kitching, J., Trahms, L., and Knappe, S. (2012). Magnetoencephalography with a chip-scale atomic magnetometer. Biomedical Optics Express, 3(5):981.

Sarvas, J. (1987). Basic mathematical and electromagnetic concepts of the biomagnetic inverse problem. Physics in Medicine and Biology, 32(1):11–22.

Schwindt, P. D. D., Knappe, S., Shah, V., Hollberg, L., Kitching, J., Liew, L.-a., Schwindt, P. D. D., Knappe, S., Shah, V., Hollberg, L., and Kitching, J. (2017). Chip-scale atomic magnetometer. Applied Physics Letters, 6409(2004):1–4.

Schwindt, P. D. D., Lindseth, B., Knappe, S., Shah, V., Kitching, J., and Liew, L. A. (2007). Chip-scale atomic magnetometer with improved sensitivity by use of the Mx technique. Applied Physics Letters, 90(8):81102–811023.

Sekihara, K., Nagarajan, S. S., Poeppel, D., and Marantz, A. (2004). Performance of an MEG Adaptive-Beamformer Source Reconstruction Technique in the Presence of Additive Low-Rank Interference. IEEE Transactions on Biomedical Engineering, 51(1):90–99.

Seltzer, S. J. (2008). Developments in Alkali-Metal Atomic Magnetometry. PhD thesis, Princeton University.

Shah, V., Knappe, S., Schwindt, P. D., and Kitching, J. (2007). Subpicotesla atomic magnetometry with a microfabricated vapour cell. Nature Photonics, 1(11):649–652.

Shah, V. and Romalis, M. V. (2009). Spin-exchange relaxation-free magnetometry using elliptically polarized light. Physical Review A - Atomic, Molecular, and Optical Physics, 80(1):13416.

Shah, V. K. and Wakai, R. T. (2013). A Compact, High Performance Atomic Magnetometer for Biomedical Applications. Physics in Medicine & Biology, 58(22):8153–8161.

Shelly, C. D., Matrozova, E. A., and Petrashov, V. T. (2016). Superconductivity: Resolving thermoelectric "paradox" in superconductors. Science Advances, 2(2):e1501250–e1501250.

Sheng, D., Perry, A. R., Krzyzewski, S. P., Geller, S., Kitching, J., and Knappe, S. (2017). A microfabricated optically-pumped magnetic gradiometer. Applied Physics Letters, 110(3).

Singer, W. (1999). Neuronal synchrony: a versatile code for the definition of relations? Neuron, 24(1):49–65.

Stam, C. J., Nolte, G., and Daffertshofer, A. (2007). Phase lag index: Assessment of functional connectivity from multi channel EEG and MEG with diminished bias from common sources. Human Brain Mapping, 28(11):1178–1193.

Stenroos, M., Hunold, A., and Haueisen, J. (2014). Comparison of three-shell and simplified volume conductor models in magnetoencephalography. NeuroImage, 94:337–348.

Tewarie, P. K., Steenwijk, M. D., Brookes, M. J., Uitdehaag, B. M., Geurts, J. J., Stam, C. J., and Schoonheim, M. M. (2018). Explaining the heterogeneity of functional connectivity findings in multiple sclerosis: An empirically informed modeling study. Human Brain Mapping, 39(6):2541–2548.

Timmermann, L., Gross, J., Dirks, M., Volkmann, J., Freund, H. J., and Schnitzler, A. (2003). The cerebral oscillatory network of parkinsonian resting tremor. Brain, 126(1):199–212.

Tröebinger, L., López, J. D., Lutti, A., Bradbury, D., Bestmann, S., and Barnes, G. (2014). High precision anatomy for MEG. NeuroImage, 86:583–591.

Uhlhaas, P. J. and Singer, W. (2010). Abnormal neural oscillations and synchrony in schizophrenia. Nature Reviews Neuroscience, 11(2):100–113.

Van Veen, B. D. and Buckley, K. M. (1988). Beamforming: A Versatile Approach to Spatial Filtering. IEEE ASSP Magazine, 5(2):4–24.

Van Veen, B. D., van Drongelen, W., Yuchtman, M., and Suzuki, A. (1997). Localization of brain electrical activity via linearly constrained minimum variance spatial filtering. IEEE Transactions on Biomedical Engineering, 44(9):867–880.

Vrba, J. (2000). Multichannel SQUID Biomagnetic Systems. In Weinstock, H., editor, Applications of Superconductivity, pages 61–138. Springer Science+Business Media B.V., Dordrecht.

Vrba, J. (2002). Magnetoencephalography: The art of finding a needle in a haystack. Physica C: Superconductivity and its Applications, 368(1-4):1–9.

Vrba, J., Anderson, G., and Betts, K. (1999). 151-Channel whole-cortex MEG system for seated or supine positions. In Yoshimoto, T., Kotani, M., Kuriki, S., Karibe, H., and Nakasato, N., editors, Recent Advances in Biomagnetism, pages 93–96. Tohoku University Press, Sendai, Japan.

Vrba, J., Haid, G., Lee, S., Taylor, B., Fife, A. A., Kubik, P., McCubbin, J., and Burbank, M. B. (1991). Biomagnetometers for unshielded and well shielded environments. Clinical Physics and Physiological Measurement, 12(B):81–86.

Vrba, J. and Robinson, S. E. (2001). Signal processing in magnetoencephalography. Methods, 25(2):249–271.

Vrba, J. and Robinson, S. E. (2002). SQUID sensor array configurations for magnetoencephalography applications. Superconductor Science and Technology, 15(9):R51.

Whitham, E. M., Pope, K. J., Fitzgibbon, S. P., Lewis, T., Clark, C. R., Loveless, S., Broberg, M., Wallace, A., DeLosAngeles, D., Lillie, P., Hardy, A., Fronsko, R., Pulbrook, A., and Willoughby, J. O. (2007). Scalp electrical recording during paralysis: Quantitative evidence that EEG frequencies above 20 Hz are contaminated by EMG. Clinical Neurophysiology, 118(8):1877–1888.

Xia, H., Ben-Amar Baranga, A., Hoffman, D., and Romalis, M. V. (2006). Magnetoencephalography with an atomic magnetometer. Applied Physics Letters, 89(21):Article number 211104.

Zetter, R., Iivanainen, J., and Parkkonen, L. (2019). Optical Co-registration of MRI and On-scalp MEG. Scientific Reports, 9(1):5490.

Zetter, R., Iivanainen, J., Stenroos, M., and Parkkonen, L. (2018). Requirements for Coregistration Accuracy in On-Scalp MEG. Brain Topography, 31(6):931–948.

Zimmerman, J. E., Thiene, P., and Harding, J. T. (1970). Design and operation of stable rf-biased superconducting point-contact quantum devices, and a note on the properties of perfectly clean metal contacts. Journal of Applied Physics, 41(4):1572–1580.

Zimmermann, R. and Scharein, E. (2004). MEG and EEG show different sensitivity to myogenic artifacts. Neurology & clinical neurophysiology: NCN, 2004:78.